

**CHARACTERIZATION OF ROCK  
SAMPLES USING SWIR-LWIR  
HYPERSPETRAL IMAGING  
TECHNIQUES – AN EXAMPLE OF  
THE HIGH SULFIDATION  
EPITHERMAL SYSTEM OF  
RODALQUILAR, SOUTHEAST  
SPAIN**

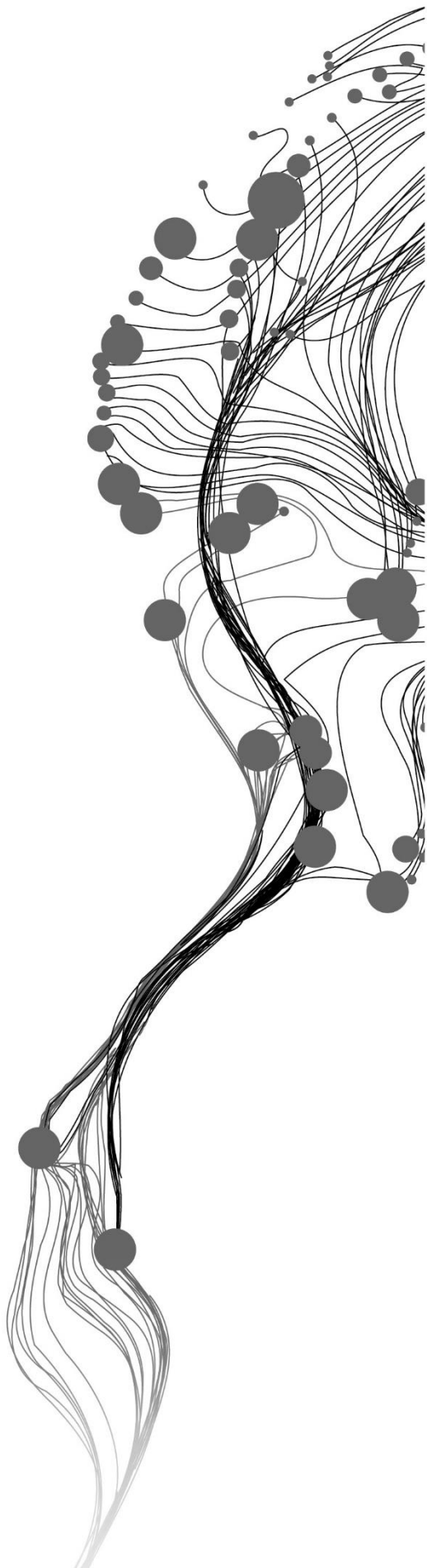
MICKIALE GIDAY ABERA

February, 2018

SUPERVISORS:

Dr. Chris Hecker

Mr. Wim Bakker, MSc.



# **CHARACTERIZATION OF ROCK SAMPLES USING SWIR-LWIR HYPERSPPECTRAL IMAGING TECHNIQUES – AN EXAMPLE OF THE HIGH SULFIDATION EPITHERMAL SYSTEM OF RODALQUILAR, SOUTHEAST SPAIN**

MICKIALE GIDAY ABERA

Enschede, The Netherlands, February, 2019

Thesis submitted to the Faculty of Geo-Information Science and Earth Observation of the University of Twente in partial fulfillment of the requirements for the degree of Master of Science in Geo-information Science and Earth Observation.

Specialization: Applied Earth Sciences in Geological remote sensing

## **SUPERVISORS:**

Dr. Chris Hecker

Mr. Wim Bakker, MSc.

## **THESIS ASSESSMENT BOARD:**

Prof. Dr. M. van der Meijde (Chair)

Dr. Martin Schodlok (External Examiner, BGR, Germany)

#### DISCLAIMER

This document describes work undertaken as part of a programme of study at the Faculty of Geo-Information Science and Earth Observation of the University of Twente. All views and opinions expressed therein remain the sole responsibility of the author and do not necessarily represent those of the Faculty.

## ABSTRACT

This study presents the use of SWIR and LWIR range image data for characterizing the rock samples of the Rodalquilar high sulfidation epithermal system, Southeast Spain. Quartz is essential in the high sulfidation epithermal system mainly for the identification of the silicified and advanced argillic zone. However, quartz is difficult to detect with only SWIR range data because this non-hydroxide mineral has no diagnostic absorption features in the SWIR range. In this research, hyperspectral SWIR and LWIR images of 56 rock samples from the Rodalquilar epithermal system were used to characterize the minerals in the rock. The image files were subjected to several pre-processing steps. For the SWIR range, the image files were converted to reflectance data, spatially and spectrally subsetted and 1+5+1 mean filtered. For the LWIR range, the image files were converted to emissivity data, spatially and spectrally subsetted, and a forward and inverse MNF transform was applied. Subsequently, wavelength mapping was used to assist the relevant endmember extraction. Spectral angle mapper (SAM) was performed to produce mineral maps. The independent SWIR and LWIR results were combined for the identification and mapping of the minerals in the rock samples. The SWIR and LWIR results were combined by determining the three most dominant minerals and important hydrothermal indicator minerals from both ranges. From the combined SWIR-LWIR result, the rock samples were assigned into alteration zones. The assigned alteration zones of the rock samples were also compared with existing maps. The results indicate the presence of silicate, phyllosilicate, sulfate and carbonate minerals in the rock samples. Mineral mapping with the LWIR range data provides complementary information to the SWIR range data. The combined SWIR-LWIR data analysis of the rock samples resulted in a refined distribution and mapping of silicified and advanced argillic zones in the Rodalquilar high sulfidation epithermal system. In addition, the combined SWIR-LWIR data provide comprehensive mineral identification in the rock samples. This study showed the combined SWIR-LWIR data can easily be used to identify altered and unaltered minerals in rock samples, and can be used to locate the silicic and advanced argillic zone of high sulfidation epithermal system. The identified alteration zones of this study further contribute to our understanding of hydrothermal systems and may aid future exploration in epithermal system delineation and characterization of the alteration zones of high sulfidation epithermal system. Such an approach provides a vector to ore mineralization and improves the existing map of alteration zones of the Rodalquilar epithermal system in southeast Spain.

**Keywords;** Rodalquilar, epithermal system, SWIR imaging spectroscopy, LWIR imaging spectroscopy, proximal sensing, hydrothermal alteration

## ACKNOWLEDGEMENTS

I want to acknowledge Netherlands Fellowship Programme (NFP), and International Institute for Geo-information Science and Earth Observation (ITC) for giving me the chance to join master of science in Geological Remote Sensing in University of Twente and facilitating the necessary logistics during my study. I would also like to acknowledge the Department of Geological Remote Sensing very much for providing me a vehicle during the field work to Germany and allowing me to have full access to various facilities such as laboratories. I would also like to acknowledge the Federal Institute for Geosciences and Natural Resources (BGR), Hannover, Germany for the facilities provided such as the AISA-Owl hyperspectral camera to acquire images for this research.

I am very grateful of Dr. Chris Hecker, and Mr. Wim Bakker, my supervisors for their continuous and extraordinary help, follow up and guidance that they dedicated to me from the beginning to the end of my studies. This work could not have been materialized without their significant input, constructive criticism, and fruitful discussions. It was an honour to have such great supervisors.

Many thanks go to Prof. Freek Van der Meer, for his scientific comments and suggestions during the proposal defence and mid-term presentation.

I would also like to thank Dr. Martin Schodlok, for his assistance during the image acquisition for this research in the BGR.

Appreciation is extended to Eveline for helping me during the sample preparation in the ITC laboratory.

Last but not least, I have to thank my family and friends who supported me all along my thesis work.

# TABLE OF CONTENTS

1.	INTRODUCTION.....	1
1.1.	Background and justification.....	1
1.2.	Previous work.....	2
1.3.	Problem statement.....	2
1.4.	Objectives.....	3
1.4.1.	Specific objectives.....	3
1.5.	Research questions.....	3
1.6.	Hypothesis.....	4
1.7.	Research structure.....	4
2.	DESCRIPTION OF THE STUDY AREA.....	5
2.1.	Location.....	5
2.2.	Geological setting.....	6
2.3.	Alteration and mineralization of the Rodalquilar epithermal system.....	6
2.4.	SWIR and LWIR Spectral characteristics of the high sulfidation epithermal system.....	8
3.	DATASETS AND METHOD.....	12
3.1.	Datasets.....	12
3.1.1.	Rock samples.....	12
3.1.2.	Proximal sensing data acquisition.....	12
3.2.	Research Methods.....	13
3.2.1.	Image pre-processing.....	14
3.2.2.	Wavelength mapping.....	15
3.2.3.	Endmember extraction.....	16
3.2.4.	Mineral mapping.....	17
3.2.5.	SWIR-LWIR combining.....	17
3.2.6.	Assigning rock samples into alteration zones.....	19
4.	RESULTS.....	20
4.1.	Image pre-processing.....	20
4.2.	Wavelength map.....	22
4.3.	Endmembers.....	24
4.4.	Mineral map.....	28
4.5.	SWIR-LWIR combined result.....	31
4.6.	Assign rock samples into alteration zones.....	31
5.	DISCUSSION.....	33
5.1.	Selected data and methods.....	33
5.2.	Discussion on the results.....	34
5.2.1.	Mineral assemblages in the rock samples.....	34
5.2.2.	SWIR-LWIR combined.....	35
5.2.3.	Alteration zone classification of the rock samples.....	35
5.2.4.	Comparison with existing maps.....	35
6.	CONCLUSIONS AND RECOMMENDATIONS.....	38

## LIST OF FIGURES

Figure 2.1: Alteration map of the Rodalquilar area, (modified after Arribas et al., 1995) which show alteration patterns, sample locations, and the study area of this work in the black inset rectangle.....	5
Figure 2.2: Geological map of Rodalquilar (after Arribas et al., 1995).....	6
Figure 2.3: cross-section showing alteration zones in Rodalquilar (after Arribas et al., 1995).....	7
Figure 2.4: Emissivity and reflectance spectra from the silicic alteration zone in the LWIR and SWIR wavelength range. The arrows indicate the emissivity minima features in LWIR and absorption feature in SWIR.....	9
Figure 2.5: Emissivity and reflectance spectra from the advanced argillic zone in the LWIR and SWIR wavelength range. The arrows indicate the emissivity minima features in LWIR and absorption feature in SWIR.....	9
Figure 2.6: Emissivity and reflectance spectra from the intermediate argillic zone in the LWIR and SWIR wavelength range. The arrows indicate the emissivity minima features in LWIR and absorption feature in SWIR.....	10
Figure 2.7: Emissivity and reflectance spectra from the argillic alteration zone in the LWIR and SWIR wavelength range. The arrows indicate the emissivity minima features in LWIR and absorption feature in SWIR.....	10
Figure 2.8: Emissivity and reflectance spectra from the propylitic alteration zone in the LWIR and SWIR wavelength range. The arrows indicate the emissivity minima features in LWIR and absorption feature in SWIR.....	11
Figure 3.1: Prepared surface rock samples ready for image acquisition. A) Samples on the wooden box filled by sand and B) leveling the surface of the rock samples.....	13
Figure 3.2: Methodological flow chart.....	14
Figure 3.3: A) wavelength map of sample 04MRE055, B) RGB=first interpolated depth, first minimum wavelength, second minimum wavelength. The endmembers were collected from the highlighted colour, red represent (quartz) and the rest colours are clay minerals and C) hand specimen.....	16
Figure 4.1: SWIR image file sample 05ch096 displayed in RGB 74, 158, 218. A) Before fixing the SWIR 8th sample and B) After fix the SWIR 8 <sup>th</sup> sample and C) Spatial subset.....	20
Figure 4.2: Spectra of the pixel (142, 1804) from sample 05ch096. A) before the spectral subset and B) after the spectral subset.....	20
Figure 4.3: Spectra of the pixel (183, 1775) from sample 05ch096. A) before mean filter 1+5+1 and B) after mean filter 1+5+1. The red arrow shows the spikes before the filter.....	21
Figure 4.4: A) Spectra of the pixel (204, 766) from sample 05ch096. A) before the spectral subset and B) after the spectral subset.....	21
Figure 4.5: Forward MNF transform components sorted by decreasing signal to noise ratio (sample 05ch094).....	22
Figure 4.6: Spectra of the pixel (146, 210) from sample 05ch094. A) before forward and backward MNF transform and B) after forward and backward MNF transform. The red arrow shows the spikes before forward and backward MNF transform.....	22
Figure 4.7: Wavelength map sample 05ch094 A) SWIR image for the wavelength range between 2100-2400nm and B) LWIR image for the wavelength range between 8900-9300nm.....	23
Figure 4.8: Spectra from sample 05ch094 showing the profile of A) Jarosite and alunite B) Jarosite, alunite, and quartz.....	23

Figure 4.9: Wavelength map of sample 07ch003 A) wavelength range between 2100-2400 nm, B) wavelength range between 2200-2210 nm, C) wavelength range between 8000-11500 nm and D) wavelength range between 8800-9300 nm.....	24
Figure 4.10: Spectra from sample 07ch003 showing the profile of A) dickite, nacrite, alunite, jarosite. B) spectrum of quartz minerals shows a shift in the deepest emissivity minima. The vertical black lines represent a shift in the deepest emissivity minima of quartz. ....	24
Figure 4.11: Spectra of selected pure endmembers from SWIR wavelength range versus USGS spectral library.....	25
Figure 4.12: Endmember spectra A) HX_kaolinite and PX_kaolinite B) Alunite and Alunite+water C) D-Halloysite and H-Halloysite. ....	26
Figure 4.13: Spectra of selected endmembers from LWIR wavelength range and comparison with spectral libraries (USGS, JHU, and ASU). ....	27
Figure 4.14: Mineral map from sample A) 07ch014 SWIR range, B) 07ch014 LWIR range, C) SWIR range 05ch094 and D) 05ch094 LWIR range .....	29
Figure 4.15: Mineral map sample P.012 A) SWIR range B) LWIR range, and mineral map sample 07ch009 C) SWIR range D) LWIR range.....	29
Figure 4.16: Crosscutting two generations of alunite veins in sample 05ch099 highlighted by cyan colour in the SWIR range. The white inset rectangle indicates the cross-cutting relationship between the two alunite veins. ....	30
Figure 4.17: Veinlet composed of oxidized sulfide minerals from the hand specimen observation A) and highlighted by a black linear feature in SWIR range B) and highlighted by green colour quartz mineral in LWIR range C) (sample MRE01011). The white arrow shows the oxidized sulfide veinlet.....	30
Figure 4.18: Overprinting of vuggy silica and chalcedony (sample 05ch094). The white arrows indicate jarosite filled the contact between chalcedony and vuggy silica, and within the chalcedony.....	31
Figure 4.19: Rock samples and alteration zones. A) shows rock sample locations, profile lines X-X' and profile line Y-Y,' B) Cross-section of the alteration zones along the profile line X-X,' C) cross-section of the alteration zones along the profile line Y-Y.' The sample number label with different colour represents the type of the alteration zone similar to the legend.....	32
Figure 5.1: Cross-section of the alteration zones of the Rodalquilar area (after Arribas et al., 1995). A) Cross-section of the alteration zones along the profile line X-X,' B) cross-section of the alteration zones along the profile line Y-Y.' The colour of the sample number label represent the alteration zones such as red (silicic), orange (second advanced argillic), cyan (intermediate argillic), magenta (argillic) and green (propylitic) ....	37
Figure 5.2: lithological cross-section map of the Rodalquilar area (after Arribas et al., 1995). The colour of the sample number label represent the alteration zones such as red (silicic), orange (second advanced argillic), cyan (intermediate argillic), magenta (argillic) and green (propylitic).....	37

## LIST OF TABLES

Table 1.1: Mineral assemblages and alteration types in the two styles of the epithermal system (Hauff, 1983; Arribas, 1995; Hedenquist et al., 2000; Pirajno, 2009). The “+” sign indicates the minerals are significant and dominant in the zone. The “,” after “+” signs represent the presence of minerals in the zone but not always.....	1
Table 2.1: Significant mineral assemblage and alteration zones in the Rodalquilar epithermal system. The “+” sign indicates the significant and dominant minerals in the zone. The “,” after “+” signs represent the presence of minerals in the zone but not dominant. ....	8
Table 3.1: Instrument specifications and setting.....	13
Table 3.2: The main activities and purposes of image processing.....	15
Table 3.3: SAM-Mineral abundance of selected rock samples.....	18
Table 3.4: Examples of the selected three most dominant minerals, important minerals and SWIR-LWIR significant minerals in the rock samples. The bold black text in column 3 indicates the most abundant and significant mineral in the rock. ....	18
Table 4.1: The SWIR-LWIR combined result. The bold black text in column 4 indicates the most significant mineral in the rock. ....	31

# 1. INTRODUCTION

## 1.1. Background and justification

Mineral assemblages and alteration zones in epithermal systems are formed due to chemical reactions of the hot fluids, with the host rock at shallow depths, typically <1km below the earth's surface (Heald et al., 1987). Changes in pH value, salinity, temperature, pressure of the fluids and composition of the host rock lead to the formation of different mineral assemblages and alteration zones in the system (Saunders et al., 2013). These systems are broadly subdivided into two categories, namely high sulfidation and low sulfidation (Hedenquist et al., 2000), and occur with characteristic alteration mineral assemblages as shown in Table 1.1 below.

Table 1.1: Mineral assemblages and alteration types in the two styles of the epithermal system (Hauff, 1983; Arribas, 1995; Hedenquist et al., 2000; Pirajno, 2009). The “+” sign indicates the minerals are significant and dominant in the zone. The “;” after “+” signs represent the presence of minerals in the zone but not always.

Alteration types	Mineral assemblages	
	High sulfidation	Low sulfidation
Vuggy silica	Quartz + alunite, jarosite, sulfur	Chalcedony, opal, Adularia
Silicification	Quartz +chalcedony, alunite, barite	
Advanced argillic	Alunite, pyrophyllite, kaolinite (or dickite), + chloritic clays, dickite, topaz, diaspore, zunyite, quartz	Kaolinite + alunite, illite/smectite-native sulfur
Intermediate argillic	Kaolinite + illite, montmorillonite, smectite, sericite, quartz, K-feldspar	Illite, illite-smectite
Argillic	Kaolinite/dickite, illite-smectite + montmorillonite, sericite, quartz	Kaolinite (or halloysite, or dickite), montmorillonite + sericite (or muscovite), chlorite
Propylitic	Epidote, chlorite, calcite, + albite, K-feldspar	Epidote (or zoisite or clinozoisite), chlorite, albite + carbonate, sericite, montmorillonite

Identification of these mineral assemblages is essential for proper alteration zoning, and a pointer towards gold mineralization because the gold or ore mineralization is commonly developed within zones of vuggy silica/silicification (Arribas, 1995).

These alteration minerals (Table 1.1) can be identified using visual observation, polarization microscopy, geochemical analysis, and spectral study. Such studies are done using hand lenses, thin section, X-ray Powder Diffraction (XRD) and infrared spectroscopy respectively (Ducart et al., 2006; Forero et al., 2011). However, the use of hand lens and thin section does not allow the complete identification of minerals in the sample,

especially for the fine-grained clay alteration minerals. XRD has limitation for heterogenous mineral assemblages, and for minerals with a non-isometric crystal system, it is complicated.

Infrared spectroscopy can identify and quantify minerals irrespective of their transparency and grain size compared to polarization microscope and XRD analysis. Compared to the other remote sensing techniques, laboratory spectrometry enables researchers to scan and investigate rock samples at a higher spatial and spectral resolution (Mathieu et al., 2017; Kuosmanen et al., 2015). In general, mineral analysis from laboratory spectroscopic studies are helpful for quantitative measurements of the mineral assemblages in the rock samples. In turn, it helps for improved identification of the alteration zones and provision of vectors towards areas where ore mineralization should occur in the epithermal system.

Minerals are identified in infrared spectroscopy studies based on diagnostic absorption features which are generated by structural and compositional variations due to the fundamental electronic/vibrational processes (Clark, 1999). Critical spectral features in SWIR allow the identification of minerals such as phyllosilicates and other hydroxylated silicates, sulfates, and carbonates (Clark et al., 2003). The other primary minerals like quartz, feldspar, amphiboles, olivine, and pyroxenes can be identified in the LWIR region (Riley & Hecker, 2013) because they have strong spectral features in the LWIR. The effect of these strong spectral features (low emissivity value) is due to the fundamental vibrational frequency of Si-O bond in the 8000-11500 nm wavelength range. In the SWIR range quartz and k-feldspar minerals have no diagnostic spectral features, whereas strong features are present in the LWIR range. Therefore, the combined SWIR-LWIR range has the advantage to provide more comprehensive information on the identification of the mineral assemblages in the rock samples. Furthermore, It helps to accurately detect specific mineral variations that the human eye cannot see.

## 1.2. Previous work

This research is an example of the Rodalquilar epithermal deposit, Southeast Spain which has been selected as a case study. Studies related to the Rodalquilar epithermal system have been conducted, for example, Arribas et al. (1995) distinguished five alteration zones; silicic, advanced argillic, intermediate argillic, and propylitic using petrography (thin sections) and geochemical methods. Regarding spectral signatures, Bedini et al. (2009) used Hymap imaging spectrometer data and Multiple Endmember Spectral Mixture Analysis which could be used to refine the mapping of the alteration minerals, especially for the distribution of alunite, kaolinite, smectite-illite and pyrophyllite.

Similarly, Garcia (2013) studied the crystallinity variation of smectite-illite and kaolin hydrothermal alteration minerals using SWIR spectroscopy. Debba et al. (2009) determined a useful method for optimal exploration targeting zone using probabilistic mineral perspectivity mapping. In general, Van der Meer et al. (2012) reviewed the potentials of multispectral and hyperspectral remote sensing data for the identification and mapping of alteration minerals using a case study in Rodalquilar and conclude that, it is possible to identify kaolinite, illite, alunite, calcite, dolomite, hematite and goethite mineral. Recently, Contreras Acosta (2017) conducted research using high spatial resolution hyperspectral SWIR (1 $\mu$ m – 2.5  $\mu$ m) spectroscopy of rock sample images, and differentiate hypogene and supergene rock samples based on alteration minerals in the rock samples.

## 1.3. Problem statement

Different methods had been employed to identify the alteration minerals in the study area. For example, Arribas et al. (1995) use petrography and geochemical techniques. Others used remote sensing techniques such as airborne (Bedini et al., 2009), SWIR non-imaging spectroscopy on rock samples (Garcia, 2013) and

SWIR imaging spectroscopy on rock samples (Contreras Acosta, 2017) and none of the studies used LWIR imaging spectroscopy to identify the mineral assemblages in the epithermal system.

The SWIR (1 $\mu\text{m}$  – 2.5  $\mu\text{m}$ ) spectral range cannot be used to identify some of the expected and essential minerals, such as silica, feldspar, and barite (Table 1.1) because they do not show diagnostic spectral features in SWIR range that is due to the absence of hydroxyl groups in their mineral structure. Besides, the SWIR wavelength range has limitations on differentiating chlorite and epidote (Pontual et al., 1997a). In general, the loss of the number of feldspars and hornblende to clays in the advanced, intermediate and argillic zone, and the addition of quartz in the silicified alteration zones are not yet quantified. All this makes the mineral assemblages and alteration zoning incomplete. Particularly the primary host of the gold mineralization, the vuggy silica (dominated by quartz), the silicified zone (e.g., quartz, adularia & barite), the advanced argillic zone (e.g., a bit of quartz), and the intermediate argillic zone (a bit of quartz and unaltered k-feldspar) cannot be quantified with the application of SWIR remote sensing.

Furthermore, mineral reactions from primary mineral to alteration minerals have not been able to be quantified yet based on an altered and non-altered rock sample study with SWIR and LWIR infrared spectroscopy methods in the epithermal system due to the incomplete characterization of the minerals in the rock samples.

Therefore, this research characterizes the current mineral assemblages in the rock samples of the Rodalquilar system by combining SWIR (1 $\mu\text{m}$  – 2.5  $\mu\text{m}$ ) and LWIR (8 $\mu\text{m}$  -11.5 $\mu\text{m}$ ) hyperspectral images. It uses the 20 scanned rock samples that were used in the study of Contreras Acosta (2017) plus an additional 36 samples that we selected from the ITC rock sample storage. The results of the two sets of image files were combined to determine the mineral content of the rock samples and link this to the alteration zones quantitatively. Furthermore, the assignment of the rock samples into alteration zones were compared with the existing alteration map. Finally, the results were assessed on the added value of having an additional wavelength range of the LWIR and the refinement of the mineral assemblage and alteration zonation of the Rodalquilar high sulfidation epithermal system.

#### **1.4. Objectives**

The main objective is to produce an improved and detailed alteration zoning including the silicic and advanced argillic alteration zones using the combined SWIR-LWIR high spatial resolution hyperspectral imaging techniques of rock samples.

##### **1.4.1. Specific objectives**

The specific objectives include;

1. To determine the current mineralogic composition of the rock samples with infrared techniques
2. To identify textures from the SWIR and LWIR image data
3. To combine the SWIR and LWIR data for determining significant mineral assemblages in the rock samples
4. To distinguish and assign the rock samples into the different alteration zones based on their current mineralogy

#### **1.5. Research questions**

1. Which minerals are determined from the image of the rock samples of the Rodalquilar in the SWIR and LWIR range?
2. What type of textures can be identified from SWIR and LWIR image data?

3. How to combine the results from SWIR and LWIR image of the rock samples for high sulfidation epithermal system characterization?
4. Do the rock samples conform to the alteration zones of the Rodalquilar system as mapped by the previous works?
5. Do the rock samples identify or improve the subclassifications of the alteration zones?
6. What is the difference between the current SWIR-LWIR result and existing maps?

## 1.6. Hypothesis

1. Minerals expected to be found by extending the wavelength range with LWIR are quartz, feldspar, pyroxene, clay minerals, sulfate, carbonate and iron oxides
2. Subclassification of alteration zones are expected to be found
3. The percentage of the dominant minerals are assumed to be based on the alteration zones

## 1.7. Research structure

This research paper is structured into six chapters. [Chapter 1](#) introduces the research background and justification, previous work, research problem, research objectives, research questions, and hypothesis. [Chapter 2](#) description of the study area includes location, geological setting, alteration and mineralization, and SWIR-LWIR spectral characteristics. [Chapter 3](#) comprises research datasets and methods; starting from sample selection, image acquisition, pre-processing, endmember extraction, mineral mapping, SWIR and LWIR combining, to data analysis and interpretation methods. [Chapter 4](#) present the results of the pre-processing, endmember extraction, mineral mapping, SWIR, and LWIR combining, and alteration zones. [Chapter 5](#) discusses the methods employed and results obtained from this research, including assigning the rock samples to alteration zones, the comparison between altered and unaltered rock samples, and comparison with existing maps. [Chapter 6](#) Conclusion and Recommendation.

## 2. DESCRIPTION OF THE STUDY AREA

This section introduces the general description of the study area concerning the location, geological setting, alteration and mineralization, and SWIR-LWIR spectral characteristics of the epithermal system.

### 2.1. Location

The study area is located in the Cabo de Gata volcanic field, Almeria province, southeastern Spain (Figure 2.1). It is well known for its gold and base metal mineralization in the volcanic caldera-related epithermal deposit.

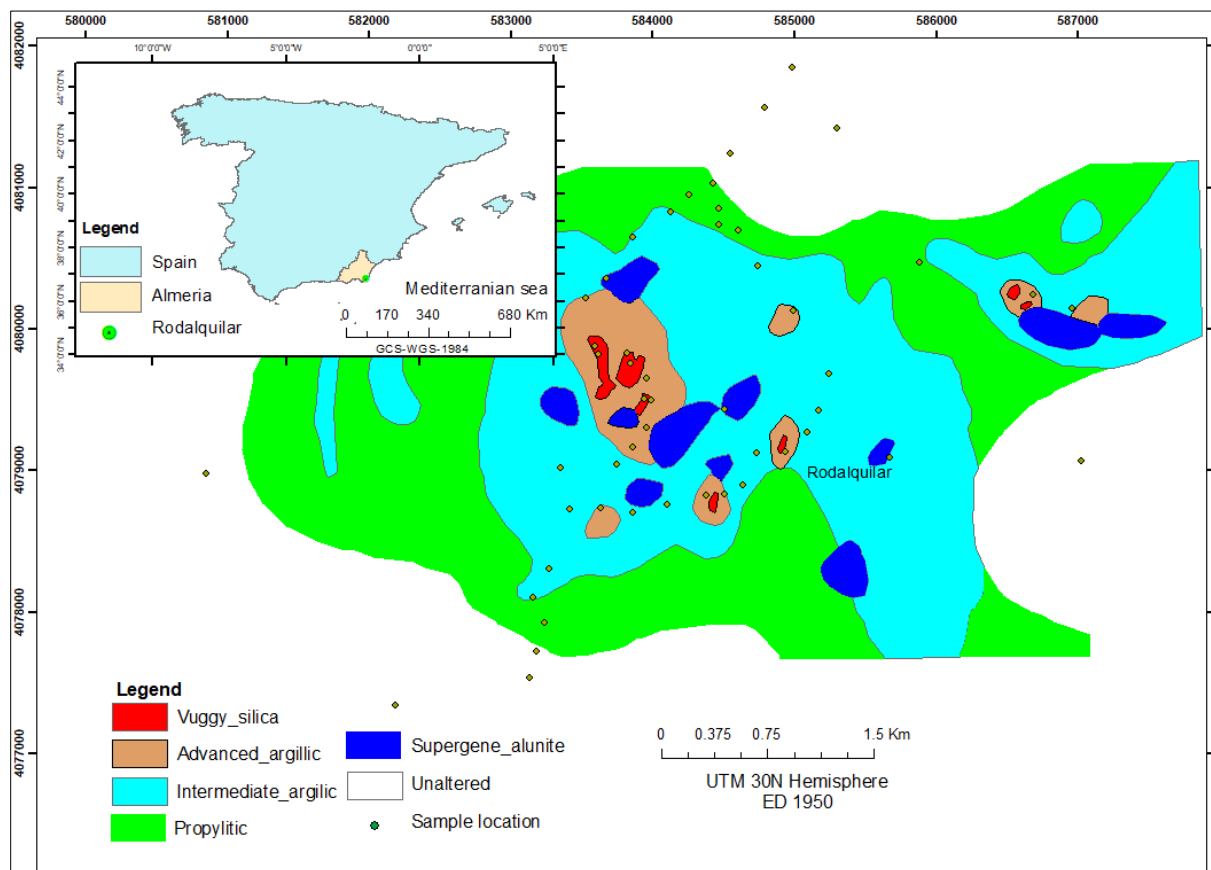


Figure 2.1: Alteration map of the Rodalquilar area, (modified after Arribas et al., 1995) which show alteration patterns, sample locations, and the study area of this work in the black inset rectangle.

The geology and hydrothermal alteration of the area has been carefully mapped and well summarized by Rytuba et al. (1990); Arribas et al. (1995) and Bedini et al. (2009) which makes Rodalquilar an excellent area to develop and test remote sensing and spectroscopic methods for mineral exploration (Van der Meer et al., 2018). This section outlines the general description and geological map based on these references.

## 2.2. Geological setting

Geologically the area is a volcanic arc caldera formed due to subduction of the oceanic plate underneath the continental plate. The caldera is an oval-shaped structure that developed in an older andesitic volcanic field which consists of calc-alkaline volcanic rocks of the late Tertiary age and Quaternary sedimentary rocks such as limestone/sandstone which are intruded by late-stage numerous intrusive rocks and hydrothermal veining. A detailed discussion of the lithology and geologic history can be found in several reports (e.g., Rytuba et al. (1990) and Arribas et al. (1995)).

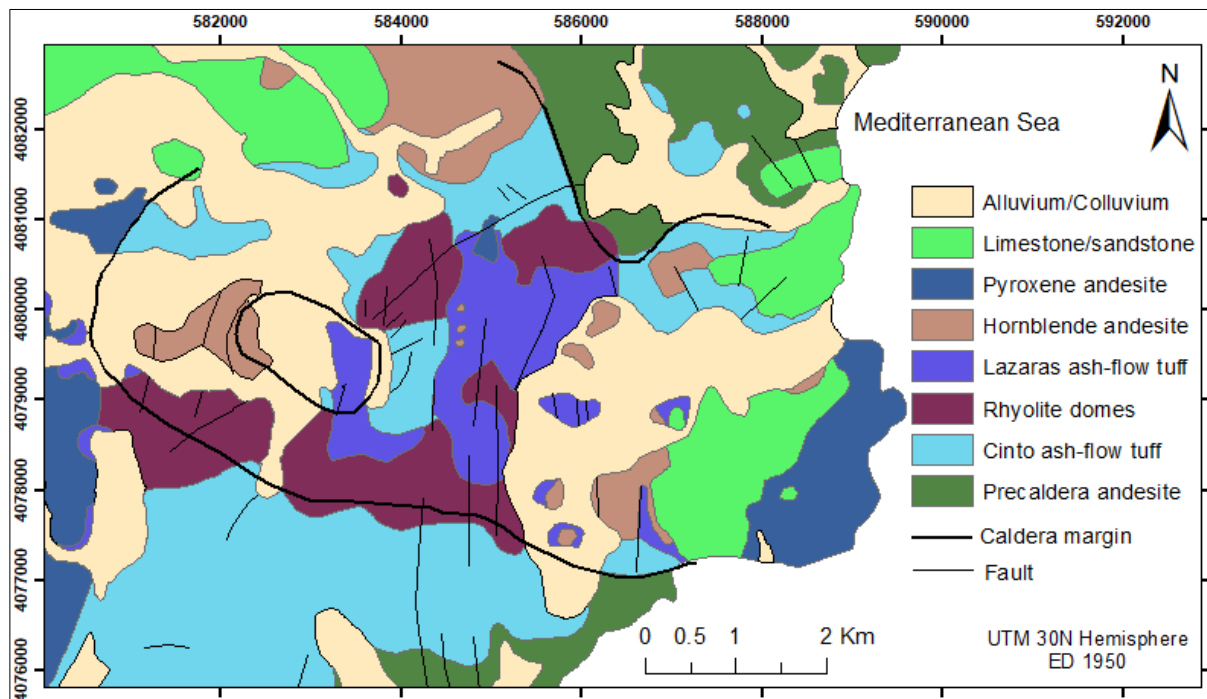


Figure 2.2: Geological map of Rodalquilar (after Arribas et al., 1995)

The volcanic rocks range in composition from mafic (pyroxene/hornblende andesite) to felsic (rhyolite). The lithologies according to chronological order from older to younger are pre-caldera andesite and cinto ignimbrites, rhyolite domes, las Lazarus ignimbrite, hornblende andesite flows, pyroxene andesite, limestone/sandstone, and alluvium/colluvium.

## 2.3. Alteration and mineralization of the Rodalquilar epithermal system

The formation of the alteration zones is described in section 1.1. Different places may have different mineral assemblages due to the difference in the composition of the lithologies, hydrothermal fluids and temperature of the fluids. This section summarizes the alteration and mineralization of the Rodalquilar area based on Arribas et al. (1995). The classification of the alteration zones is according to the important mineral assemblages and their dominance of minerals in the rock.

In Rodalquilar, the calc-alkaline volcanic rocks experienced an extensive hydrothermal alteration which resulted in the formation of new minerals from high temperature to low temperature as silica, alunite, kaolinite, montmorillonite, and chlorite. Two styles of mineralization are associated with those alteration zones such as high sulfidation Au-(Cu-Te-Sn) ores and low sulfidation Pb-Zn-(Cu-Ag-Au) quartz vein mineralization. This research is focusing on the high sulfidation part of the area which is located in the central part of the Rodalquilar volcanic field. The reason being that the gold production of the world comes mostly from high sulfidation epithermal deposits (Morishita & Nakano, 2008). The sufficient gold

concentration in the area is also located in the north-south structures (Cunningham et al., 1990) which is aligned along the selected transect line or the sample locations of this research.

The detailed mineral assemblages in alteration zones in Rodalquilar are summarized in Table 2.1. The silicic zone is dominated by vuggy silica formed by extreme leaching of the original rock. It is associated with the high sulfidation gold mineralization which is related to the high-temperature hydrothermal fluid circulation. The advanced argillic zone is divided into two, namely quartz dominated by alunite, and quartz dominated by kaolinite and illite. However, the two subclassifications of the advanced argillic zone in Rodalquilar area was previously mapped as one advanced argillic zone. The intermediate argillic zone is dominated by quartz and kaolinite. The dominance of mineral assemblages varies from place to place. For example near the advanced argillic zone kaolinite-dickite is abundant, whereas in the outer zone closer to the propylitic zone, illite-smectite become the dominant minerals. The argillic zone is dominated by illite, quartz, pyrite. The argillic zone is mapped as an intermediate argillic zone in the Rodalquilar epithermal system. The propylitic zone consists of quartz, chlorite, K-feldspar, illite-smectite. This zone is here spatially mapped on the periphery of the area. The other zone is a supergene which is characterized by alunite, quartz, kaolinite, jarosite and amorphous silica mineral. It occurs creating an overprinted pattern with the primary mineralization of the advanced argillic zone (Figure 2.3). They are formed due to weathering or low-temperature hydrothermal alteration of the primary mineralization (a mineralization form due to high-temperature hydrothermal fluids circulation). Therefore, alunite, the kaolin group and quartz minerals in the Rodalquilar can be the result of a primary or a supergene process.

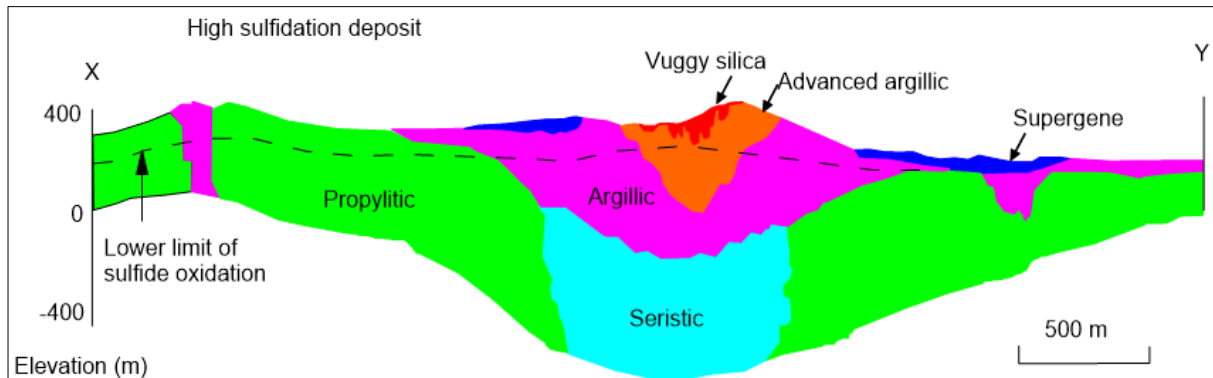


Figure 2.3: cross-section showing alteration zones in Rodalquilar (after Arribas et al., 1995)

However, the supergene minerals can be distinguished from the primary minerals based on differences in degree of structural order or crystallinity structure development of the minerals. For example, high crystalline kaolinite, dickite, nacrite, and quartz indicate high-temperature fluid which is related to primary minerals. The poorly crystalline kaolinite and hydrated halloysite indicate weathering or low-temperature hydrothermal fluids which are related to supergene minerals (Garcia, 2013). This crystallinity can be identified using infrared spectroscopy study.

Table 2.1: Significant mineral assemblage in the alteration zones of the Rodalquilar epithermal system. The “+” sign indicates the significant and dominant minerals in the zone. The “,” after “+” signs represent the presence of minerals in the zone but not dominant.

Silicic zone	Advanced argillic		Intermediate argillic zone	Argillic zone	Propylitic zone	Supergene
	1 <sup>st</sup>	2 <sup>nd</sup>				
Vuggy porous quartz, opal, chalcedony. Also some alunite, kaolinite, zunyite, aluminium sulfate-phosphate	Quartz+alunite, kaolinite	Quartz +kaolinite+illite, Dickite, pyrite, pyrophyllite	Quartz, kaolinite, illite, illite/smectite, k-felspar, hematite, goethite, pyrite, minor alunite, pyrophyllite and diaspore	Illite, quartz, pyrite with less amount of rutile. Kaolinite, diaspore, alunite are rare	Quartz, chlorite, K-feldspar, vermiculite, illite, smectite, hematite, goethite, primary plagioclase, less calcite	Supergene Alunite, quartz, kaolinite, jarosite, hematite, hydrated amorphous silica

#### 2.4. SWIR and LWIR Spectral characteristics of the high sulfidation epithermal system

This section discusses the spectral characteristics of the alteration minerals in the alteration zones associated with the high sulfidation epithermal system in SWIR and LWIR wavelength ranges. Several studies characterize an epithermal system using the SWIR range. However, for the high spatial resolution hyperspectral LWIR range, no studies have been done so far. For the SWIR range, Pontual et al. (1997a) have already described spectra of SWIR active minerals in detail in “*Geologically based spectral analysis guides for mineral exploration*” (GMEX-version 1-volume 4 book). Therefore, this section is mainly focusing on LWIR spectral characteristics. However, only the spectral features in SWIR are presented.

High sulfidation epithermal systems are characterized by alteration zones dominated by vuggy silica and advanced argillic zones (Hedenquist et al., 2000) formed by high temperature acidic hydrothermal fluids. The mineral assemblages and zonation outlines decreasing temperatures outward from the vuggy silica vicinity of the center of the mineralization and outward advanced argillic to intermediate argillic to propylitic. The spectral characteristic in different alteration zones is described below and is based on the USGS, ASU and JHU spectral libraries.

##### Silicic zone

This zone is characterized by mainly quartz, chalcedony, and opal. The diagnostic feature for quartz is the doublet feature at 8.24  $\mu\text{m}$  and 9.24  $\mu\text{m}$  with an emissivity peak at around 8.6  $\mu\text{m}$ . For opal, the first emissivity minimum is at 8.90  $\mu\text{m}$ . For chalcedony, small emissivity minima can be found at around 8.15  $\mu\text{m}$ . The main differences between chalcedony and opal in SWIR range are the small absorption features at 1.5  $\mu\text{m}$  and 1.95  $\mu\text{m}$ .

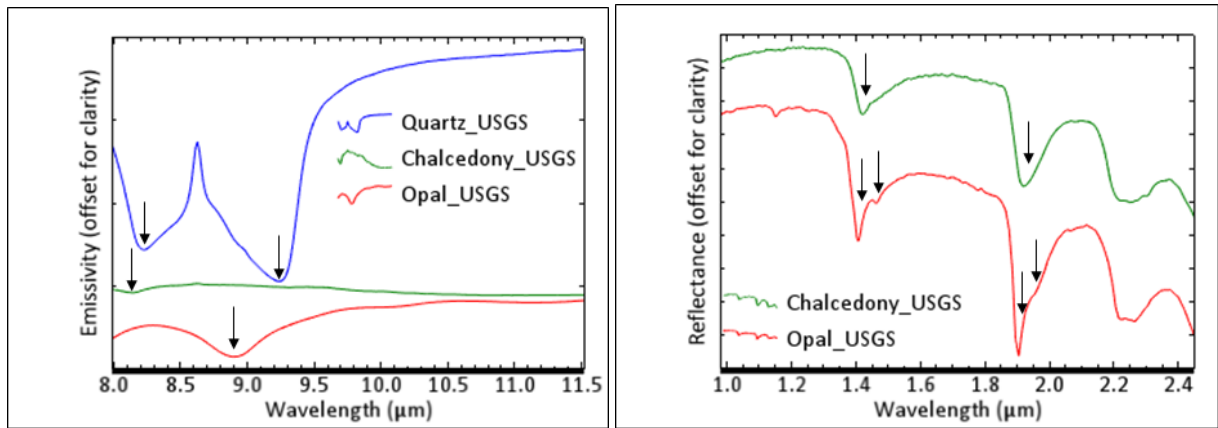


Figure 2.4: Emissivity and reflectance spectra from the silicic alteration zone in the LWIR and SWIR wavelength range. The arrows indicate the emissivity minima features in LWIR and absorption feature in SWIR.

### Advanced argillic zones

This zone is characterized by quartz, alunite, diaspore, pyrophyllite, and dickite. Alunite has a diagnostic minimum emissivity feature at around 8.5  $\mu\text{m}$ , a broad feature between 8.8  $\mu\text{m}$  and 9.1  $\mu\text{m}$ , and a small feature at around 9.7  $\mu\text{m}$ . Diaspore has a very shallow depth broad feature between 8.6  $\mu\text{m}$  to 10.4  $\mu\text{m}$ , and the deepest is around 8.7  $\mu\text{m}$ . Pyrophyllite has narrow and deep features at 8.6  $\mu\text{m}$  and 9.11  $\mu\text{m}$  and small feature at 10.45  $\mu\text{m}$ . Dickite has diagnostic features at around 8.8  $\mu\text{m}$ , broad feature between 9.2  $\mu\text{m}$  and 9.5  $\mu\text{m}$ , and small doublet feature at 9.8-9.9  $\mu\text{m}$ . The main differences in SWIR range are indicated by the black arrow.

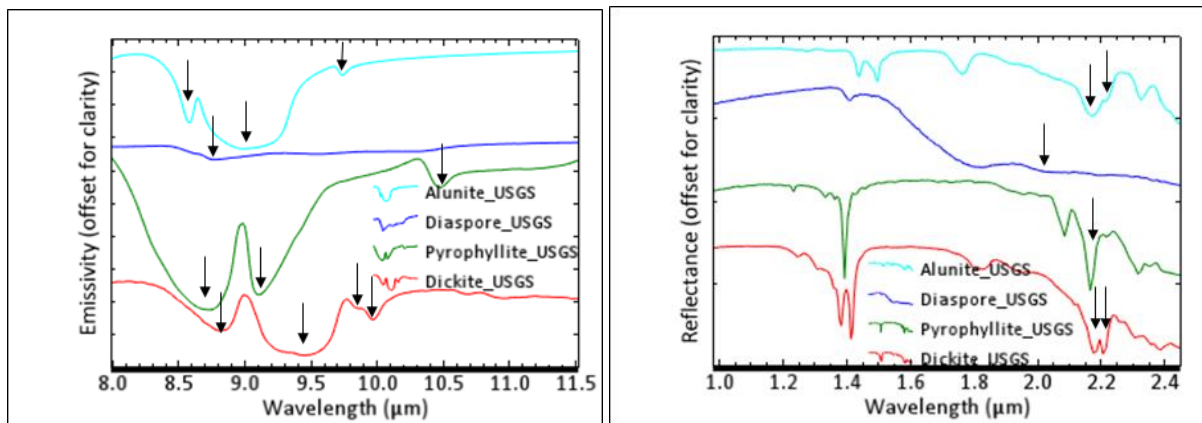


Figure 2.5: Emissivity and reflectance spectra from the advanced argillic zone in the LWIR and SWIR wavelength range. The arrows indicate the emissivity minima features in LWIR and absorption feature in SWIR.

### Intermediate argillic zone

Characterized by quartz, kaolinite, dickite, pyrophyllite, and illite. Kaolinite has three typical features at 8.8  $\mu\text{m}$ , 9.4  $\mu\text{m}$ , and 9.9  $\mu\text{m}$ . Illite has two features at 9.5  $\mu\text{m}$  and 9.09  $\mu\text{m}$ . In SWIR range kaolinite has a doublet absorption feature at 2.20  $\mu\text{m}$  and 2.16  $\mu\text{m}$  and the small absorption feature at 1.8  $\mu\text{m}$  indicates a crystalline kaolinite. Illite has a single absorption feature at 2.20  $\mu\text{m}$ .

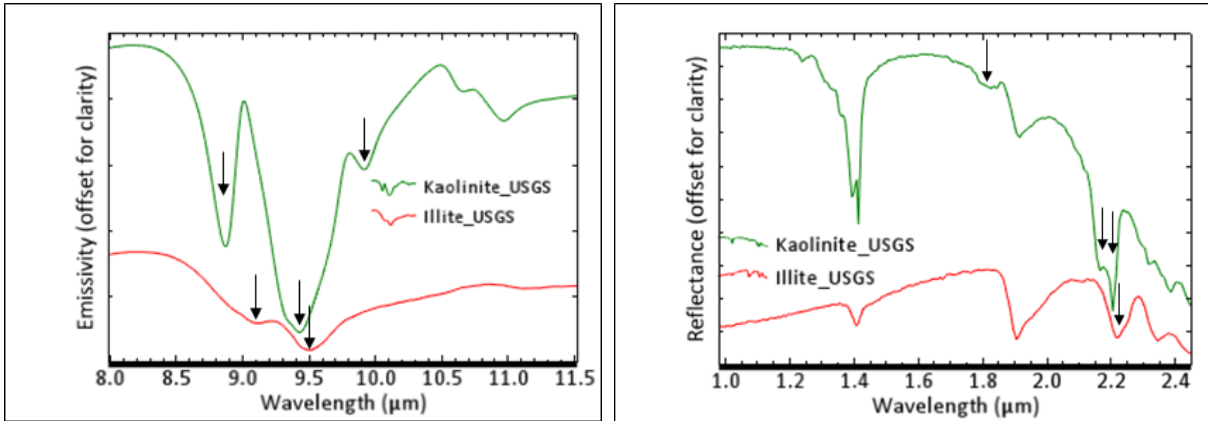


Figure 2.6: Emissivity and reflectance spectra from the intermediate argillic zone in the LWIR and SWIR wavelength range. The arrows indicate the emissivity minima features in LWIR and absorption feature in SWIR.

### Argillic zone

Characterized by illite, illite-smectite, smectite. Emissivity minimum feature of illite-smectite occurs at 9.45  $\mu\text{m}$ , near 8.66  $\mu\text{m}$  and small feature at 8.44  $\mu\text{m}$ . For smectite, features have at around 9.39 and 8.74  $\mu\text{m}$ . In SWIR range smectite has a first absorption feature at 2.20  $\mu\text{m}$  and deep narrow water absorption features at 1.9 and 1.4  $\mu\text{m}$ .

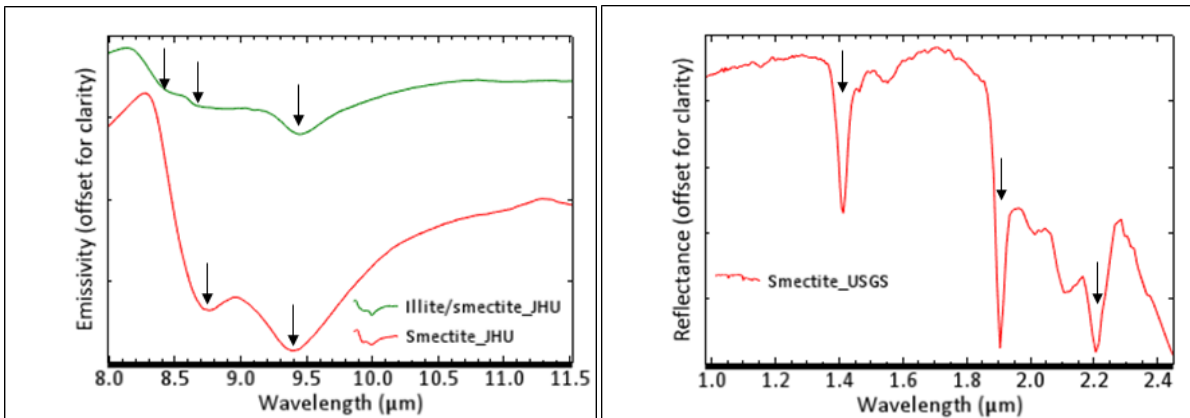


Figure 2.7: Emissivity and reflectance spectra from the argillic alteration zone in the LWIR and SWIR wavelength range. The arrows indicate the emissivity minima features in LWIR and absorption feature in SWIR.

### Propylitic zone

Characterized by quartz, chlorite, epidote, calcite and smectite minerals. Chlorite has three diagnostic emissivity minimum at 9.34  $\mu\text{m}$ , 9.74  $\mu\text{m}$ , and 10.40  $\mu\text{m}$ . Epidote has a broad shallow feature between 8.80 - 9.61  $\mu\text{m}$  and between 10.12-10.49  $\mu\text{m}$  and centered emissivity peak at around 9.83  $\mu\text{m}$ . Calcite has a single narrow, deep feature at 11.32  $\mu\text{m}$ . In SWIR range chlorite and epidote are difficult to distinguish both have first absorption feature at 2.33  $\mu\text{m}$ . Calcite first absorption feature is at 2.34  $\mu\text{m}$ .

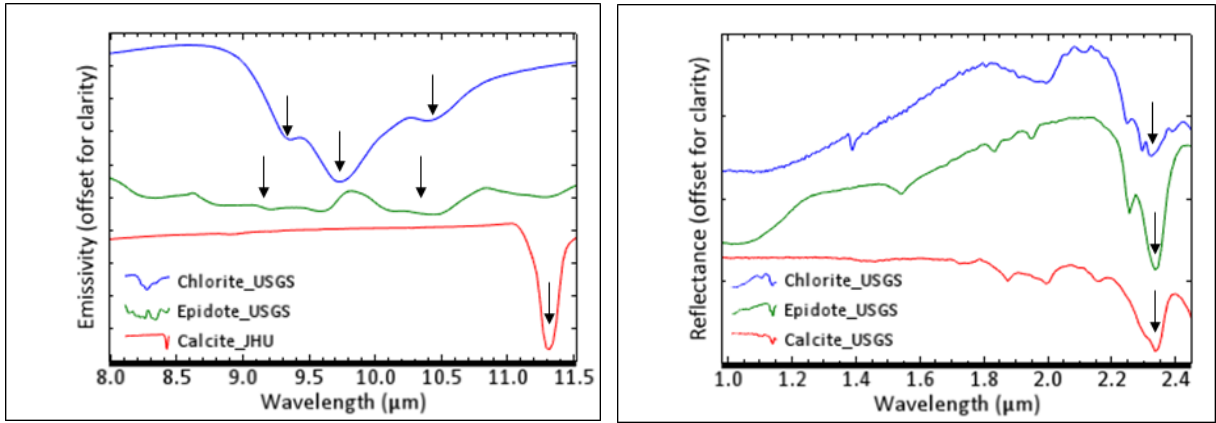


Figure 2.8: Emissivity and reflectance spectra from the propylitic alteration zone in the LWIR and SWIR wavelength range. The arrows indicate the emissivity minima features in LWIR and absorption feature in SWIR.

## 3. DATASETS AND METHOD

SWIR and LWIR image data of surface rock samples were used to characterize alteration minerals associated with the high sulfidation epithermal system. This section explains the different approaches to achieve the research objectives. The methods cover a selection of rock samples, image acquisition of the surface of the rock samples. Pre-processing (improving the spatial and spectral image quality), image processing (wavelength mapping, endmember extraction, and mineral mapping). Followed by SWIR and LWIR result integration, assign the rock samples into the alteration zone and comparison with the existing alteration zone map. The different elements of the methods and datasets used are described in detail below.

### 3.1. Datasets

#### 3.1.1. Rock samples

More than 200 rock samples of Rodalquilar are available in the ITC laboratory. The samples were collected by ITC students and staff in different research campaigns in the Rodalquilar Caldera Complex in south-eastern Spain. Among the available samples, 45 Altered and 11 unaltered rock samples in a total of 56 samples were selected for image analysis, because the sample locations are representative for the specific study area and the high sulfidation epithermal area. The selection of the samples was based on the spatial distribution of the samples and spatial alignment along a transect line and crossed all the alteration units according to the existing map of Arribas et al. (1995). Altered and unaltered rock samples were distinguished based on physical characteristics (grain size, texture, and mineral composition) of the rock samples using a hand lens. The geographic location of the samples is presented in Appendix 4. The rock samples from younger to older represent alluvium/colluvium, pyroxene andesite, hornblende andesite, Lazarus ash-flow tuff, rhyolite domes, and cinto ash-flow tuff. The sample codes MRE and CH in the entire paper stand for Mineral Resource Exploration and Chris Hecker respectively.

One unaltered sample of each rock unit was selected to represent the composition of that rock unit before alteration. Also, the samples 04MRE042, 04MRE042(1) and 04MRE042(2) are collected from the same rock unit out of curiosity. The rock samples were sliced using a rock cutter called Lortone slab saw, at the Geoscience laboratory of the ITC faculty laboratory. The first step was to cut the rock samples with a rock saw through the representative part of the rock surface to avoid shadows in the image due to the irregular surface. After the sample is cut, the surface of the sample was washed to remove cuttings, and it was dried in the oven at 50°C for one day in order to remove absorbed water from cutting the samples and washing. A desiccator was used to prevent entering moisture from the atmosphere. Furthermore, pressurized air was used to remove the remnant dust after the sample was dry.

#### 3.1.2. Proximal sensing data acquisition

A Specim SWIR3 hyperspectral camera and a Specim Aisa Owl hyperspectral camera were used for the image acquisition of the surface of the rock samples in the SWIR and LWIR wavelength range respectively. For the SWIR image files, the samples were scanned in dark laboratory conditions and for the LWIR in bright laboratory conditions. Technical specification of the instrument and settings used are given in Table 3.1.

Table 3.1: Instrument specifications and setting

Parameters	SWIR wavelength range	LWIR wavelength range
Service Provider	ITC	BGR
Spectral range (nm)	894.51 - 2511.11	7704.43 - 12571.90
Spatial resolution ( $\mu\text{m}$ )	260	400
Spectral resolution (nm)	5.6	48
Number of bands	288	101
Frame rate (Hz)	38.9	21.32
Speed (mm/s)	10	9.8
Exposure time (ms)	2.1	0.95

Laboratory imaging spectroscopy was performed on the prepared rock samples to acquire high spatial and spectral resolution image files. The samples were acquired in SWIR range using the Specim Hyperspectral camera at the Geoscience Laboratory in the ITC Faculty building, University of Twente, Enschede, The Netherlands. Furthermore, the same surface position of each rock sample was scanned in the LWIR wavelength range using the AISA-Owl hyperspectral camera located in the Federal Institute for Geosciences and Natural Resources (BGR), Hannover, Germany. During the image acquisition, the surface of rock samples was placed horizontally in a wooden box filled with quartz sand to level all samples as shown in Figure 3.1.

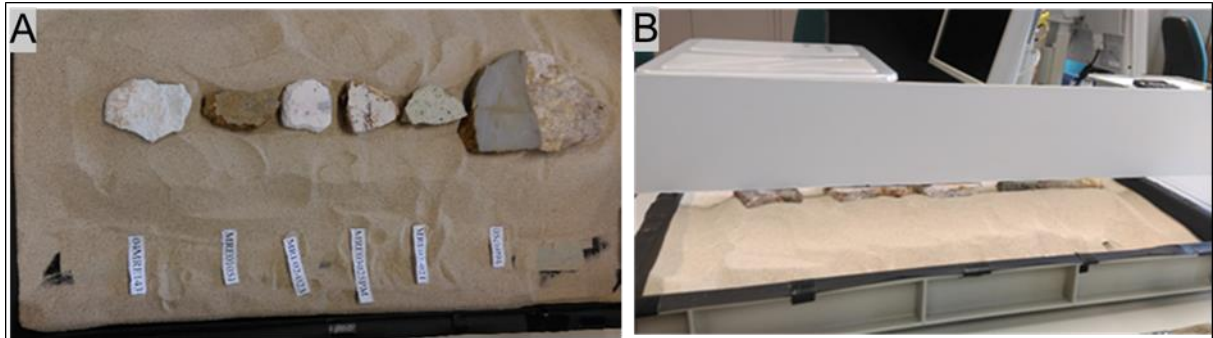


Figure 3.1: Prepared surface rock samples ready for image acquisition. A) Samples on the wooden box filled by sand and B) leveling the surface of the rock samples.

### 3.2. Research Methods

To characterize the surface of the rock samples using SWIR and LWIR image data several steps have been employed for understanding the high sulfidation epithermal system. These steps include image pre-processing and processing, and data analysis and interpretation. Description of the steps are as follows, and the methodological flowchart is presented in Figure 3.2.

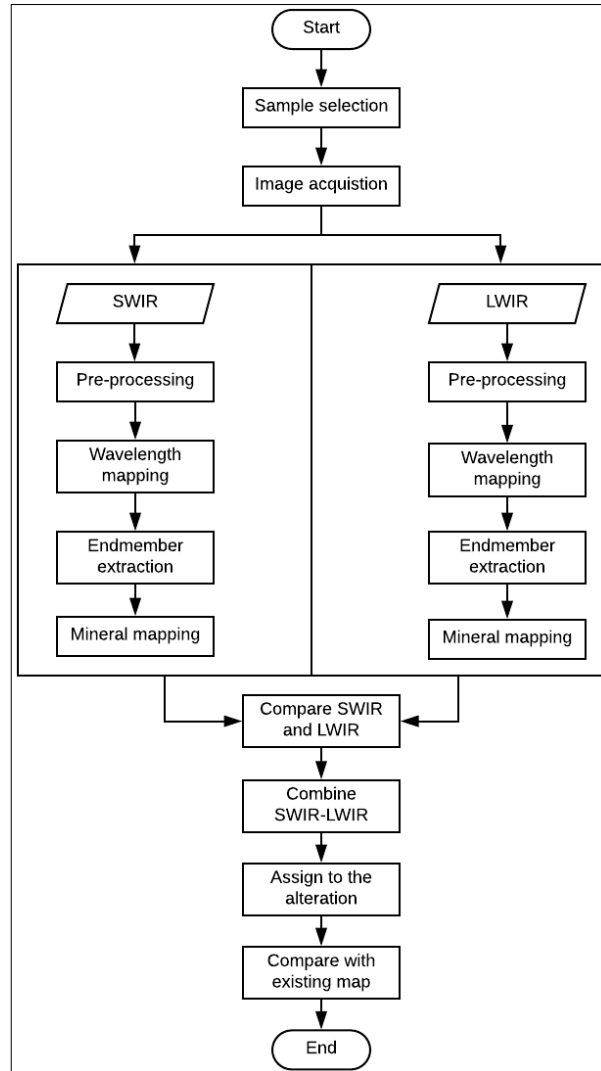


Figure 3.2: Methodological flow chart

### 3.2.1. Image pre-processing

The acquired image cubes were pre-processed to improve the image quality before further processing (e.g., endmember extraction and mineral map) by suppressing the noise but minimize the impact on the spatial and spectral features. Four steps of image pre-processing have been employed for each of the acquired image cubes of SWIR and LWIR files. The first step was converting the recorded image data (raw DN value) to the reflectance images. This was performed using HypPy3 software by using a special tool *calibration of dark and white reference*. The LWIR reflectance image file was converted to an emissivity image file using Kirchoff's law (emissivity = 1-reflectance) using a spectral math tool in ENVI software. The second step was masking the reflectance image by removing the unwanted extra space outside the sample margin which does not represent the sample data. The background value was assigned to NaN to avoid its effect in the statistics of the image. This was done using ENVI software by applying to *resize data (spatial-spectral)* subset tool and manually selecting the region of interest (ROI). Also, noisy spectral bands were removed in all data cubes using a spectral subset in ENVI (Figure 4.2). For example, SWIR image files Band 1-16, and 288 were removed. The number of bands reduced from 288 bands to 271 bands corresponding to the 985 nm to 2505 nm wavelength range. For LWIR image files bands 1-6 and bands 80-101 were removed. The images were reduced from 101 bands to 73 bands corresponding to the 7996 nm to 11501 nm wavelength range. The removed bands do not affect the research objectives because the minerals of interest can be identified

within the subsetted wavelength ranges. The third pre-processing step was correcting the bad columns in the SWIR image file data caused by the Specim SWIR3 camera. This was performed using a HypPy3 special tool using a *fix SWIR 8<sup>th</sup> sample*. The algorithm replaces every eighth column by the average of its neighboring two columns (Bakker, 2018). The final pre-processing step was smoothing of the spectral data; it reduces the noise present in the spectra. For SWIR image files spatial-spectral filter using *Fast mean filter (1+5+1)* tool in HypPy3 software was applied to remove outliers in the pixel and noise that are not indicative of absorption feature of minerals. For LWIR image files forward and backward MNF transform (Green et al., 1988) was applied to suppress the noise with the minimum spectral feature impact on LWIR image files. The MNF transform filters out the noise components and sort out according to the image quality. Visual inspection of individual components was used to select components that have more information (i.e., signal bearing)the (Figure 4.5). The selected components for each image were then used to drive inverse transform and produce full image cubes which have 73 bands. Finally, the image data cubes were produced that contained a lower noise component than the original data.

Following to the image pre-processing, Image processing was performed on the pre-processed SWIR contiguous 271 spectral bands from 985 nm to 2505 nm and LWIR contiguous 73 spectral bands from 7996 nm to 11501 nm. The purpose was to visualize the absorption and emissivity spectral features, to extract endmembers, to quantify the minerals by classifying the pixels of the image into the dominant minerals.

Table 3.2: The main activities and purposes of image processing.

Activity	Purpose
Wavelength mapping	Highlight the minerals present in each pixel of the image based on the minimum reflectance/emissivity value of the wavelength.
Hand picking endmember extraction	Generate appropriate endmembers. The results are compared with USGS, JHU and ASU library and with spectral interpretation field manual Pontual et al., (1997b)
Spectral angle mapper (SAM) classification	Produce a mineral map and determine mineral abundances in the rock samples.
SWIR - LWIR combining	To quantify the significant mineral assemblages in the rock samples. Then used to assign the rock samples into the alteration zones

### 3.2.2. Wavelength mapping

The wavelength mapping method was applied, which provides a simple and straight forward tool for highlighting the dominant minerals in each pixel and mineral patterns in the image based on their deepest absorption feature or low reflectance/emissivity in the spectra. It is advantageous to automatically stretch the interpolated depth values of the absorption features to increase the saturation and show patterns clearly (W. H. Bakker, 2012). Contreras Acosta (2017), also used wavelength mapping to get a first overview of the dominating minerals in each pixel and extract endmembers for a subset of the rock samples of this research and identified appropriate endmembers. For this study, the wavelength map was used to assist endmember extraction and to compare the highlighted minerals in each pixel and patterns of the SWIR and LWIR image files. To produce a wavelength mapping hyperspectral python (HypPy3) software was used. First, the wavelength of the minimum was run to obtain the wavelength of the lowest value of the spectrum (W. H. Bakker, 2012). For SWIR image files the minimum wavelength was produced in the range between 2100 nm to 2400 nm because minerals in SWIR range have a diagnostic absorption feature in that range and also

in order to exclude the water absorption feature at 1900 nm. For LWIR image files the full range from 8000 nm to 11500 nm was created. The resulting image is a one band image in which the values denote the wavelength. Then this result was used for wavelength mapping and produced a colour map using Hue Saturation Value (HSV) fusion of an interpolated local wavelength of a minimum combined with the interpolated depth of the local minima (W. H. Bakker, 2012). The different colours from the resulting fused image highlight the dominant minerals present and the abundance can be inferred from the depth in the legend.

### 3.2.3. Endmember extraction

Mineral endmember extraction was applied to the pre-processed SWIR and LWIR wavelength range image files. In order to determine the mineral contents in the rock. The endmembers were extracted manually using hand-picking from each pre-processed 56 image files assisted by the wavelength maps and physical observation of the samples.

For the SWIR range, the wavelength map and physical observations of the samples were used to assist the endmember collection because in the SWIR range the active endmember minerals are highlighted in different colour contrast since they have diagnostic narrow deepest absorption features. While in case of LWIR range the emissivity minima of the active minerals in LWIR range have broad and overlapping emissivity minima features which makes it tricky to discriminate the quartz minerals from the clay minerals. However, quartz has a deep depth emissivity minima spectral feature compared to the other emissivity minima spectral feature of clay minerals in the epithermal system. Therefore, the RGB combination of first interpolated depth, first interpolated minimum wavelength and second interpolated minimum wavelength was applied (Figure 3.3 B). Also, physical observations of the samples were used to confirm the endmember minerals identified.

Most of the LWIR wavelength maps of the rock samples are highlighted by green colour (Appendix 3). As an illustration (Figure 3.3 A) shows the LWIR wavelength map of sample 04MRE055. The minimum emissivity value of the wavelength is highlighted by a bright green colour, dark green colour and a few pixels blue colour.

From each rock sample, the endmember minerals were collected. In total from SWIR range, 107 endmembers and 105 endmembers from LWIR were extracted. Then manual endmember screening was applied to remove duplicates and mixed spectra. Finally, 13 candidate endmembers from SWIR and 13 candidate endmembers from LWIR were collected and compared with USGS, JPU, ASU library, and the spectral interpretation field manual Pontual et al. (1997a) for mineral identification and naming. Finally, the extracted endmembers were used for mineral mapping.

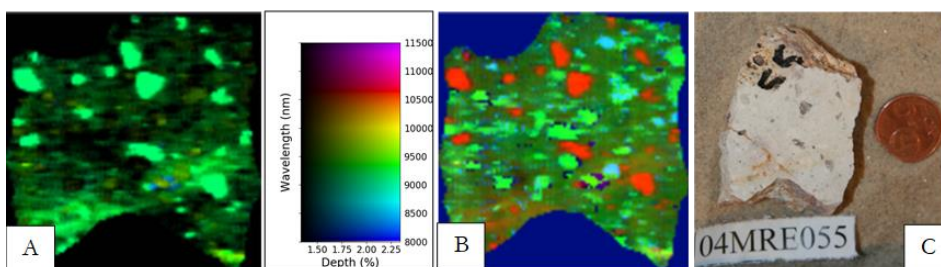


Figure 3.3: A) wavelength map of sample 04MRE055, B) RGB=first interpolated depth, first minimum wavelength, second minimum wavelength. The endmembers were collected from the highlighted colour, red represent (quartz), and the rest colours are clay minerals and C) hand specimen.

### 3.2.4. Mineral mapping

For this study, the SAM method was applied to produce mineral maps of the SWIR and LWIR image files. Because SAM is the most widely used mapping method in hyperspectral remote sensing (Van der Meer & Van der Werff, 2007) and it is straightforward and easily accessible in ENVI as the spectral tool.

Moreover, for high spatial resolution (0.4mm) image it is sufficient to use SAM with the rule classifier. Because this research is aiming at the classification of the rock samples into the different alteration zones, the classification is mainly based on the dominant mineral assemblages of the rock. Therefore, SAM classifies the dominant minerals in the pixel. In previous work on SWIR image files by Contreras Acosta (2017), the SAM method was also recommended to get the dominant minerals per pixel using a 0.1 radians threshold. This technique uses the reference endmembers extracted from the pre-processed image and the pre-processed image files. The algorithm matches the image spectra with the reference endmembers. It determines the similarity between two spectra by calculating the spectral angle between them. The output from SAM is a set of rule images (one per endmember) that can be classified using the rule classifier. From the statistics of the classified image, the abundance of the dominant mineral per pixel was estimated. During the classification, a single value was selected, and the maximum angle (radians) set 0.1 for SWIR image files and 0.05 for LWIR image files.

### 3.2.5. SWIR-LWIR combining

The SWIR and LWIR range mineral map results were combined to get the significant mineral assemblages of the rock samples and then to classify the rock samples into alteration zones. Three steps have been employed to combine the SWIR and LWIR results. The **first step** was a comparison of the SWIR and LWIR range mineral map results by observing the mineral assemblages and distributions in the rock samples. The **second step** was selecting the three most dominant minerals from both the SWIR and LWIR ranges from the quantified percentage of the SAM result (Table 3.3), for all the rock samples see (Appendix 6). The three dominant minerals were chosen because in the epithermal system the alteration zones have two to three dominant mineral assemblages per alteration zone. For example in Arribas et al. (1995) alteration zones in Rodalquilar epithermal system and alteration zones in general epithermal system (Hauff, 1983; Arribas, 1995; Hedenquist et al., 2000; Pirajno, 2009). However, in this study less abundant but important minerals were also considered to be included in the assemblage of the rock samples, because the presence of an important mineral indicates hydrothermal activity. For example, the presence of an important mineral from the *kaolin group* (highly crystalline kaolinite, nacrite, dickite, dehydrated halloysite) of more than 2% in felsic igneous rocks reveals kaolinization/argillic alteration. In this case, it means that K-feldspar altered to kaolinite due to hydrothermal fluids. The presence of more than 45% *quartz* in mafic rocks indicates the addition of quartz/silicification due to hydrothermal fluids. *Alunite* (more than 2%) in potassium-rich volcanic rocks (rhyolite-andesite) were also included to the mineral assemblage because they indicate the action of sulfuric acid bearing solutions on these rocks during the oxidation and leaching of metal sulfide deposit. *Pyrophyllite* (more than 2%) are also indicators of high-temperature hydrothermal activity near silicic/advanced argillic alteration zone. The **third step** was combining the selected minerals from both ranges and putting them in order based on significant mineral percentage. Poorly crystalline kaolinite, jarosite are excluded because they are related to weathering products of K-feldspar and oxidation of iron sulfides mineral respectively. In addition anorthite, hydrated halloysite and pyroxene were also excluded because they do not indicate hydrothermal activity.

Table 3.3: SAM-Mineral abundance of selected rock samples

Sample code	SWIR-Mineral abundance (%)												LWIR-Mineral abundance (%)							
	Alunite	Alunite+water	Dickite	Pyrophyllite	Nacrite	Chlorite	D-Halloysite	H-Halloysite	Jarosite	PX-Kaolinite	HX-Kaolinite	Montmorillonite	Nontronite	Alunite	Halloysite	Jarosite	Kaolinite	Nontronite	Quartz	K-feldspar
<b>MRE01013</b>	0	0	3	0	43	0	0	0	33	12	5	0	0	0	0	3	15	0	82	0
<b>P.012</b>	75	1	0	0	0	0	0	0	0	0	4	0	0	63	0	3	12	0	22	0
<b>07ch011</b>	0	0	7	0	0	0	0	2	3	0	48	0	5	0	0	5	70	0	25	0
<b>04MRE143</b>	0	0	2	28	2	0	0	2	0	0	63	1	0	0	0	0	70	0	0	30
<b>MRE01004</b>	0	0	0	6	3	0	0	0	1	1	3	21	59	0	0	0	0	75	25	0
<b>04MRE256A</b>	0	0	0	0	0	60	0	0	13	4	0	0	0	0	0	95	0	0	5	0

Table 3.4: Examples of the selected three most dominant minerals, important minerals and SWIR-LWIR significant minerals in the rock samples. The bold black text in column 4 indicates the most abundant and significant mineral in the rock. The “+” sign indicates the minerals are significant and dominant in the zone. The “,” after “+” signs represent the presence of minerals in the zone.

Sample Code	Dominant mineral assemblages		SWIR-LWIR significance mineral assemblages	Lithology	Assigned alteration zone
	SWIR	LWIR			
MRE01013	Nacrite (43%), Jarosite (33%), PX-kaolinite(12%), HX-kaolinite(5%)	Quartz (82%), kaolinite (15%), jarosite (3%)	<b>Quartz</b> , Nacrite, Kaolinite, HX-kaolinite	Lazaras ash flow tuff	Silicic
P.012	Alunite (75%), HX-Kaolinite (4%)	Alunite (63%), Quartz (22%), Kaolinite (12%)	<b>Alunite+Quartz</b> , Kaolinite, HX-kaolinite	Alluvium	First advanced argillic
07ch011	HX-Kaolinite (24%), Montmorillonite (22%), PX-kaolinite (17%)	Kaolinite (70%), Quartz (25%), jarosite (5%)	<b>Kaolinite+Quart</b> , HX-kaolinite, Montmorillonite	Lazaras ash flow tuff	Second advanced argillic
04MRE143	HX-Kaolinite (63%), Pyrophyllite (28%),	Kaolinite (71%), K-feldspar (29%)	<b>Kaolinite</b> , HX-Kaolinite, K-feldspar, Pyrophyllite	Lazaras ash flow tuff	Intermediate argillic
MRE01004	Nontronite (59%), Montmorillonite (21%), Pyrophyllite (6%), HX-kaolinite (4%)	Nontronite (75%), Quartz (25%)	<b>Nontronite</b> , Quartz, Montmorillonite, Pyrophyllite, HX-kaolinite	Lazaras ash flow tuff	Argillic

04MRE256A	Chlorite (60%), Jarosite (13%), PX-Kaolinite (4%)	Jarosite (95%), Quartz (5%)	<b>Chlorite, Quartz</b>	Precaldera andesite	Propylitic
-----------	--	--------------------------------	-------------------------	------------------------	------------

### 3.2.6. Assigning rock samples into alteration zones

The rock samples are assigned into alteration zones such as (silicic, first advanced argillic, second, advanced argillic, intermediate argillic, argillic and propylitic). The naming of the alteration zone is according to Arribas et al. (1995) and (Hauff, 1983; Arribas, 1995; Hedenquist et al., 2000; Pirajno, 2009). The mineral assemblages are based on the combined result of SWIR-LWIR range significant mineral assemblages in the rock samples.

For example, the silicic zone is characterized by mainly dominant quartz mineral. Some alunite/kaolinite is also present. The silicic zone is formed due to the addition of silica into the rocks. However, the abundance of silica depends on the composition of the rock. In this study, rock samples associated with intermediate-felsic volcanic rocks (e.g., pyroxene andesite, hornblende andesite, Lazarus ash flow/cinto ash flow) are assigned to silicic alteration zone if they have quartz >70% plus the presence of alunite/kaolinite/pyrophyllite in the mineral assemblage. For rock samples associated with felsic rocks (e.g., rhyolite domes) are assigned to silicic alteration zone if they have quartz >80% plus the presence of alunite/kaolinite/pyrophyllite in the mineral assemblage. For rock samples associated with alluvium/colluvium are also assigned to silicic alteration zone if they have quartz >65% plus the presence of alunite/kaolinite/pyrophyllite.

The advanced argillic zone is divided into two zones. The first advanced argillic zone is dominated by alunite+quartz (>80%) where alunite is >60% and quartz >20%. The second advanced argillic zone is dominated by kaolinite + quartz (>80%) where kaolinite is >60%, and quartz is >20%

The intermediate argillic zone is dominated by kaolinite mineral. In this study kaolinite >70% and less quartz mineral <20% is assigned to the intermediate argillic zone. Kaolin group minerals between 50-60% but abundant than smectite group minerals in the mineral assemblages were also assigned to intermediate argillic zone.

The argillic zone is dominated by smectite minerals (montmorillonite/nontronite) and few kaolinite, k-feldspar minerals. Smectite minerals >50% were assigned to the argillic zone.

Propylitic zone mainly dominated by either calcite/chlorite or nontronite/jarosite. Without HX-kaolinite, pyrophyllite, dickite, nacrite because these minerals relate to high-temperature fluids. Therefore, calcite/chlorite/nontronite > 50% were assigned to propylitic zone.

Finally, based on the assigned rock samples into the alteration zones, two cross-section maps were produced. The profile lines were selected based on;

- 1) They cross all the alteration zones
- 2) Adequate sample distribution.

The assigned rock samples were also compared with the existing alteration maps.

## 4. RESULTS

This chapter introduces the results of all the steps including the SWIR and LWIR pre-processing, wavelength map, endmember extraction, mineral map and the combined result of SWIR-LWIR. A selection of rock samples were chosen as an illustration throughout this section.

### 4.1. Image pre-processing

Fifty-six images in SWIR and LWIR range were acquired (Appendix 1). The image files were converted to reflectance and emissivity data from the raw DN values. The results of the pre-processed image files after conversion to the reflectance and emissivity data are given below.

#### SWIR pre-processing

##### Fix SWIR 8<sup>th</sup> pixel problem and a spatial subset

The result shows before and after correction of the bad column in the data from the Specim SWIR3 camera (Figure 4.1A) and B) and the spatial subset of the SWIR image file (Figure 4.1C).

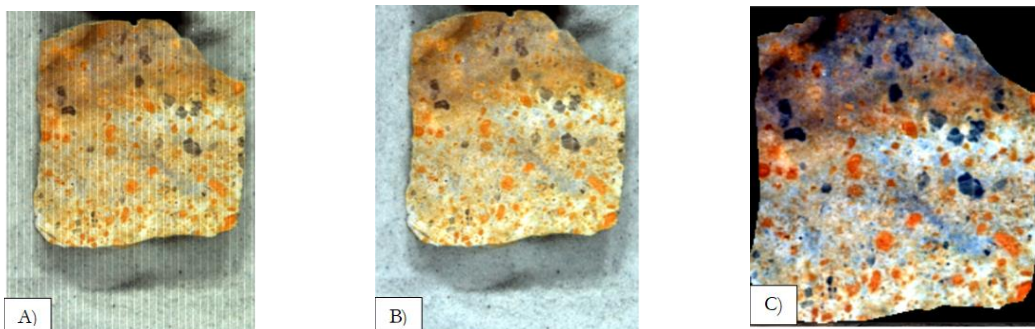


Figure 4.1: SWIR image file sample 05ch096 displayed in RGB 74, 158, 218. A) Before fixing the SWIR 8<sup>th</sup> sample and B) After fix the SWIR 8<sup>th</sup> sample and C) Spatial subset.

#### Spectral subset

Figure 4.2 A) shows a spectrum from sample 05ch096 before the spectral subsetting was performed. The spectral range goes from 894 nm – 2511 nm. Figure 4.2 B) shows the same spectrum from sample 05ch096 after the spectral subsetting was performed. The resultant bands cover 271 corresponding to the 985 nm to 2505 nm wavelength range.

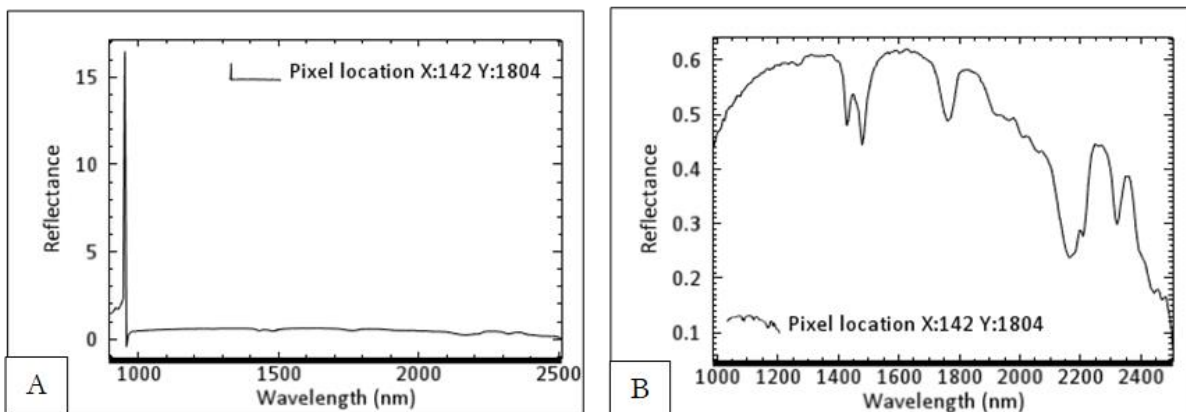


Figure 4.2: Spectra of the pixel (142, 1804) from sample 05ch096. A) before the spectral subset and B) after the spectral subset.

The result of the spectral subset of the image files was further pre-processed to remove outliers in the pixel and absorption effects that are not indicative of mineralogy using mean filter 1+5+1.

### Mean filter 1+5+1

The result of the mean filter shown in Figure 4.3 B). The spectrum shows reduced spikes compared with the one without the mean filter. Figure 4.3 A) shows a spectrum before the mean filter 1+5+1 was performed. Figure 4.3 B) shows a spectrum after the mean filter was applied for the same pixel location.

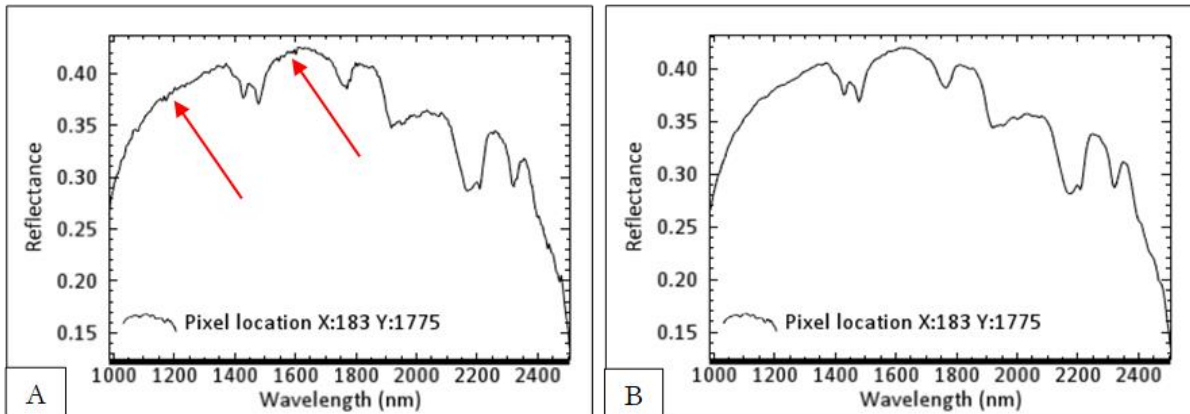


Figure 4.3: Spectra of the pixel (183, 1775) from sample 05ch096. A) before mean filter 1+5+1 and B) after mean filter 1+5+1. The red arrow shows the spikes before the filter.

### LWIR pre-processing

#### Spectral subset

Figure 4.4 A) shows a spectrum from sample 05ch096 before the spectral subsetting was applied. The spectral range goes from 7704.43 - 12571.90 nm. Figure 4.4 B) shows the same spectrum from sample 05ch096 after the spectral subset was performed. The result of the spectral subset covers 73 bands corresponding to the 7996.49 nm to 11501 nm wavelength range.

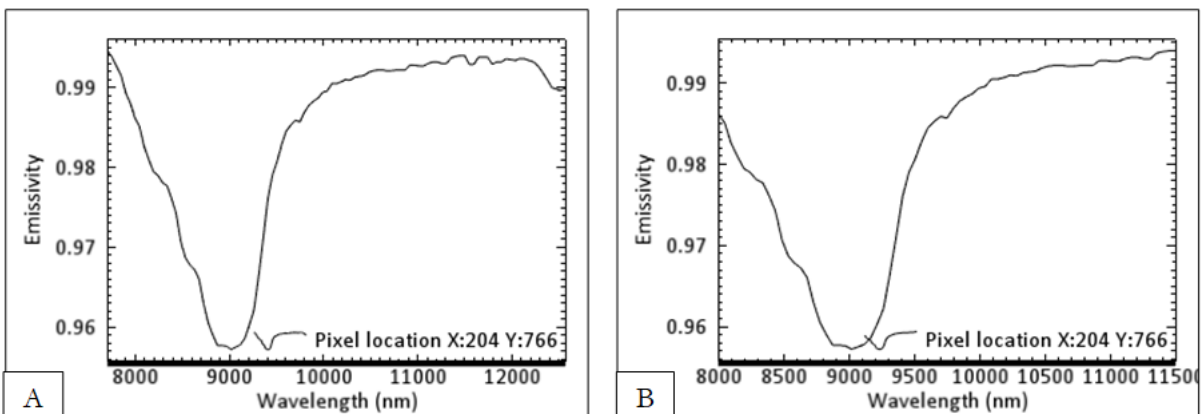


Figure 4.4: A) Spectra of the pixel (204, 766) from sample 05ch096. A) before the spectral subset and B) after the spectral subset.

### MNF

Forward and backward MNF transform was applied to suppress the noise with minimum spectral feature impact on the spectral subset LWIR image files. Figure 4.5 shows the forward MNF transform result from sample 05ch094. The first six components that contain most of the information (i.e., signal bearing) were selected. MNF component 7-73 are dominated by random noise that degrades the signal content of the image. They are excluded from the backward MNF transformation by a spectral subsetting to the first 6 MNF components.

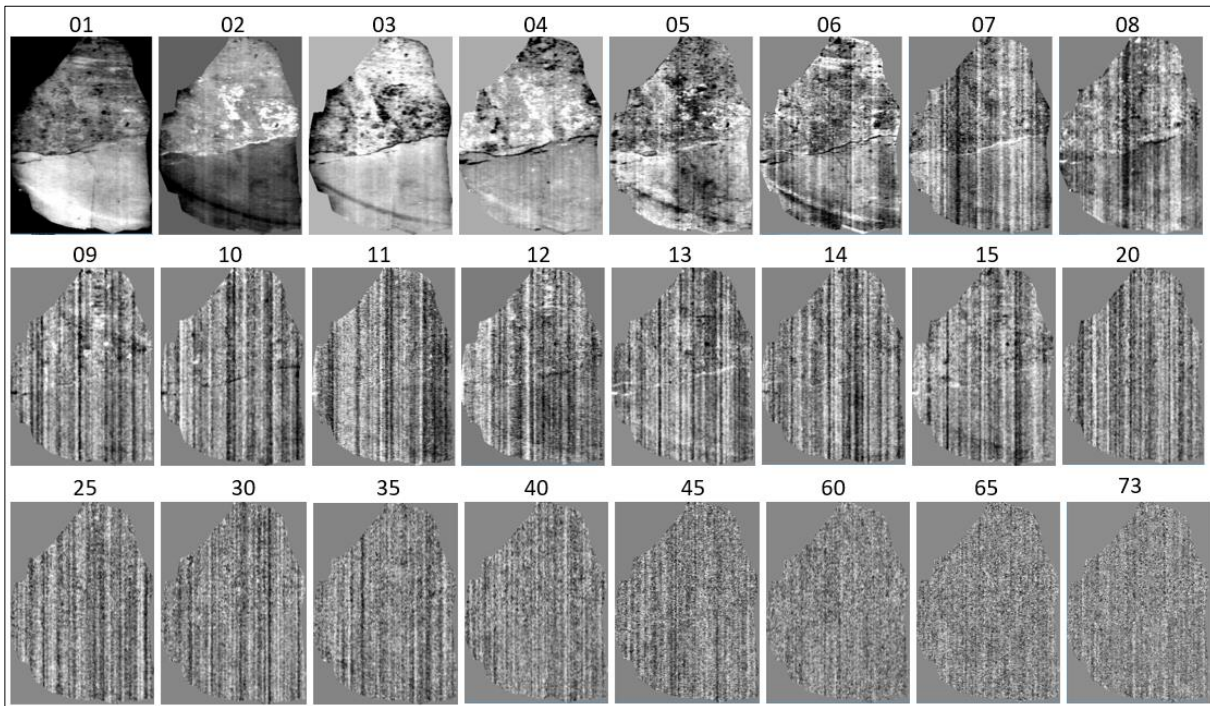


Figure 4.5: Forward MNF transform components sorted by decreasing signal to noise ratio (sample 05ch094)

The result of the forward and backward MNF transform is shown in (Figure 4.6 B). The spectrum shows reduced spikes compared with the one without the forward and backward MNF transform. Figure 4.6 A) shows a spectrum before the forward and backward MNF was performed. Figure 4.6 B) shows a spectrum after the forward and backward MNF transform was applied for the same pixel location.

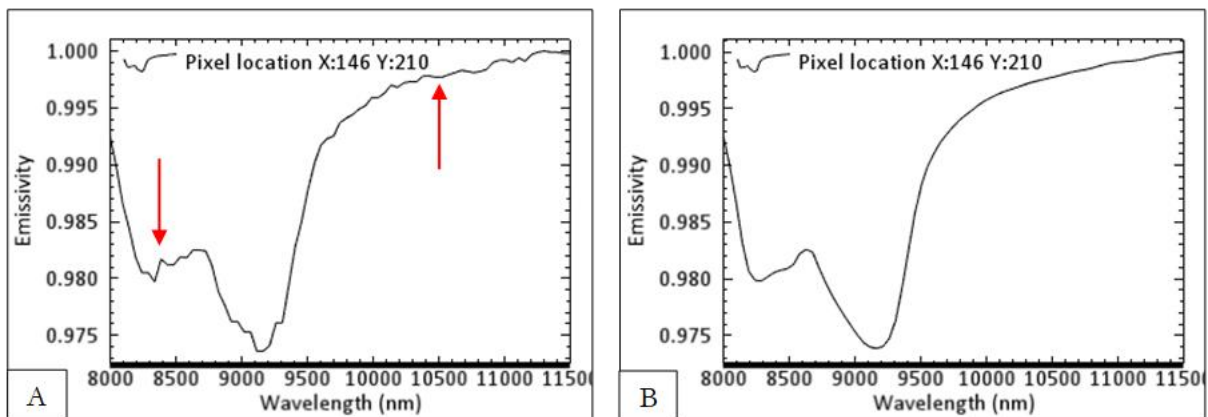


Figure 4.6: Spectra of the pixel (146, 210) from sample 05ch094. A) before forward and backward MNF transform and B) after forward and backward MNF transform. The red arrow shows the spikes before forward and backward MNF transform.

## 4.2. Wavelength map

The results of the wavelength maps of fifty-six images of SWIR and LWIR wavelength range were produced at a wavelength range between 2100-2400 nm and 800-11500 nm respectively. These results are spatially presented based on the geographic location of the samples (Appendix 2 and 3). The spatial distribution of these wavelength maps of the rocks shows patterns of alteration zones, for example, the propylitic alteration zone was outlined at the periphery of the Rodalquilar epithermal system and the silicic/advanced argillic zones at the center of the area.

The result of the wavelength maps in the SWIR range highlighted the presence of alunite, jarosite, kaolinite, pyrophyllite, nacrite, halloysite, dickite, montmorillonite, nontronite, chlorite in the wavelength range between 2100-2400nm. The wavelength map results in LWIR highlight the presence of quartz, k-feldspar, hornblende, pyroxene, anorthite, alunite, jarosite, kaolinite, nontronite, calcite and dolomite in the wavelength range between 8000-11500 nm.

As an illustration, the wavelength map of the sample 05ch094 can be seen in Figure 4.7. The yellow colour at wavelength 2267 nm shows pixels with jarosite (spectrum in Figure 4.8 A). Cyan colours at the wavelength around 2170 show pixels with alunite (spectrum in Figure 4.8 A) and the black colour in the 2100-2400 nm which is highlighted by red colour at around 9200 nm in Figure 4.7 B) is quartz (spectrum in Figure 4.8 B). The cyan at wavelength 8969 is alunite (spectrum in Figure 4.8 B). The greenish colour at a wavelength around 9018 nm is also jarosite (spectrum in Figure 4.8 B). The other colours in the LWIR range are mixtures of quartz and alunite.

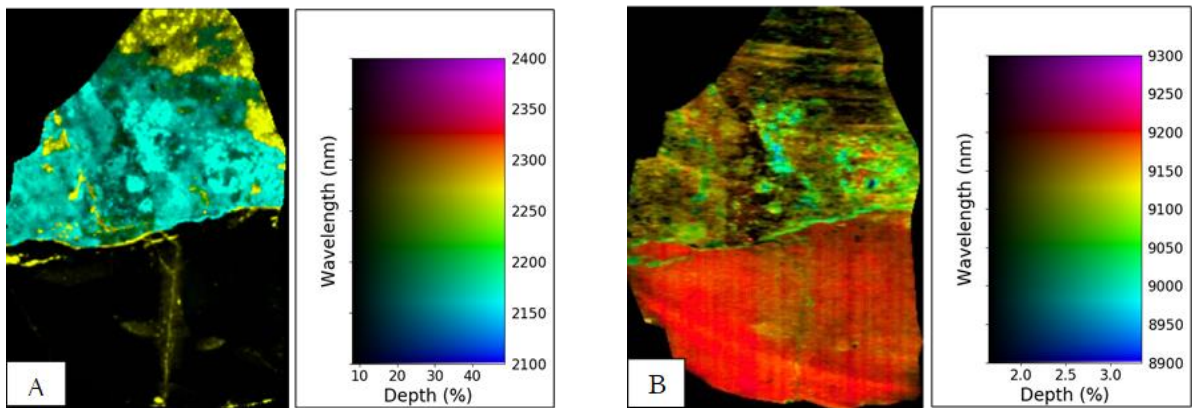


Figure 4.7: Wavelength map sample 05ch094 A) SWIR image for the wavelength range between 2100-2400nm and B) LWIR image for the wavelength range between 8900-9300nm.

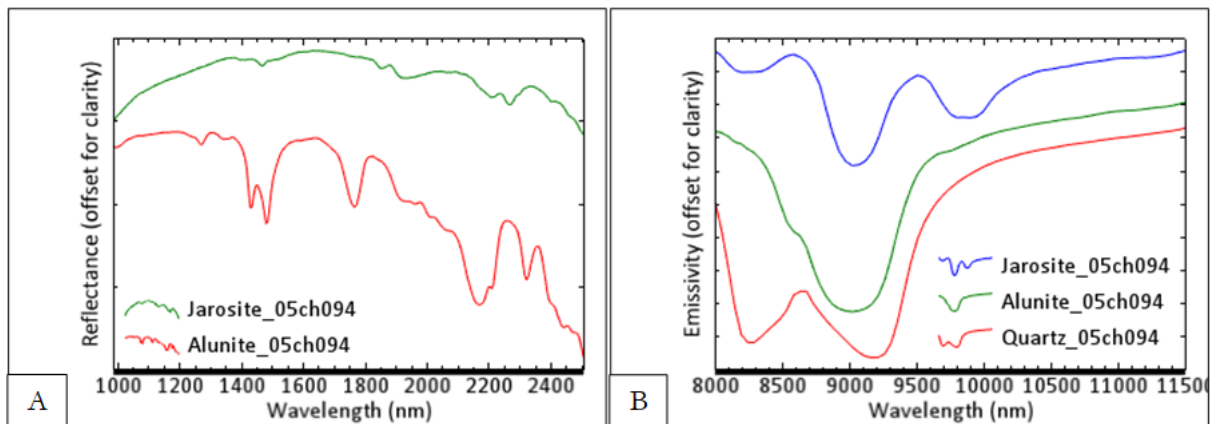


Figure 4.8: Spectra from sample 05ch094 showing the profile of A) Jarosite and alunite B) Jarosite, alunite, and quartz.

Wavelength maps covering different wavelength ranges were produced. As an illustration, the wavelength map of the sample 07ch003 is presented in Figure 4.9. In 2100-2400 nm wavelength range the yellow colour pixels represent only jarosite mineral (spectrum in Figure 4.10 A). The rest green pixels at wavelength 2100-2400 nm shows nacrite dickite, alunite minerals together. Then in the wavelength map of the range 2200-2210 nm (Figure 4.9 B) the greenish yellow pixels show dickite minerals (spectrum in Figure 4.10 A), the

greenish colour highlight nacrite mineral (spectrum in Figure 4.10 A) and the few cyan pixels show alunite minerals (spectrum in Figure 4.10 A).

In the LWIR wavelength range of the same sample 07ch003 (Figure 4.9 C and D), the wavelength map in the range 8000-11500 nm the image is highlighted by only green colour of the quartz mineral (spectrum in Figure 4.10 B). The result was further spectrally subset to 8800-9300 nm (Figure 4.9 D) to see differences in the quartz mineral. Then the result highlight reddish colour at a wavelength around 9200 nm, yellowish colour at a wavelength around 9100 nm and few greenish pixels at a wavelength around 9050 nm. They all represent quartz (spectrum in Figure 4.10 B) with a little shift in the deepest absorption feature. The shift of the different quartz minerals could be due to a mixture with alunite or jarosite. For instance, the shift of the emissivity minima around 9100 nm is associated with jarosite. The shift around 9050 nm is associated with alunite. This indicates that the SWIR range is sensitive for detecting jarosite, alunite, dickite, and nacrite while the LWIR range is sensitive for detecting quartz. However, indirectly it is also possible to know the presence of alunite and jarosite minerals using a shift of quartz features.

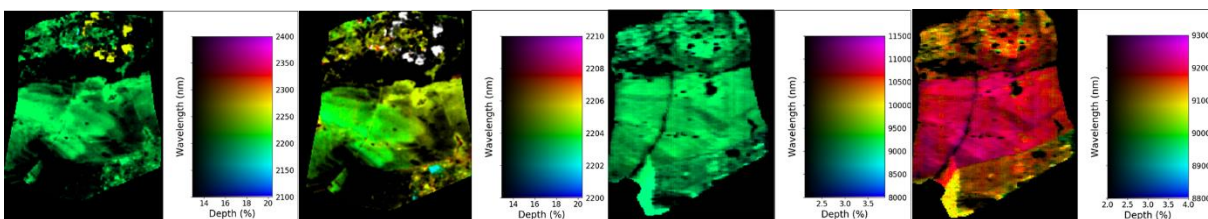


Figure 4.9: Wavelength map of sample 07ch003 A) wavelength range between 2100-2400 nm, B) wavelength range between 2200-2210 nm, C) wavelength range between 8000-11500 nm and D) wavelength range between 8800-9300 nm

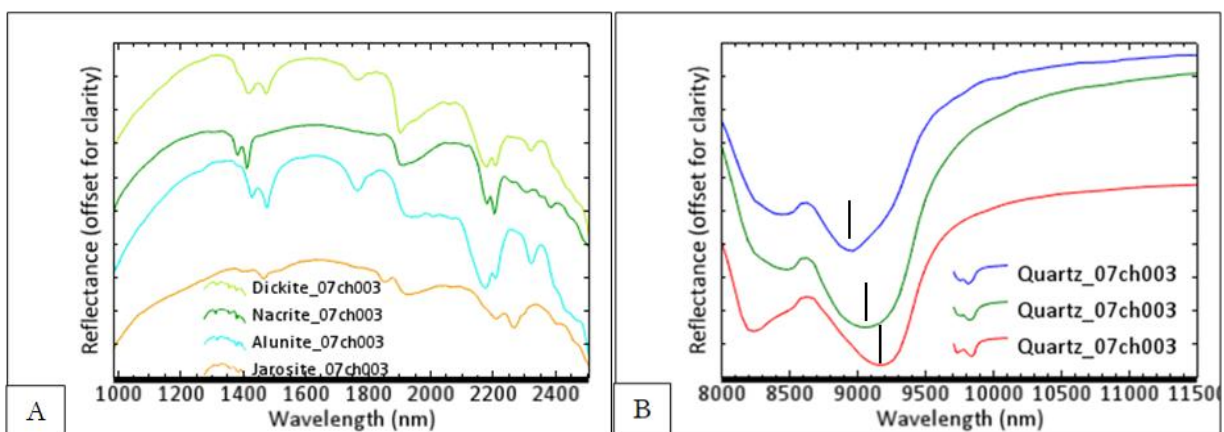


Figure 4.10: Spectra from sample 07ch003 showing the profile of A) dickite, nacrite, alunite, jarosite. B) spectrum of quartz minerals shows a shift in the deepest emissivity minima. The vertical black lines represent a shift in the deepest emissivity minima of quartz.

### 4.3. Endmembers

In the SWIR wavelength range, the following endmembers of altered minerals including alunite, jarosite, pyrophyllite, highly crystalline kaolinite, nacrite, dickite, hydrated halloysite, nontronite, montmorillonite, chlorite, poorly crystalline kaolinite, alunite+water, and dehydrated halloysite were extracted. The endmembers spectra are shown in Figure 4.11.

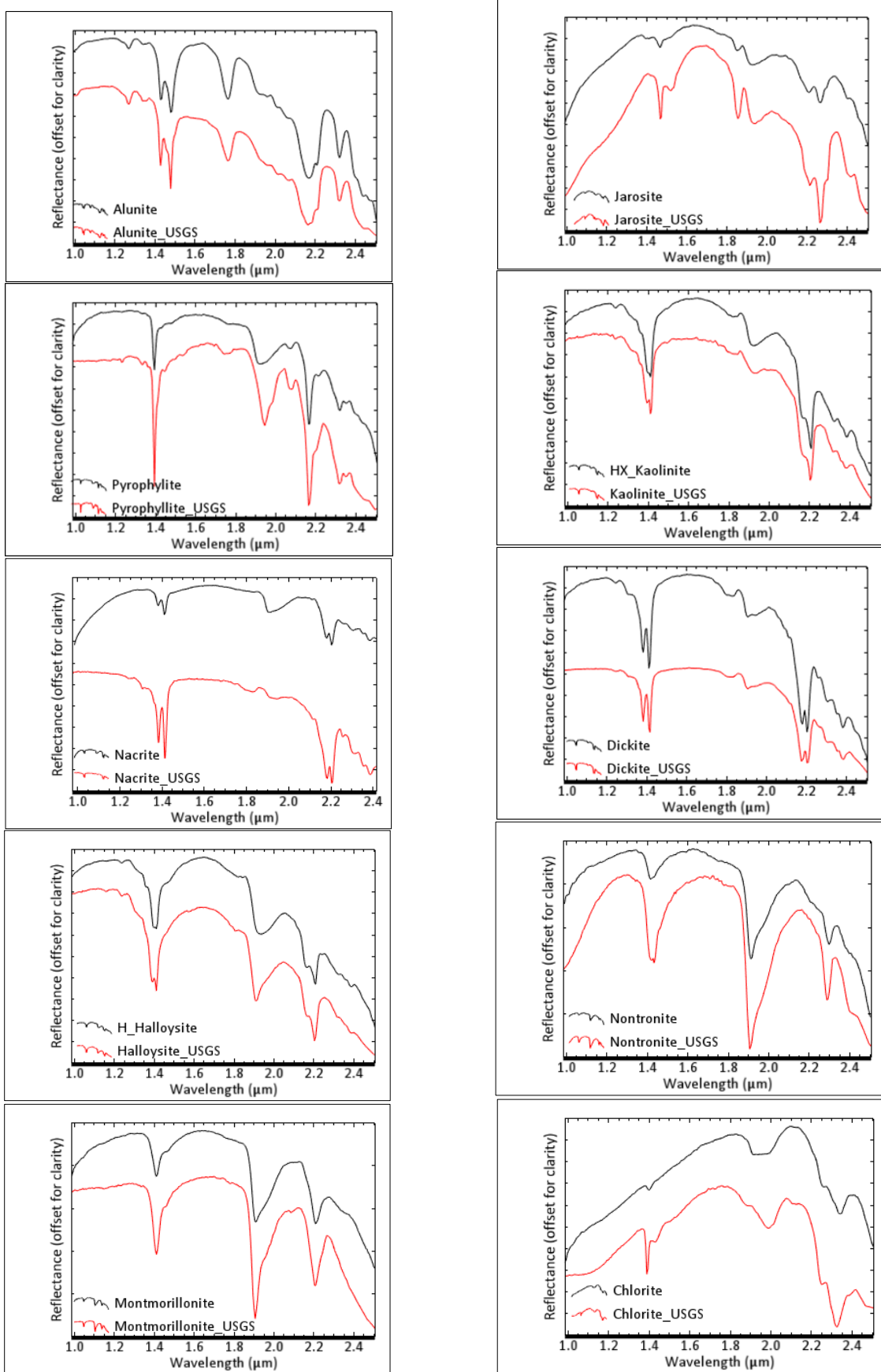


Figure 4.11: Spectra of selected pure endmembers from SWIR wavelength range versus USGS spectral library.

Two alunite endmembers were selected. The two endmembers differ in the water absorption feature around 1900-2062 nm, and in the slope of the spectra between the wavelength 1910 to 2050 nm (Figure 4.12 A). For the kaolinite endmembers, two types of kaolinite were selected based on the crystallinity of spectral feature (Figure 4.12 B). They are highly crystalline kaolinite (HX-kaolinite) and poorly crystalline kaolinite (PX-kaolinite). HX-kaolinite has a low water absorption depth at wavelength 1900 nm and a small feature at wavelength 1823 nm (Figure 4.12 B). The PX-kaolinite has a higher water absorption depth at wavelength 1900 nm (Figure 4.12 B). Hydrated (H-Halloysite) and dehydrated halloysite (D-Halloysite) are selected based on differences in the water absorption feature at 1900 nm. Dehydrated halloysite show sharp, narrow and shallow depth absorption feature at 1900 nm (Figure 4.12 C).

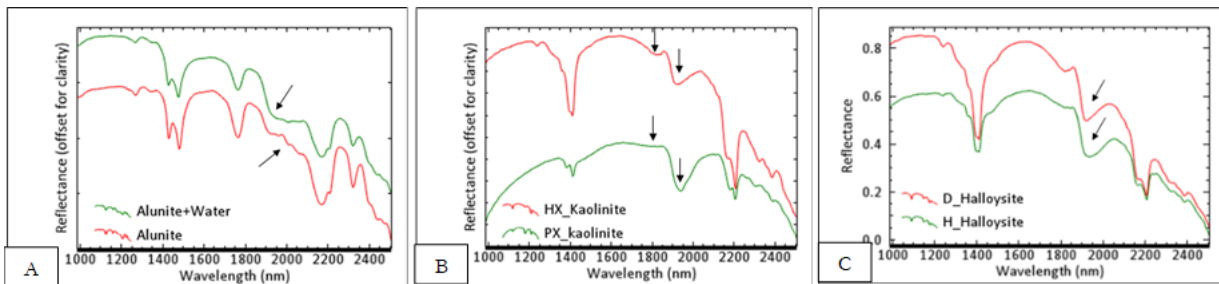
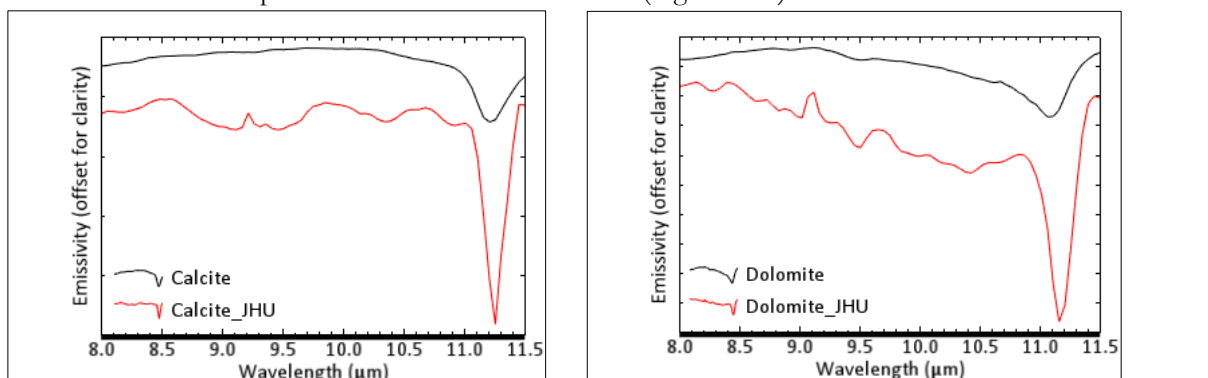


Figure 4.12: Endmember spectra A) HX\_kaolinite and PX\_kaolinite B) Alunite and Alunite+water C) D-Halloysite and H-Halloysite.

In the LWIR wavelength range, the following endmembers including unaltered minerals (quartz, hornblende, anorthite, pyroxene, K-feldspar, calcite, and dolomite) and altered (alunite, jarosite, nontronite, kaolinite, and halloysite) were extracted. The endmembers spectra are shown in Figure 4.13. Carbonate minerals such as **calcite** and **dolomite** have a single emissivity minimum feature at 11209 nm and 11111 nm respectively, but the calcite and dolomite minerals in JHU spectral library have an emissivity minimum feature at 11269 nm and 11148 nm respectively. **Alunite** has a deep emissivity minimum feature at 8969 nm, is much broader than jarosite and has two shallower emissivity minimum features at 8568 nm on the shoulder of the spectra and 9726 nm. **Jarosite** has a narrow emissivity minimum feature compared to Alunite at 9018 and two shallower emissivity minimum features at 8239 nm and 9846 nm. **Kaolinite** has four emissivity minimum features with the primary feature at 9554 nm, secondary feature at 8872 nm, third feature at 9943 nm and fourth feature at 11014 nm. **Nontronite** has a significant emissivity minimum feature at 9602 nm and is asymmetric with a shoulder at 8921 nm. **Hornblende** has a primary emissivity minimum feature at 10138 nm. **Halloysite** has a primary emissivity minimum feature at 9505 nm, compared to kaolinite it has a less significant feature at 8872 nm and compared to nontronite it has a narrow feature and is asymmetric the right shoulder. **K-feldspar** has three emissivity minimum feature at 8434 nm, 8602 nm, and 9943 nm. **Anorthite** has a primary emissivity minimum feature at 10770 nm. **Pyroxene** has a first emissivity minimum at 9554 nm, second feature at 10284 nm and third feature at 11306 nm. Two types of quartz are selected, **Quartz-1** has a doublet emissivity minimum feature centered at 8629 nm with the minimum at 8483 nm and 9067 nm. **Quartz-2** also show a doublet emissivity minimum feature, but the minimum features are present at 8215 nm and 9213 nm (Figure 4.13).



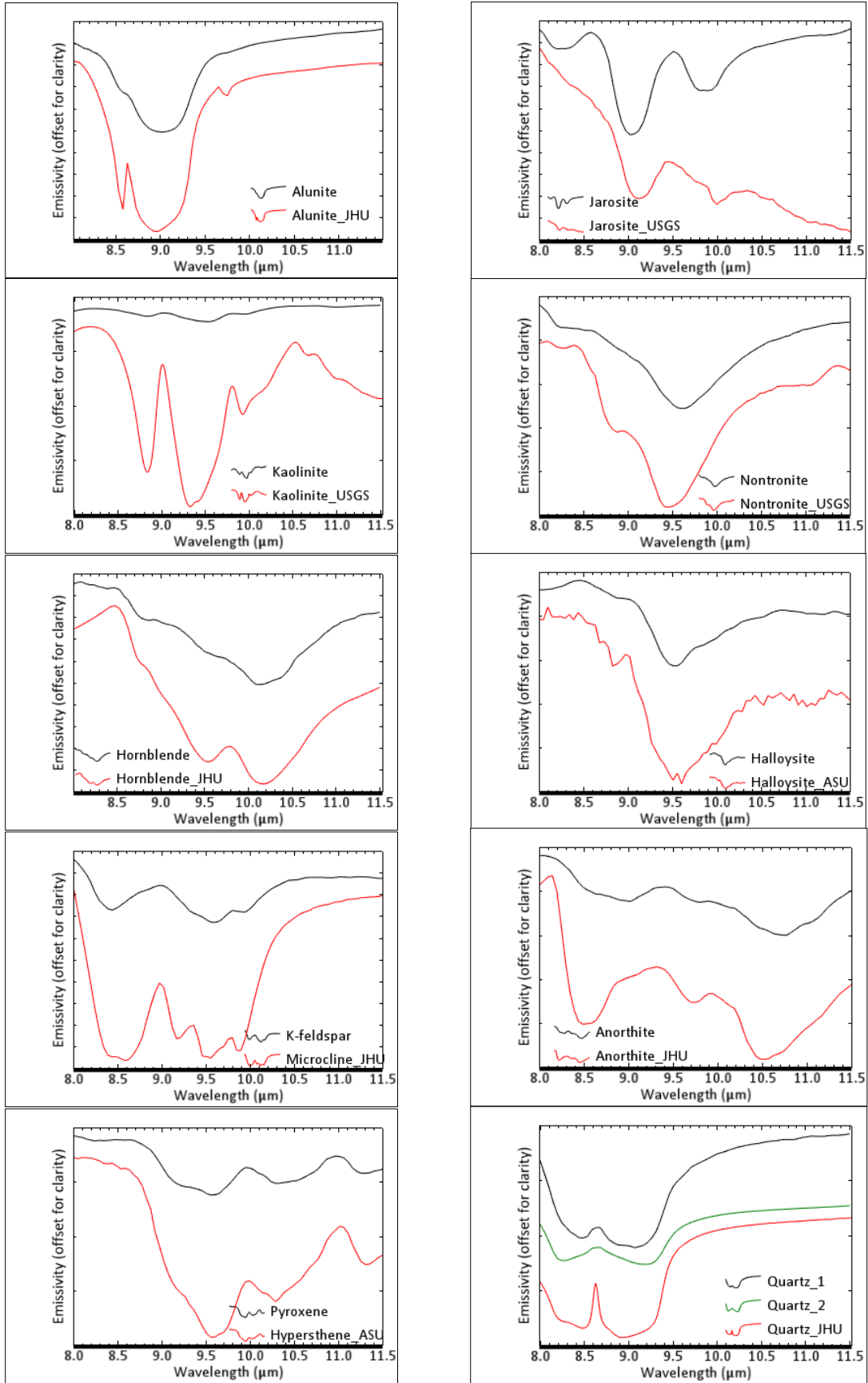


Figure 4.13: Spectra of selected endmembers from LWIR wavelength range and comparison with spectral libraries (USGS, JHU, and ASU).

#### 4.4. Mineral map

Mineral maps of the most dominant minerals per pixel for the SWIR and LWIR wavelength range of the 56 rock samples were produced. The results show that in the LWIR range all the pixel in the images are classified into the endmember minerals while in SWIR range for three samples (04MRE040, 04MRE048(2) and 06cb163) more than 50% of the image pixels are unclassified (represented by black). The abundance of the minerals in the samples are described in Appendix 4 and 5. The specific mineral identification of the secondary minerals in the LWIR range were verified using the SWIR range active minerals and hand specimen observations in the same pixel location and vice versa. As an illustration, a few samples are described in this section.

The SWIR range allows the mapping of Alunite, alunite+water, dickite, pyrophyllite, nacrite, chlorite, D-halloysite, H-halloysite, jarosite, PX-kaolinite, HX-kaolinite, montmorillonite and nontronite minerals in the rock samples of the study area (Appendix 4). Minerals mapped in LWIR range include alunite, halloysite, jarosite, kaolinite, nontronite, quartz-1, quartz-2, k-feldspar, pyroxene, anorthite, calcite, and dolomite in the rock samples.

The classified mineral maps derived from SWIR and LWIR hyperspectral data were compared regarding the minerals and their distribution in the rock samples to see the similarities and differences in the mapping of the minerals. These similarities and differences are shown in Figure 4.14 for two examples of the silicified rock sample 07ch014 and the rock sample 05ch094 and in Figure 4.15 for two examples of the advanced argillic rock sample P.012 and the rock sample 07ch009. These samples are selected since the study is about the characterization of the rock samples of the high sulfidation epithermal system, and these zones are the most critical zones in the high sulfidation epithermal system.

Figure 4.14 A) & B) shows the result of the rock sample 07ch014 in the SWIR range from abundant to less abundant minerals, the rock consists of nontronite, jarosite, PX-kaolinite, montmorillonite, alunite, alunite+water, pyrophyllite, HX-Kaolinite, and nacrite. In the LWIR range, the same rock sample 07ch014 consists of quartz, alunite, and kaolinite in decreasing abundance. In both SWIR and LWIR range alunite is mapped but there is a significant difference in the distribution, and among the kaolin group minerals only kaolinite is mapped. In the LWIR range nontronite, montmorillonite, pyrophyllite, and nacrites are not mapped. In the SWIR range quartz is not mapped and the unclassified (black colour) is mapped by alunite in LWIR range. Therefore the combined SWIR and LWIR range is advantageous over the independent analysis, for the mapping of minerals associated with silicic alteration zones in high sulfidation epithermal system.

Figure 4.14 C) & D) shows that the SWIR mineral map from the silicified rock sample 05ch094 allows mapping the distribution of alunite and jarosite while in the LWIR range allows mapping of quartz, alunite, and jarosite in decreasing abundance.

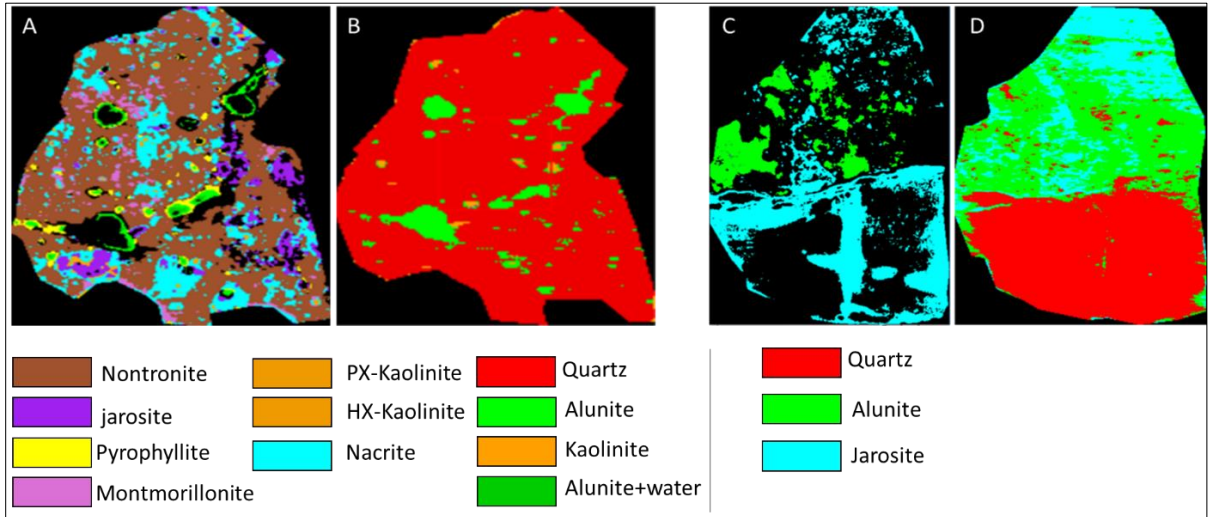


Figure 4.14: Mineral map from sample A) 07ch014 SWIR range, B) 07ch014 LWIR range, C) SWIR range 05ch094 and D) 05ch094 LWIR range

In general, jarosite and alunite minerals can be mapped by both the SWIR and LWIR ranges. However, quartz is only mapped in the LWIR range. For the SWIR sample 05ch094 the fine-grained quartz, all the unclassified pixels are mapped by quartz in LWIR while the unclassified associated with vugs are mapped by quartz and alunites in LWIR.

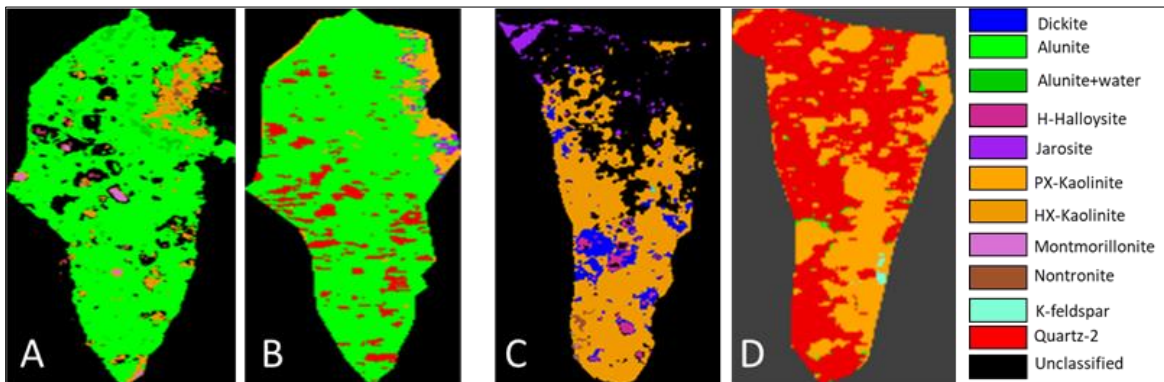


Figure 4.15: Mineral map sample P.012 A) SWIR range B) LWIR range, and mineral map sample 07ch009 C) SWIR range D) LWIR range

Three samples 04MRE042, 04MRE042(1) and 04MRE042(2) were selected from the same rock unit out of curiosity. Since, in the hand specimen the rocks showed differences in colour. After analysis, the results showed that sample 04MRE042 was composed of nontronite, HX-kaolinite and nacrite. Sample 04MRE042(1) was made up of nontronite, pyrophyllite, quartz and Nacrite. Sample 04MRE042(2) composed of nontronite, quartz and nacrite. The minerals identified in these samples indicated that the rocks had differences in the kaolin group minerals and pyrophyllite. This difference could be due to the presence of stringers/veinlets intruded the rock samples.

### Texture

Study of textures of the rock samples can help to understand the origin of the alteration minerals. In this study, hydrothermal alteration minerals are observed in veinlets, vugs and as a replacement of primary minerals (phenocrysts). As an illustration the samples 05ch099, MRE01011, and 05ch094 are described.

Alunite veins are common in most of the rock samples, and often cut across the rock samples and cross-cutting each other (Figure 4.16). This cross-cutting relationship suggests at least two episodes of alunite veining in the area. Both the two generations of alunite veins are also cutting kaolinite minerals (Figure 4.16). This cross-cutting relationship also indicates that kaolinite mineral is formed first then intruded by alunite veins.

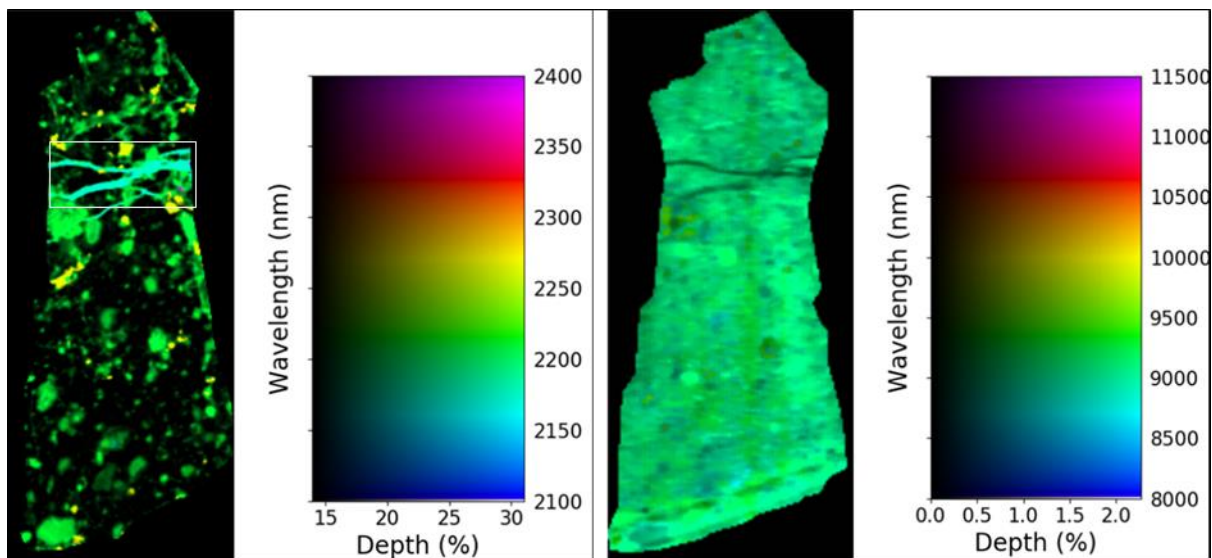


Figure 4.16: Crosscutting two generations of alunite veins in sample 05ch099 highlighted by cyan colour in the SWIR range. The white inset rectangle indicates the cross-cutting relationship between the two alunite veins.

A linear feature of oxidized sulfide veins cut across the rock sample is also observed in sample MRE01011 (Figure 4.17). This vein in the SWIR range is highlighted by linear feature black colour and green colour in the LWIR range. The wavelength map in LWIR highlight as quartz mineral. It is also visible in hand specimen shows oxidized sulfide mineral (Figure 4.17 A). Among the sulfide minerals the most probable is pyrite because it shows a euhedral shape in the hand specimen. This oxidized sulfide vein may be related to the vicinity of the ore deposit/mineralized zone.

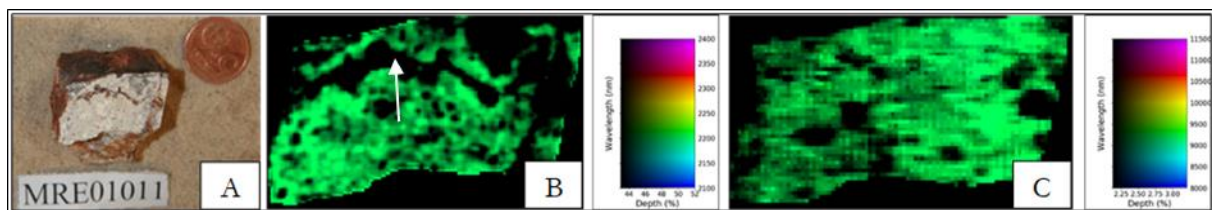


Figure 4.17: Veinlet composed of oxidized sulfide minerals from the hand specimen observation A) and highlighted by a black linear feature in SWIR range B) and highlighted by green colour quartz mineral in LWIR range C) (sample MRE01011). The white arrow shows the oxidized sulfide veinlet.

Overprinting of vuggy silica and chalcedony are observed in the sample 05ch094. Also a jarosite veinlet is filled along the contact between the vuggy silica and chalcedony (Figure 4.18) which indicates oxidation of alunite veinlet minerals because alunite is aluminium potassium sulfate mineral, where iron replaces aluminium. This suggested alunite occurs as veinlet and replacement in the rock sample.

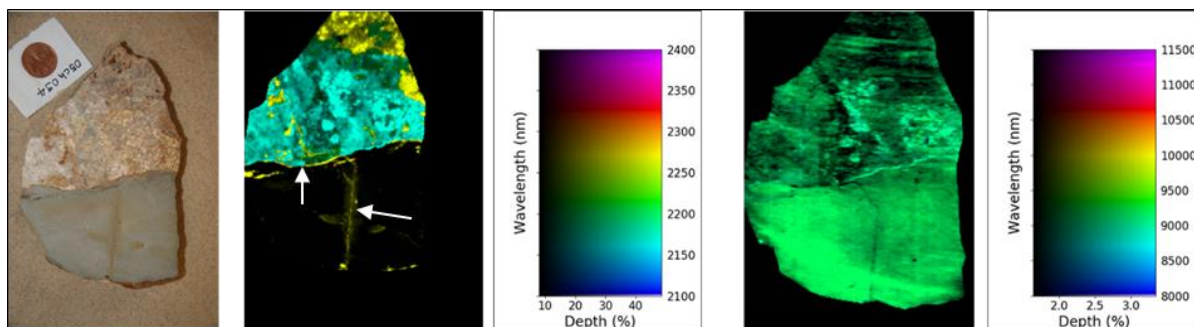


Figure 4.18: Overprinting of vuggy silica and chalcedony (sample 05ch094). The white arrows indicate jarosite filled the contact between chalcedony and vuggy silica, and within the chalcedony.

#### 4.5. SWIR-LWIR combined result

The SWIR-LWIR combined result is presented in a tabular form (Table 4.1) for the full dataset see (Appendix 6). The SWIR and LWIR range mineral map results were combined to get the significant mineral assemblages of the rock samples and then to classify the rock samples into the alteration zones. The result shows the presence of the most significant mineral assemblages such as quartz dominated (>70%, e.g. sample MRE01013), alunite+quartz (>80% e.g. sample P.012), kaolinite+quartz (>80% e.g. sample 07ch011), kaolinite (>70% e.g. sample 04MRE143), smectite minerals (>50% and presence of crystalline kaolin group minerals e.g. sample MRE01004), chlorite/calcite/nontronite (e.g. sample 04MRE256A).

Table 4.1: The SWIR-LWIR combined result. The bold black text in column 4 indicates the most significant mineral in the rock.

Sample code	SAM-Mineral abundance (%)		SWIR-LWIR significant mineral assemblage
	SWIR	LWIR	
<b>MRE01013</b>	Nacrite (43%), Jarosite (33%), PX-kaolinite(12%), HX-kaolinite(5%)	Quartz (82%), kaolinite (15%), jarosite (3%)	<b>Quartz</b> , Nacrite, Kaolinite, HX-kaolinite
<b>P.012</b>	Alunite (75%), HX-Kaolinite (4%)	Alunite (63%), Quartz (22%), Kaolinite (12%)	<b>Alunite+Quartz</b> , HX-kaolinite, Kaolinite
<b>07ch011</b>	HX-Kaolinite (24%), Montmorillonite (22%), PX-kaolinite (17%)	Kaolinite (70%), Quartz (25%), jarosite (5%)	<b>Kaolinite (HX-Kaolinite)+Quartz</b> , Montmorillonite
<b>04MRE143</b>	HX-Kaolinite (63%), Pyrophyllite (28%),	Kaolinite (71%), K-feldspar (29%)	<b>Kaolinite</b> , HX-Kaolinite, Pyrophyllite
<b>MRE01004</b>	Nontronite (59%), Montmorillonite (21%), Pyrophyllite (6%), HX-kaolinite (4%)	Nontronite (75%), Quartz (25%)	<b>Nontronite</b> , Montmorillonite, Quartz, Pyrophyllite, HX-kaolinite
<b>04MRE256A</b>	Chlorite (60%), Jarosite (13%), PX-Kaolinite (4%)	Jarosite (95%), Quartz (5%)	<b>Chlorite</b> , Quartz

#### 4.6. Assign rock samples into alteration zones

The rock samples were assigned into alteration zones based on the combined SWIR-LWIR wavelength range results. As an illustration (Figure 4.19 B & C) is presented in this section, which shows the assigned

rock samples and cross-section of the alteration zones in the Rodalquilar high sulphidation epithermal system. The full set of the rock samples is presented in Appendix 6. The result shows the rock samples are classified into silicic, first advanced argillic, second advanced argillic, intermediate argillic, argillic and propylitic alteration zones. Most of the rocks are classified into the intermediate argillic zone (23 rock samples), followed by argillic (14 rock samples), silicic alteration zone (9 rock samples), propylitic (7 rock samples), second advanced argillic (2 rock samples) and first advanced argillic (1 rock sample).

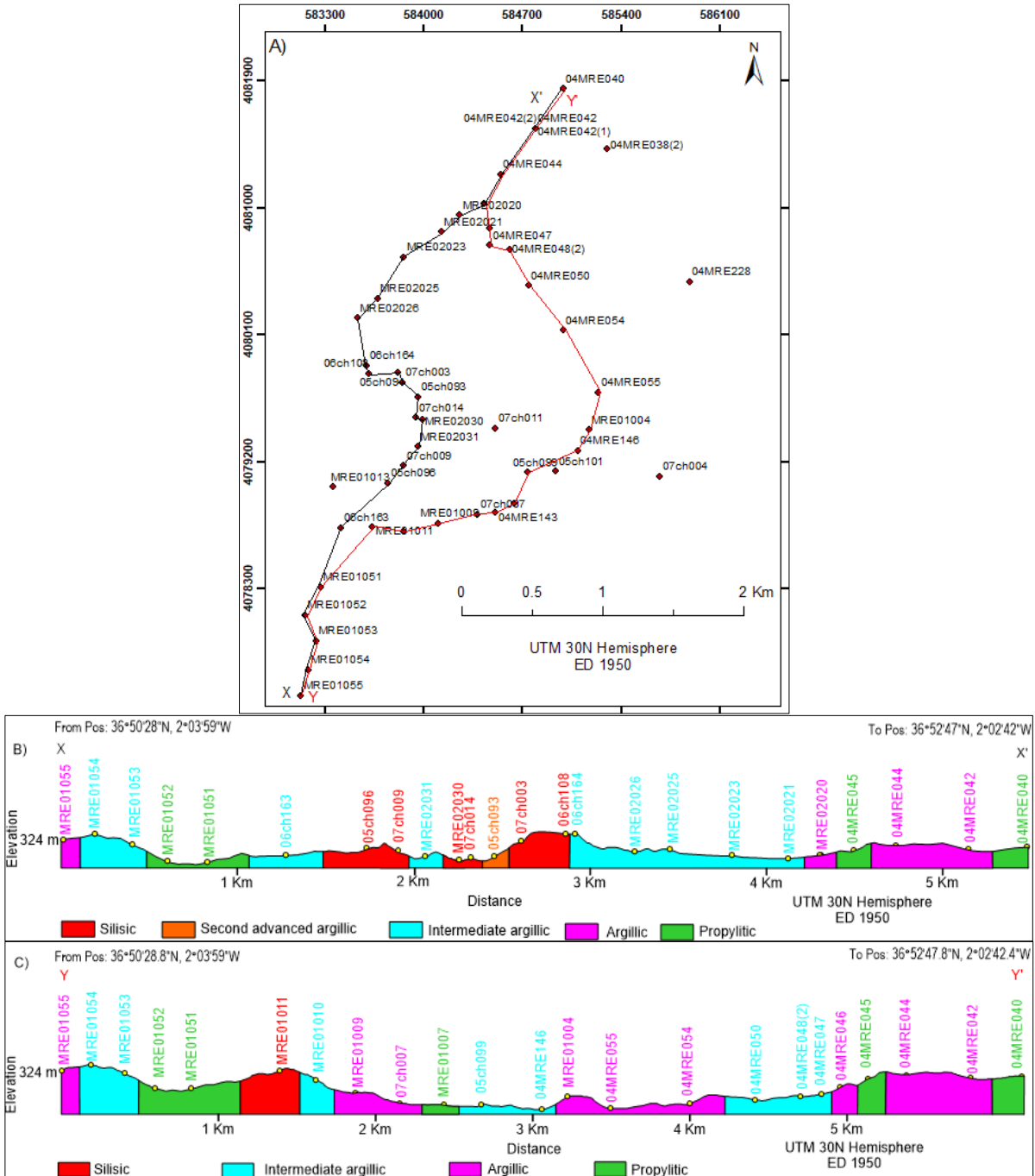


Figure 4.19: Rock samples and alteration zones. A) shows rock sample locations, profile lines X-X' and profile line Y-Y,' B) Cross-section of the alteration zones along the profile line X-X,' C) cross-section of the alteration zones along the profile line Y-Y.' The sample number label with different colour represents the type of the alteration zone similar to the legend.

## 5. DISCUSSION

In this research SWIR and LWIR range image data of surface rock samples were used to characterize alteration minerals associated with high sulfidation epithermal system. This chapter discusses selected data and methods, and the results. The discussion is as follows.

### 5.1. Selected data and methods

Emissivity data was used for the LWIR wavelength range, because in LWIR range alunite, quartz, nontronite, halloysite, and k-feldspar minerals have low reflectance value and broad absorption feature between 9500 nm - 11500 nm wavelength range which makes it difficult to discriminate the minerals using reflectance data in wavelength mapping. However, using emissivity data in wavelength mapping highlights the diagnostic minimum emissivity value of the minerals present in the image. Since, in emissivity data 9500 nm-11500 nm wavelength range has a highest emissivity value.

For the LWIR range data, wavelength mapping in 8000-11500 nm wavelength interval makes impossible to differentiate quartz from the clay minerals. Since, quartz and clay minerals were highlighted by similar colour in that range. The reason could be due to the overlapping of the first minimum emissivity feature. Since quartz spectra have the highest depth value compared to clay minerals, the RGB colour composite of the first interpolated depth, the first interpolated minimum wavelength, and the second interpolated minimum wavelength was created. This combination has proved successful in discriminating quartz from clay minerals. Accordingly, this approach is recommended for future application.

For the mineral mapping and quantification of the minerals in the rock sample, a classification method using SAM was selected. The reasons are explained in detail in section 3.2.4. However, the quality of the mineral mapping is strongly dependent on the threshold, the quality of the endmember collected and the spectral profile of the wavelength range (Hecker et al., 2008). In this research different threshold values were tested to get a quality mineral map and the result was verified by checking the spectra and mineral pattern and compared with the hand specimen. For example, sample 05ch094 from the hand specimen and wavelength mapping typically shows overprinting of vuggy silica (associated with alunite and jarosite) and chalcedony (cryptocrystalline quartz) in Figure 4.7 and Figure 4.14 A mineral map of the same sample 05ch094 (Figure 4.18) with a threshold value 0.1 radians for SWIR image files and 0.05 radians for LWIR image files give a reasonable similarity with the wavelength mapping result and texture in the rock samples. Therefore, this threshold value using SAM method for high sulfidation rock samples is recommended for future application.

For the LWIR image files, the result shows hornblende mineral is unclassified in all of the rock samples. However, in the hand specimen coarse-grained hornblende were observed in samples 04MRE040, 04MRE044, 04MRE256A and MRE02020. The set of endmembers used for the classification affects the mapping of the hornblende mineral in the rock samples. For example, using only endmembers from the rock sample itself will classify the hornblende mineral, but using the full set of endmembers used from the rock samples of the entire area, hornblende remains unclassified. The reason can be due to the similarity of the spectral signature of hornblende with other minerals such as nontronite and halloysite because the SAM method depend on an overall spectral fit rather than the individual emissivity minima features. Therefore, SAM classification method using full spectral range of endmembers consist of hornblende, halloysite and nontronite mineral may provide a wrong classification.

## 5.2. Discussion on the results

### 5.2.1. Mineral assemblages in the rock samples

Minerals such as nacrite, dickite, pyrophyllites, montmorillonite, and chlorite can only be identified in the SWIR range and not in the LWIR range. Quartz, k-feldspar, pyroxene, hornblende, anorthite, calcite, and dolomite can only be identified in the LWIR range and not in the SWIR range. Minerals such as kaolinite, halloysite, nontronite, alunite, and jarosite similarly can be mapped in both the SWIR and the LWIR range. However, for the barite, and zunyite the SWIR and LWIR data analysis both show that it's difficult to identify the minerals in the rock samples, the reasons could be 1) due to the absence of these minerals in the rock samples selected. Since, the samples of this study were selected only from the altered and unaltered area not from the core of the mineralization. For example, barite in hydrothermal system occur as veins and is a gangue mineral associated with sulphide ore veins. 2) due to the limited stability of minerals for example, zunyite is stable up to 450°C and is replaced by topaz at higher temperatures (Hsu, 1986). In the Rodalquilar area presence of the topaz minerals were also reported by Arribas et al. (1995). Therefore, the SWIR and LWIR range indicates that altered and unaltered minerals of high sulfidation epithermal deposit are present in the Rodalquilar area. Also, mineral mapping using the LWIR range provides complementary information to the SWIR range.

The analysis showed that the SWIR and LWIR wavelength ranges, mapped and identified different minerals in the same pixel location of the images. For instance, in Sample 05ch094 (Figure 4.14 C and D), the SWIR range, map jarosite mineral in the veinlet and alunite in the LWIR range. This indicates that SWIR range is sensitive to identify and map jarosite mineral than LWIR range in veinlets. Jarosite is an iron analog of alunite; both are found together because they are solid solution endmembers. Jarosite is formed when Al is replaced by Fe minerals, which often occurs in sulphide-rich fluids. This vein can be related to late-stage mineralization of alunite vein cutting the fine-grained quartz (chalcedony). Therefore, for minerals such as alunite and jarosite occurred in veinlets, combining of the SWIR-LWIR data takes advantage over independent analysis of the dataset.

In completely altered rock samples SWIR and LWIR images can be used to identify similar mineral assemblages, particularly for Alunite, Jarosite, Kaolinite, Nontronite, and Halloysite. In unaltered rock samples, the use of SWIR and LWIR can give different minerals. The reason can be due to the sensitivity of the wavelength range to detect the minerals in pervasive alteration and selective alteration of the rocks. For example, in pervasive alteration, all the minerals are completely altered; therefore both ranges are sensitive in the detection of the secondary mineral. However, the distribution of the mineral map in the rock is not the same. In the case of selective alteration, it consists of primary and secondary minerals, LWIR range is sensitive to detect the primary mineral and SWIR range for the secondary mineral. For example, quartz is more sensitive in LWIR and clay minerals in SWIR.

In the LWIR wavelength range of the sample 07ch003 (Figure 4.9), the wavelength map in the range 8000-11500 nm result the image was highlighted by only green colour quartz mineral. The result were further subset to 8800-9300 nm to see differences in the quartz mineral, then the result highlight reddish colour at a wavelength around 9200 nm, yellowish colour at a wavelength around 9100 nm and few greenish pixels at a wavelength around 9050 nm have a little shift in the deepest absorption feature. They all represent a quartz mineral. The shift of the quartz minerals is due to the mixture with the alunite or jarosite mineral. For instance, the shift of the emissivity minima around 9100 nm is associated with jarosite. The shift around 9050 nm associated with alunite. Indicates that, SWIR range can detect jarosite, alunite, dickite, and nacrite.

LWIR range detect quartz mineral. However, indirectly it is possible to know the presence of alunite and jarosite minerals using a shift of quartz minerals.

Arribas et al., (1995) reported the presence of calcite in the area using petrography and geochemical study. However, SWIR range cannot identify the calcite mineral, but LWIR identify both calcite and dolomite in sample 04MRE008 and 04MRE011. Therefore, this result suggests that LWIR range can easily detect carbonate minerals than SWIR range.

Comparison between the analysis of the SWIR and LWIR data on identification and mapping of the minerals in the rock samples show that the LWIR data takes advantage over the SWIR data especially for the identification of important minerals such as quartz and alunite associated with silicified and advanced argillic alteration zone of the high sulfidation epithermal system. A practical example was observed in the rock samples from these alteration zones (Figure 4.14 and 4.15), where quartz minerals are missed using SWIR range data but well mapped using LWIR range data.

### **5.2.2. SWIR-LWIR combined**

The combined SWIR-LWIR result shows the presence of the most significant mineral assemblages such as quartz dominated (>70%, e.g. sample MRE01013), alunite+quartz (>80% e.g. sample P.012), kaolinite+quartz (>80% e.g. sample 07ch011), kaolinite (>70% e.g. sample 04MRE143), smectite minerals (>50% and presence of crystalline kaolin group minerals e.g. sample MRE01004), chlorite dominated (e.g. sample 04MRE256A). These results suggest that the rocks are affected by pervasive and selective hydrothermal alteration because of the abundance of the important minerals such as HX-kaolinite, nacrite, dickite in the rock sample. For example, in granitic rocks, the presence of low abundance crystalline kaolin group minerals indicate that the rocks has been affected by hydrothermal fluids which results to selective argillic alteration (e.g. sample MRE01004). Kaolinite dominated >70% in the rock samples e.g sample 04MRE0143 indicate pervasive intermediate argillic alteration zone. Alunite + quartz minerals dominated in the rock e.g. sample P.012 also suggest the action of sulfuric acid bearing solutions on these rocks during the oxidation and leaching of metal sulfide deposit. Therefore, the combined SWIR-LWIR result can easily identify altered and unaltered mineral assemblage in the rock samples and locate the different alteration zones in high sulfidation epithermal system.

### **5.2.3. Alteration zone classification of the rock samples**

The spatial distribution of the assigned rock samples (Figure 4.19) from the alteration zones shows an irregular pattern of the alteration zone distribution. This may indicate that multiple veinlets (stock work veining) intruded the Rodalquilar area.

### **5.2.4. Comparison with existing maps**

The differences and similarities of the combined SWIR-LWIR alteration zone result versus the existed alteration map of Arribas et al. (1995) in the Rodalquilar high sulfidation epithermal system was investigated. For example the location of these samples *07cb014*, *07cb003*, *06cb108*, *05cb093*, *06cb163*, *MRE02023*, *MRE02021*, *MRE01010*, *05cb099*, *04MRE146*, *04MRE050*, *MRE02020*, *04MRE045* are exactly matching with the vuggy silica, advanced argillic, intermediate argillic and propylitic of Arribas et al. (1995) (Figure 5.1 A and B). A clear mismatch was also observed in the alteration zones of Arribas et al. (1995) for example in the location of these samples *MRE01053*, *MRE01052*, *MRE01051*, *05cb096*, *07cb009*, *MRE02031*, *MRE02030*, *06cb164*, *MRE02026*, *MRE02025*, *MRE02020*, *MRE01011*, *07cb007*, *MRE01007*, *04MRE054*, *04MRE048(2)*, *04MRE047*, *04MRE046* (Figure 5.1 A and B). Even though the difference between this

study and Arribas et al. (1995) was not checked using geochemical analysis, a lithological map of Arribas et al. (1995) was used to cross-check the alteration zones based on the protolith of the rocks. However, the alteration mineral assemblage of the rocks depends on the composition, temperature, and pressure of the fluid, and composition of the host rock (Heald et al., 1987; Saunders et al., 2013). Mapping of the lithological units also depends on the scale of the geological map.

In general, sample *MRE02025* is assigned to intermediate argillic zone associated with the supergene and rhyolite dome in Arribas et al. (1995). Rhyolite is a felsic volcanic rock composed of mainly quartz, k-feldspar and muscovite. The assumption is that the protolith rock is rhyolite and it is affected by hydrothermal activity in that case the K-feldspar and muscovite can alter to kaolinite and halloysite. The LWIR range result of this sample in Appendix 6 shows the rock is composed of 75% kaolinite, 21% quartz and 4% halloysite. This indicates that k-feldspar and muscovite minerals are entirely altered to kaolinite and halloysite respectively. Halloysite typically forms by hydrothermal alteration of aluminosilicate minerals, and it can occur intermixed with kaolinite, dickite, and montmorillonite (Kerr, 1952). In other places like Wagon wheel Gap, Colorado, United States halloysite minerals are suspected to be the weathering product of rhyolite by downward moving waters (Kerr, 1952). The SWIR range result of this sample (Appendix 4) also showed the presence of both highly crystalline and poorly crystalline kaolinites. Therefore based on the crystallinity of minerals (Garcia, 2013) and the lithology (Arribas et al., 1995), the rock sample has experienced overprinting of hydrothermal alteration and weathering due to downward moving water.

According to Arribas et al. (1995), (Table 2.1) the first advanced argillic zone, the second advanced argillic zone, and argillic zones were not mapped in the area. Maybe the two subclassifications (first advanced argillic and second advanced argillic) of this study can be grouped as an advanced argillic zone, and the argillic zone of this study can be grouped with the intermediate argillic zone of Arribas et al. (1995). However, this study plots those alteration zones in the study area (Figure 4.19 and Figure 5.1).

Within a single alteration zone of Arribas et al. (1995) for example intermediate argillic, advanced argillic (Figure 5.1 A), this study finds 2-3 alteration zones (Figure 5.1). This indicates that multiple veinlets (stockwork veining) intruded the Rodalquilar area.

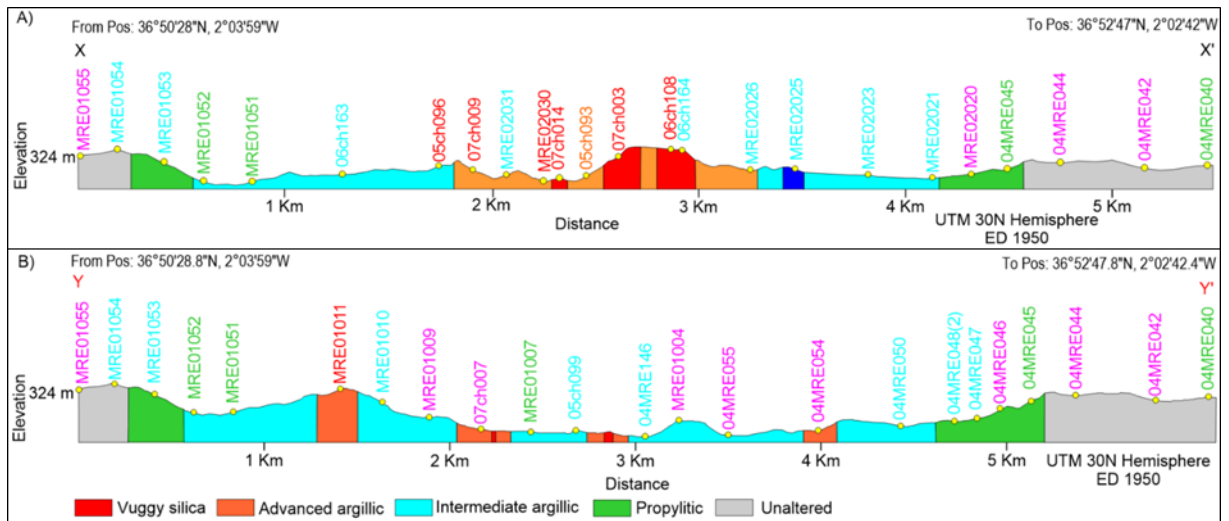


Figure 5.1: Cross-section of the alteration zones of the Rodalquilar area (after Arribas et al., 1995). A) Cross-section of the alteration zones along the profile line X-X,' B) cross-section of the alteration zones along the profile line Y-Y.' The colour of the sample number label represent the alteration zones such as red (silicic), orange (second advanced argillic), cyan (intermediate argillic), magenta (argillic) and green (propylitic)

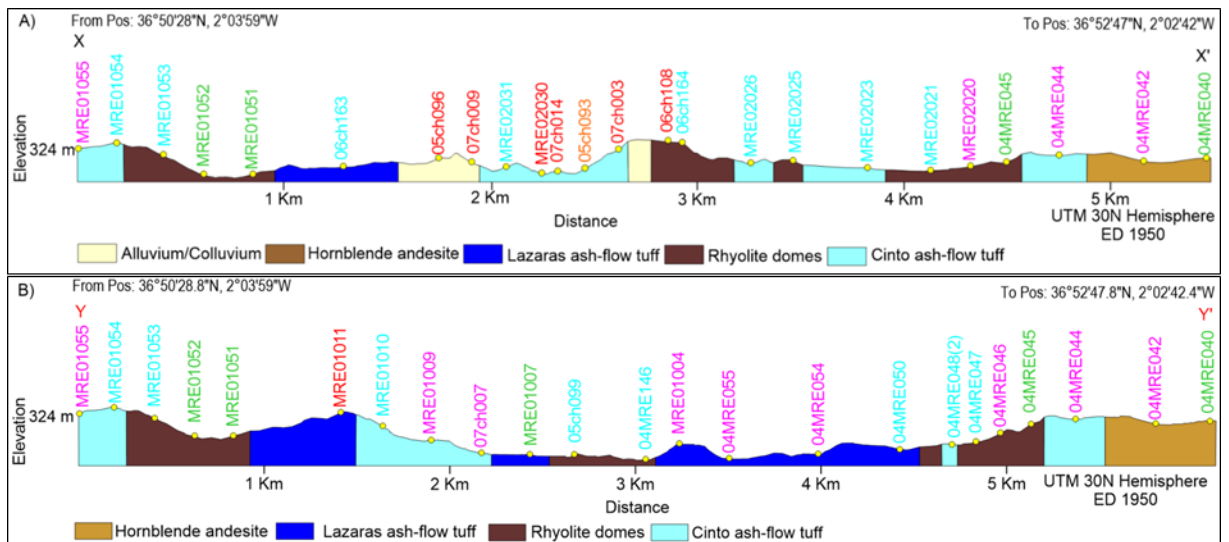


Figure 5.2: lithological cross-section map of the Rodalquilar area and the assigned alteration zones of the rock samples (after Arribas et al., 1995). A) Cross-section of the lithologies along the profile line X-X,' B) cross-section of the lithologies along the profile line Y-Y.' The colour of the sample number label represent the alteration zones such as red (silicic), orange (second advanced argillic), cyan (intermediate argillic), magenta (argillic) and green (propylitic)

## 6. CONCLUSIONS AND RECOMMENDATIONS

In this research, we carried out a mineral spectral study and a mineral mapping in the SWIR and LWIR range of hyperspectral data to characterize rock samples of the Rodalquilar high sulfidation epithermal system. Based on the results and discussion, we can draw the following conclusions.

The use of emissivity data from the LWIR range, and classification using SAM with a 0.05 threshold have proven to be useful in the mineral mapping of rock samples in a high sulfidation epithermal system. Regarding endmember extraction and texture identification, the use of wavelength mapping in a combination of an RGB colour composite of the first interpolated minimum wavelength, the first interpolated depth, and the second interpolated minimum wavelength is suggested for future applications.

Analysis of the SWIR hyperspectral data on rock samples allows mapping of minerals associated with high sulfidation epithermal systems including alunite, jarosite, kaolinite, dickite, nacrite, halloysite, pyrophyllite, montmorillonite, nontronite, and chlorite minerals.

Analysis of the LWIR hyperspectral data on rock samples allows mapping of minerals associated with high sulfidation epithermal systems such as quartz, k-feldspar, pyroxene, anorthite, calcite, and dolomite in addition to the SWIR active minerals including alunite, jarosite, kaolinite, halloysite, and nontronite.

The quartz-feldspar-alunite assemblage characteristics of the central and mineralized part of the high sulfidation epithermal system have a diagnostic emissivity minimum feature in the LWIR wavelength range. They are identified in rocks dominated by quartz, alunite and kaolinite minerals.

From the minerals identified and textures observed in the rocks using SWIR and LWIR image data, it is possible to conclude that the rocks have experienced intensive hydrothermal activity and overprinting of weathering mineralization.

The use of combined SWIR-LWIR hyperspectral image data has advantages over independent analysis of SWIR and LWIR hyperspectral images. This is because quantification of important minerals like nacrite, dickite, pyrophyllites, montmorillonite, and chlorite can only be identified in the SWIR range and not in the LWIR range. Quartz, k-feldspar, pyroxene, hornblende, anorthite, calcite, and dolomite can only be identified in the LWIR range and not in the SWIR range.

The combined SWIR-LWIR data analysis allows mapping of the silicic, first advanced argillic, second advanced argillic, intermediate argillic, argillic and propylitic alteration zones in the Rodalquilar high sulfidation epithermal system. In this study, first advanced argillic zone, second advanced argillic zone and argillic zone are classified, and spatially presented. In the original existing maps, these zones are not distinguished or mapped. Understanding the distribution of these alteration zones provides a better vector to ore mineralization and improves the existing maps of the alteration zones of the Rodalquilar epithermal system in southeast Spain.

This research finally concludes that the use of SWIR-LWIR hyperspectral image data for rock sample characterization in the high sulfidation epithermal system is highly beneficial. This is especially true for the determination of the altered and unaltered minerals in rock samples and offers the possibility to locate the silicic and advanced argillic zone of a high sulfidation epithermal system. The identified alteration zones of

this study also contribute to our understanding of hydrothermal systems and may aid future exploration in delineation and characterization of the alteration zones of a high sulfidation epithermal system.

## **Recommendations**

For validation of the current results, geochemical analysis of the rock samples is recommended both for the mineralogy and the whole rock geochemistry. The geochemical technique for quantifying hydrothermal alteration effects using the Gresens mass balance approach and the alteration box plot approach is recommended. Both approaches allow the identification of alteration reactions and the quantification of the amount of alteration.

Wavelength mapping with RGB combination of the interpolated minimum wavelength of the deepest feature, the interpolated depth of the deepest feature, and the minimum wavelength of the second deepest feature, offer an advantage for the collection of candidate endmembers representative of the minerals in the rock.

The combined SWIR-LWIR range results in this study are only applicable for high sulfidation epithermal system because it was focusing only the significant and dominant hydrothermal indicator minerals in the rock samples. However, for a petrographic study to determine the mineral composition in the rock sample, further study has to be conducted on combining of SWIR and LWIR range data. By comparing both the wavelength range results and comes up with a scientific idea on combining.

## LIST OF REFERENCES

---

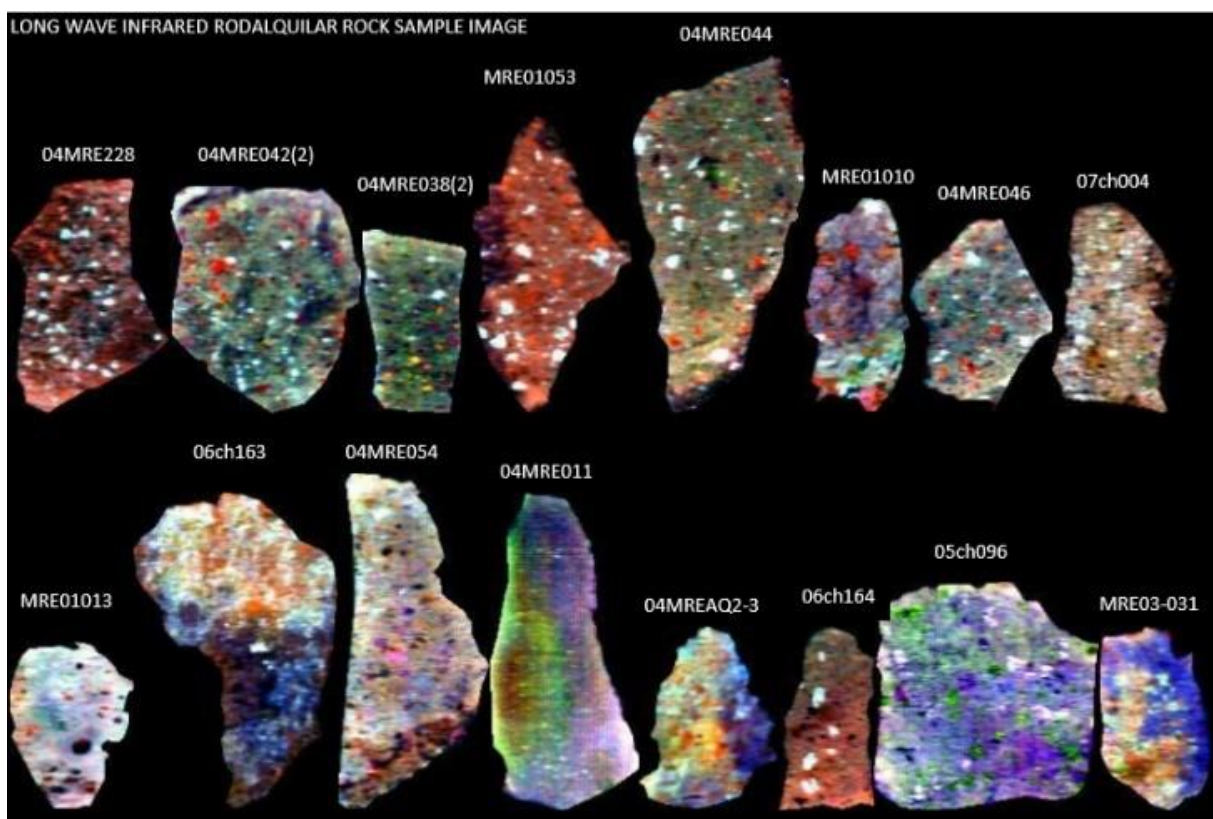
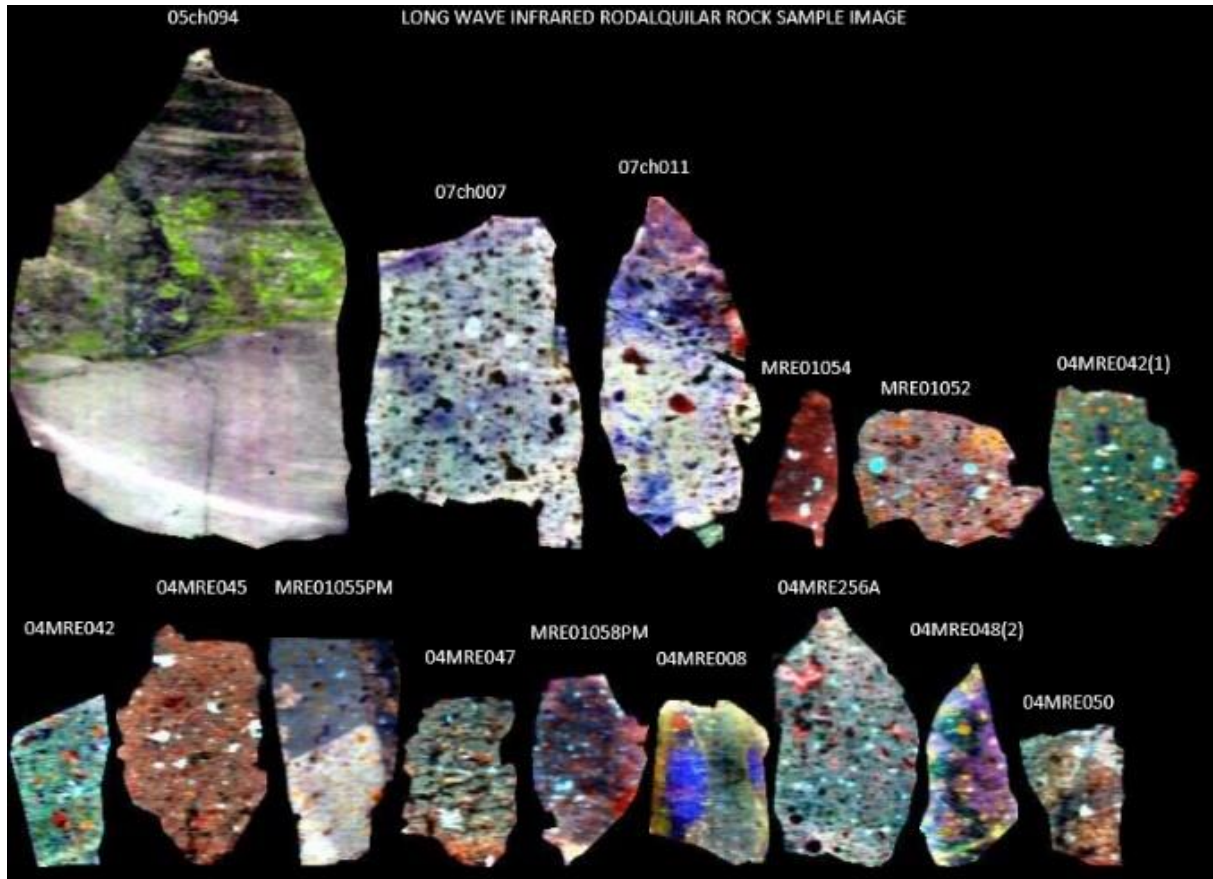
- Arribas, A. (1995). Characteristics of high-sulfidation epithermal deposits, and their relation to magmatic fluid. *Mineralogical Association of Canada Short Course Series*, 23, 419–454.  
<https://doi.org/10.1186/2193-1801-3-130>
- Arribas, A., Cunningham, C. G., Rytuba, J. J., Rye, R. O., Kelly, W. C., Podwyssocki, M. H., ... Tosdal, R. M. (1995). Geology, geochronology, fluid inclusions, and isotope geochemistry of the Rodalquilar gold alunite deposit, Spain. *Economic Geology*, 90(4), 795–822.  
<https://doi.org/10.2113/gsecongeo.90.4.795>
- Bakker, W. H. (2012). HypPy User Manual. Retrieved from  
<http://www.itc.nl/personal/bakker/hyppy.html>
- Bedini, E., van der Meer, F., & van Ruitenbeek, F. (2009). Use of HyMap imaging spectrometer data to map mineralogy in the Rodalquilar caldera, southeast Spain. *International Journal of Remote Sensing*, 30(2), 327–348. <https://doi.org/10.1080/01431160802282854>
- Clark, R. N. (1999). Chapter 1: Spectroscopy of Rocks and Minerals, and Principles of Spectroscopy. In *Manual of Remote Sensing* (Vol. 3, pp. 3–58). John Wiley and Sons, New York: Remote Sensing for the Earth Sciences, (A.N. Rencz, ed.).
- Clark, R. N., Gregg A. Swayze, Richard Wise, K. Eric Livo, Todd M. Hoefen, Raymond F. Kokaly, & Steve J. Sutley. (2003). USGS Digital Spectral Library splib05a. Retrieved August 8, 2018, from <https://pubs.usgs.gov/of/2003/ofr-03-395/ofr-03-395.html>
- Contreras Acosta, I. C. (2017). *Mapping Epithermal alteration mineralogy with high spatial resolution hyperspectral imaging of rock samples*. MSc Thesis, University of Twente Faculty of Geo-Information and Earth Observation (ITC). Retrieved from [http://library.itc.utwente.nl/papers\\_2017/msc/aes/contreras-acosta.pdf](http://library.itc.utwente.nl/papers_2017/msc/aes/contreras-acosta.pdf)
- Cunningham, C. G., Arribas, A., Rytuba, J. J., & Arribas, A. (1990). Mineralized and unmineralized calderas in Spain; Part I, evolution of the Los Frailes Caldera. *Mineralium Deposita*, 25(1), 21–28.  
<https://doi.org/10.1007/BF00205246>
- Debba, P., Carranza, E. J. M., Stein, A., & Meer, F. D. (2009). Deriving optimal exploration target zones on mineral prospectivity maps. *Mathematical Geosciences*, 41(4), 421–446.  
<https://doi.org/10.1007/s11004-008-9181-5>
- Ducart, D. F., Crósta, A. P., Filho, C. R. S., & Coniglio, J. (2006). Alteration mineralogy at the Cerro La Mina epithermal prospect, Patagonia, Argentina: Field mapping, short-wave infrared spectroscopy, and ASTER images. *Economic Geology*, 101(5), 981–996.  
<https://doi.org/10.2113/gsecongeo.101.5.981>
- Forero, J., Zuluaga, C., & Mojica, J. (2011). Alteration Related to Hydrothermal Activity of the Nevado Del Ruiz Volcano (NRV), Colombia. *Boletín de Geología*, 33(1), 59–67.
- García, L. A. G. (2013). *Crystallinity variations of smectite-illite and kaolin hydrothermal alteration minerals by using SWIR spectroscopy. A study of the Rodalquilar Au-deposit, SE Spain*. (Vol. 60). MSc Thesis, University of Twente Faculty of Geo-Information and Earth Observation (ITC). Retrieved from [http://library.itc.utwente.nl/papers\\_2013/msc/aes/guatamegarcia.pdf](http://library.itc.utwente.nl/papers_2013/msc/aes/guatamegarcia.pdf)
- Green, A. A., Berman, M., Switzer, P., & Craig, M. D. (1988). A Transformation for Ordering Multispectral Data in Terms of Image Quality with Implications for Noise Removal. *IEEE Transactions on Geoscience and Remote Sensing*, 26(1), 65–74. <https://doi.org/10.1109/36.3001>
- Hauff, P. (1983). An overview of VIS-NIR-SWIR field spectroscopy as applied to precious metals exploration. *Arvada, Colorado: Spectral International Inc, 80001*, 303–403.
- Heald, P., Foley, N. K., & Hayba, D. O. (1987). Comparative anatomy of volcanic-hosted epithermal deposits: acid- sulfate and adularia- sericite types. *Economic Geology*, 82(1), 1–26.  
<https://doi.org/10.2113/gsecongeo.82.1.1>
- Hecker, C., Van Der Meijde, M., Van Der Werff, H., & Van Der Meer, F. D. (2008). Assessing the influence of reference spectra on synthetic SAM classification results. *IEEE Transactions on Geoscience and Remote Sensing*, 46(12), 4162–4172. <https://doi.org/10.1109/TGRS.2008.2001035>
- Hedenquist, J. W., Arribas, A., & Gonzalez-Urien, E. (2000). Chapter 7 Exploration for Epithermal Gold Deposits. *SEG Reviews*, 13(1), 245–277. <https://doi.org/07410123>
- Hedenquist, J. W., Arribas, A., & Gonzalez, E. (2000). *Chapter 7 Exploration for Epithermal Gold Deposits*

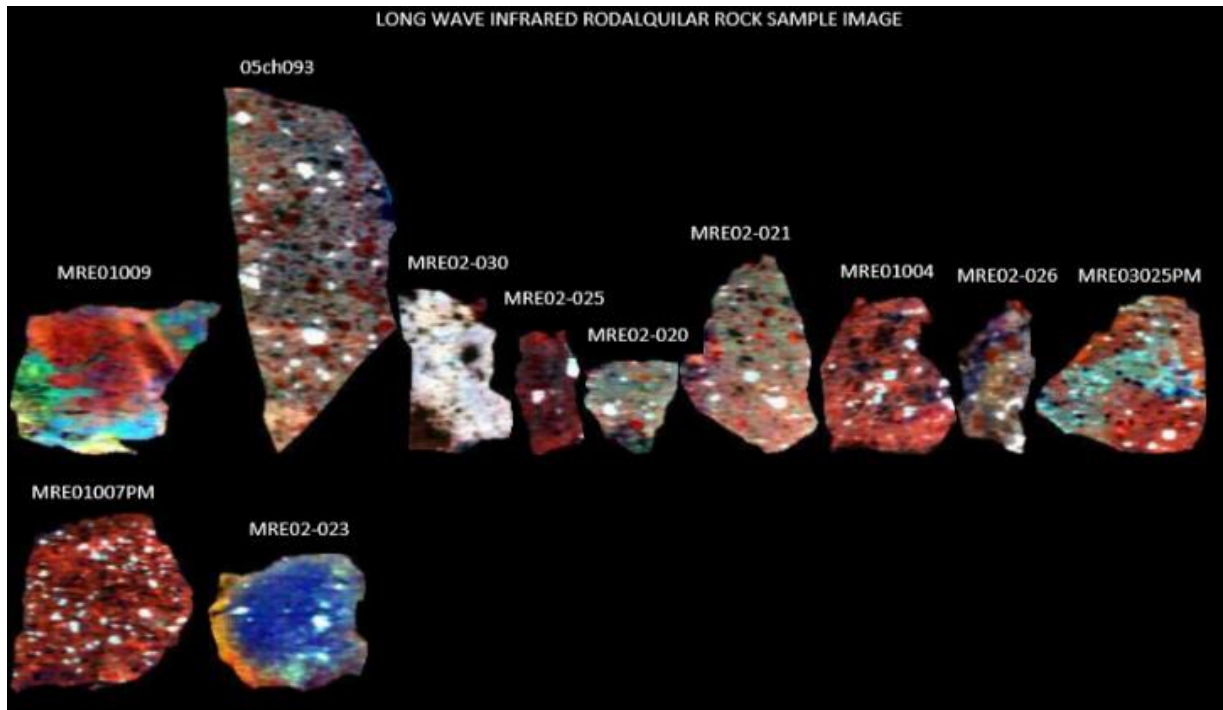
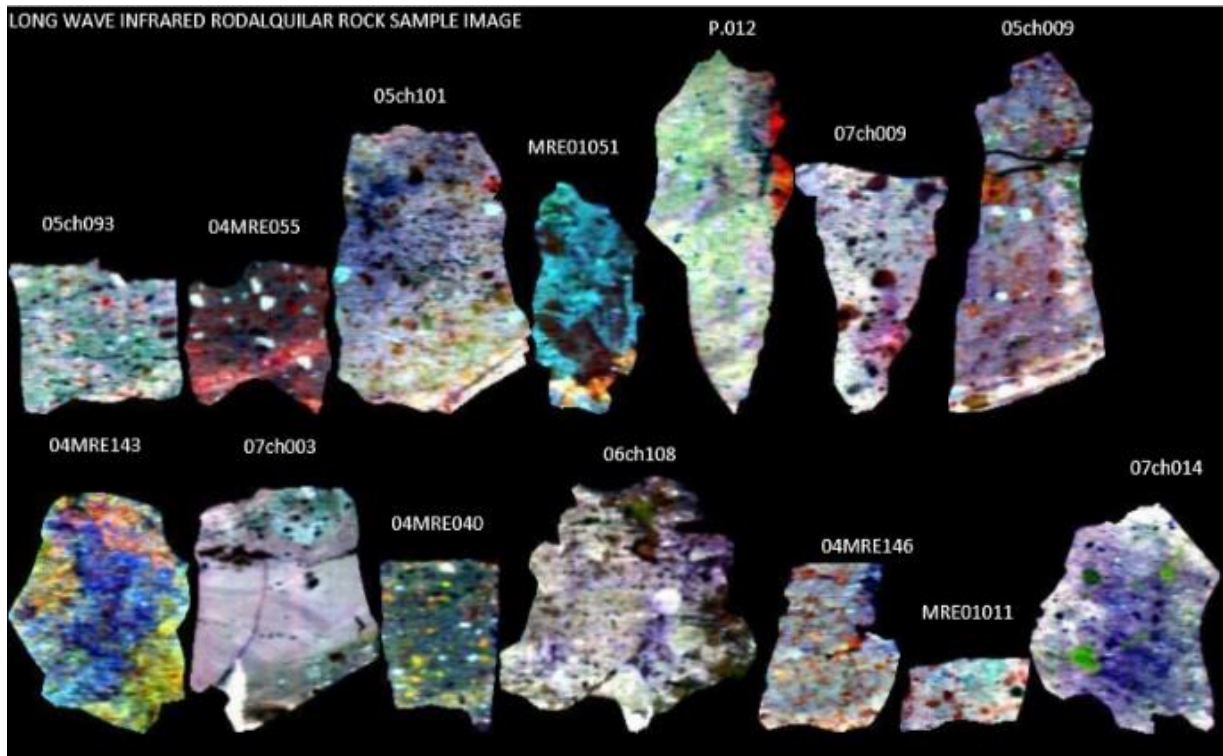
- (Vol. 13).
- Hsu, L. C. (1986). The stability relations of Zunyite under Hydrothermal Conditions. *Mining Geology*, 36(3), 219–230.
- Kerr, P. F. (1952). Formation and Occurrence of Clay Minerals. *Clays and Clay Minerals*, 1(1), 19–32. <https://doi.org/10.1346/CCMN.1952.0010104>
- Kuosmanen, V., Arkimaa, H., & Tiainen, M. (2015). Hyperspectral close-range LWIR imaging spectrometry - 3 case studies. *Geological Survey of Finland, Special Paper 58*, 117–144.
- Mathieu, M., Roy, R., Launeau, P., Cathelineau, M., & Quirt, D. (2017). Alteration mapping on drill cores using a HySpex SWIR-320m hyperspectral camera: Application to the exploration of an unconformity-related uranium deposit (Saskatchewan, Canada). *Journal of Geochemical Exploration*, 172, 71–88. <https://doi.org/10.1016/j.gexplo.2016.09.008>
- Morishita, Y., & Nakano, T. (2008). Role of basement in epithermal deposits: The Kushikino and Hishikari gold deposits, southwestern Japan. *Ore Geology Reviews*, 34(4), 597–609. <https://doi.org/10.1016/j.oregeorev.2008.09.009>
- Pirajno, F. (2009). *Hydrothermal processes and mineral systems*. Springer/Geological Survey of Western Australia.
- Pontual, S., Merry, N., & Gamson, P. (1997a). Epithermal alteration systems. *AusSpec International Pty.*
- Pontual, S., Merry, N., & Gamson, P. (1997b). Spectral Interpretation Field Manual. *AusSpec International Pty.*
- Riley, D. N., & Hecker, C. A. (2013). Mineral Mapping with Airborne Hyperspectral Thermal Infrared Remote Sensing at Cuprite, Nevada, USA (pp. 495–514). Springer, Dordrecht. [https://doi.org/10.1007/978-94-007-6639-6\\_24](https://doi.org/10.1007/978-94-007-6639-6_24)
- Rytuba, J. J., Arribas, A., Cunningham, C. G., McKee, E. H., Podwysoki, M. H., Smith, J. G., ... Arribas, A. (1990). Mineralized and unmineralized calderas in Spain; Part II, evolution of the Rodalquilar caldera complex and associated gold-alunite deposits. *Mineralium Deposita*, 25(1), 29–35. <https://doi.org/10.1007/BF00205247>
- Saunders, J. A., Hofstra, A. H., Goldfarb, R. J., & Reed, M. H. (2013). Geochemistry of Hydrothermal Gold Deposits. *Treatise on Geochemistry: Second Edition*, 13(3), 383–424. <https://doi.org/10.1016/B978-0-08-095975-7.01117-7>
- Van der Meer, F. D., Kopačková, V., Koucká, L., Van der Werff, H. M. A., Van Ruitenbeek, F. J. A., & Bakker, W. H. (2018). Wavelength feature mapping as a proxy to mineral chemistry for investigating geologic systems: An example from the Rodalquilar epithermal system. *International Journal of Applied Earth Observation and Geoinformation*, 64, 237–248. <https://doi.org/10.1016/j.jag.2017.09.008>
- Van der Meer, F. D., & Van der Werff, H. M.A. (2007). Spatial-spectral contextual image analysis of hyperspectral data to aid in the characterisation of hydrothermal alteration in epithermal gold deposits. *New Developments and Challenges in Remote Sensing*, 275–285.
- Van der Meer, F. D., Van der Werff, H. M. A., Van Ruitenbeek, F. J. A., Hecker, C. A., Bakker, W. H., Noomen, M. F., ... Woldai, T. (2012). Multi- and hyperspectral geologic remote sensing: A review. *International Journal of Applied Earth Observation and Geoinformation*, 14(1), 112–128. <https://doi.org/10.1016/J.JAG.2011.08.002>

# APPENDICES

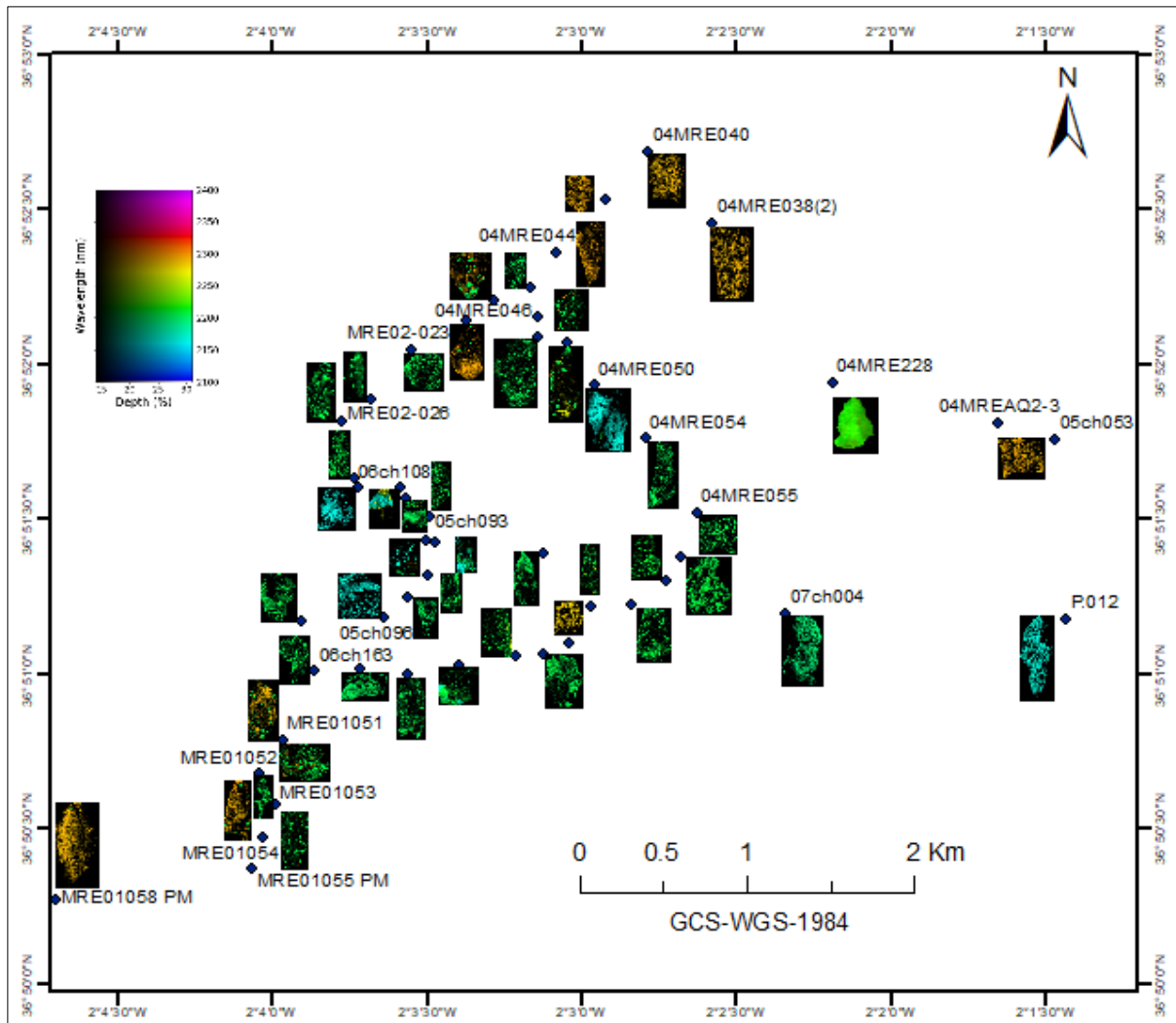
## Appendix 1. Image acquisitions

LWIR image acquisitions (RGB=9505 nm, 9067 nm, 8288 nm)

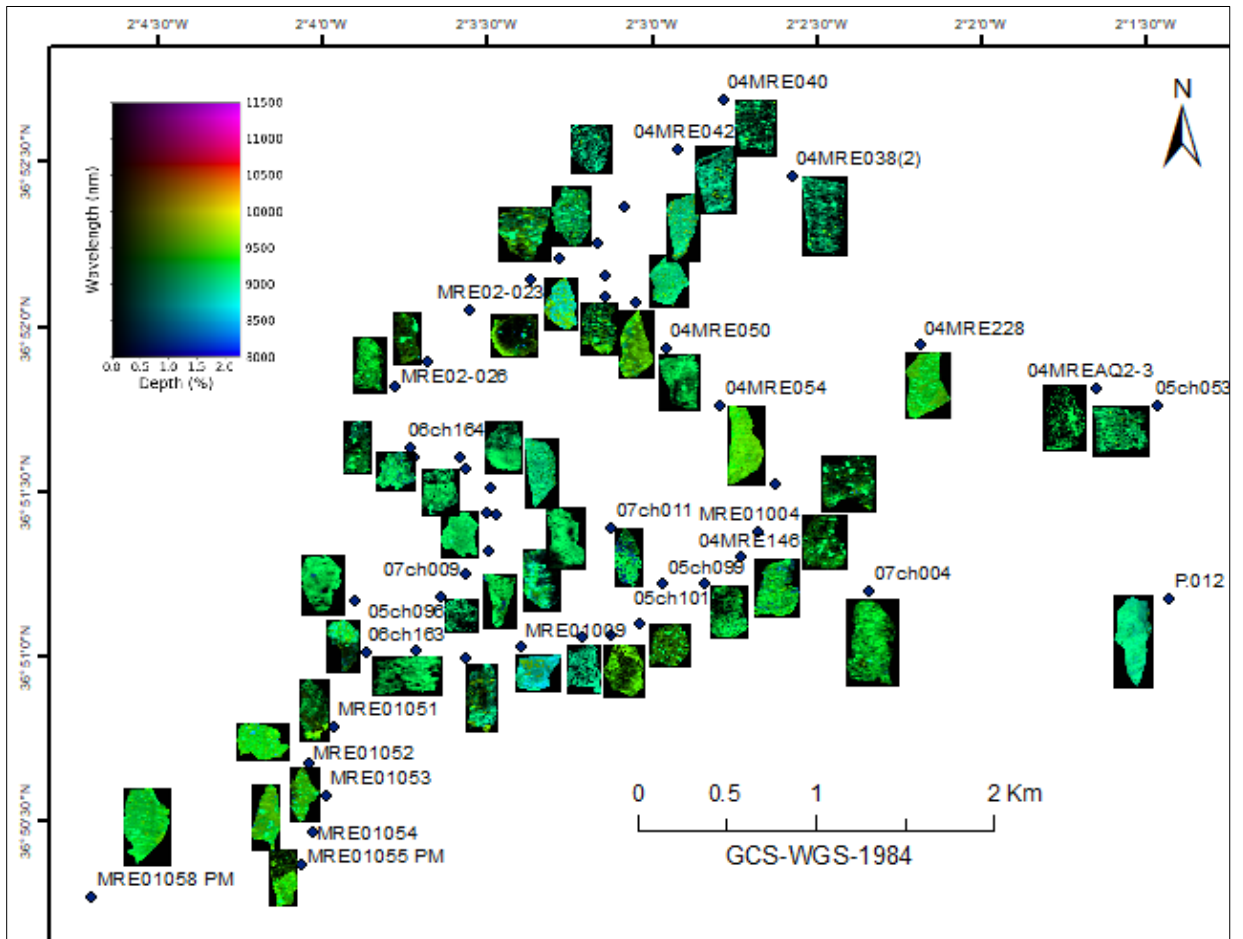




Appendix 2: SWIR wavelength map between the wavelength range 2100-2400 nm



Appendix 3: LWIR wavelength map between the wavelength range 8000-11500 nm



Appendix 4: SWIR mineral abundance of the rock samples

Sample_code	Easting	Northing	SAM-Mineral abundance (%)													
			Alunite	Alunite+water	Dickite	Pyrophyllite	Nacrite	Chlorite	D-Halloysite	H-Halloysite	Jarosite	PX-Kaolinite	HX-Kaolinite	Montmorillonite	Nontronite	Unclassified
04MRE008			0	0	0	17	0	0	0	0	0	0	0	0	63	19
04MRE011			0	0	0	0	0	0	0	0	19	0	0	12	45	24
04MRE038(2)	585301	4081418	0	0	0	8	34	0	0	0	16	2	0	1	14	25
04MRE040	584988	4081842	0	0	0	0	2	0	0	0	19	2	0	0	10	65
04MRE042	584789	4081559	0	0	0	0	3	0	0	0	18	1	4	2	23	49
04MRE042(1)	584789	4081559	0	0	0	24	4	0	0	0	12	1	0	1	19	40
04MRE042(2)	584789	4081559	0	0	0	2	3	0	0	0	35	3	0	1	8	50
04MRE044	584547	4081237	0	0	0	5	5	0	0	0	0	6	0	1	73	10
04MRE045	584430	4081026	0	0	0	0	0	0	0	0	0	19	0	1	67	12
04MRE046	584470	4080853	0	0	0	6	8	0	0	2	2	44	1	1	28	8
04MRE047	584469	4080732	0	0	0	18	1	0	0	1	3	7	0	0	60	10
04MRE048(2)	584607	4080699	0	0	0	0	1	0	0	0	22	18	0	1	3	55
04MRE050	584742	4080445	0	0	0	0	7	0	0	0	2	0	62	1	18	10
04MRE054	584992	4080128	0	0	0	2	20	0	0	0	2	0	15	39	21	0
04MRE055	585241	4079687	0	0	0	10	2	0	0	1	1	0	22	59	4	1
04MRE143	584510	4078837	0	0	2	28	2	0	0	2	0	0	63	1	0	2
04MRE146	585094	4079274	0	0	0	0	2	0	0	0	12	2	9	19	41	14
04MRE228	585887	4080472	0	0	69	0	0	0	6	10	0	0	14	0	0	1
04MRE256A			0	0	0	0	0	60	0	0	13	4	0	0	0	23
04MREAQ2-3	586684	4080240	0	0	60	0	0	0	5	9	0	0	15	9	0	2
05ch053	586958	4080146	0	0	0	8	3	0	0	0	31	3	0	0	5	50
05ch093	583961	4079654	0	0	0	24	6	0	0	0	23	0	11	20	11	5
05ch094	583819	4079828	19	2	0	0	0	0	0	0	48	0	1	0	0	30
05ch096	583746	4079044	35	0	0	11	15	0	0	0	7	5	9	0	1	17
05ch099	584737	4079121	0	0	0	8	35	0	0	1	12	4	1	20	16	3
05ch101	584933	4079130	0	0	0	0	10	0	0	0	5	5	9	24	30	16
06ch108	583613	4079821	0	0	0	42	21	0	0	0	15	1	3	1	11	5
06ch163	583413	4078725	0	0	0	0	0	0	0	6	0	0	18	0	0	76
06ch164	583595	4079876	0	0	0	0	0	0	0	3	0	2	45	4	5	42
07ch003	583845	4079758	0	0	0	0	18	0	0	0	37	32	0	0	0	13
07ch004	585670	4079091	0	0	0	10	14	0	0	0	21	1	0	1	45	9
07ch007	584381	4078823	0	0	0	0	9	0	0	0	4	0	9	65	5	7
07ch009	583856	4079167	0	0	7	0	0	0	0	2	3	0	48	0	5	36
07ch011	584506	4079435	0	0	1	0	0	0	0	0	0	17	24	22	16	20
07ch014	583944	4079509	5	1	0	4	2	0	0	0	9	8	2	7	48	16
MRE01004	585171	4079421	0	0	0	6	2	0	0	0	1	1	4	21	59	7
MRE01007	584639	4078901	0	0	0	0	0	0	0	0	7	42	0	14	27	10
MRE01009	584104	4078762	0	0	0	0	11	0	0	0	41	0	2	1	29	16
MRE01010	583859	4078703	0	0	0	0	0	0	0	2	9	0	40	0	9	40
MRE01011	583636	4078738	0	0	24	0	0	0	1	40	3	0	7	0	0	25
MRE01013	583352	4079016	0	0	2	0	43	0	0	0	33	12	5	0	0	4
MRE01051	583267	4078307	0	0	0	0	0	0	0	0	61	0	9	0	0	30
MRE01052	583155	4078106	0	0	0	0	0	0	0	0	73	16	0	0	1	10
MRE01053	583236	4077924	0	0	0	0	2	0	0	0	15	35	0	0	22	25
MRE01054	583180	4077721	0	0	0	0	28	0	0	0	7	23	0	5	36	1
MRE01055	583128	4077539	0	0	0	0	0	0	0	0	3	23	0	2	70	3
MRE01058	582183	4077342	0	0	0	0	0	0	0	0	16	20	0	1	35	28
MRE02020	584256	4080946	0	0	0	2	0	0	0	0	11	55	0	0	24	8
MRE02021	584127	4080828	0	0	0	0	0	0	0	0	0	9	0	20	66	5
MRE02023	583858	4080649	0	0	4	2	0	0	0	4	1	0	75	13	0	1
MRE02025	583670	4080354	0	0	0	8	0	0	0	0	0	21	1	52	0	17
MRE02026	583527	4080215	1	0	0	0	0	0	0	1	0	0	57	1	27	13
MRE02030	583987	4079500	0	0	10	5	0	0	1	79	0	0	0	0	0	5
MRE02031	583956	4079303	7	1	8	0	0	0	0	26	0	0	52	0	0	6
MRE03025	580848	4078979	0	0	0	1	16	0	0	0	12	9	1	51	1	10
P_012	587024	4079067	75	1	0	0	0	0	0	0	0	0	4	0	0	18

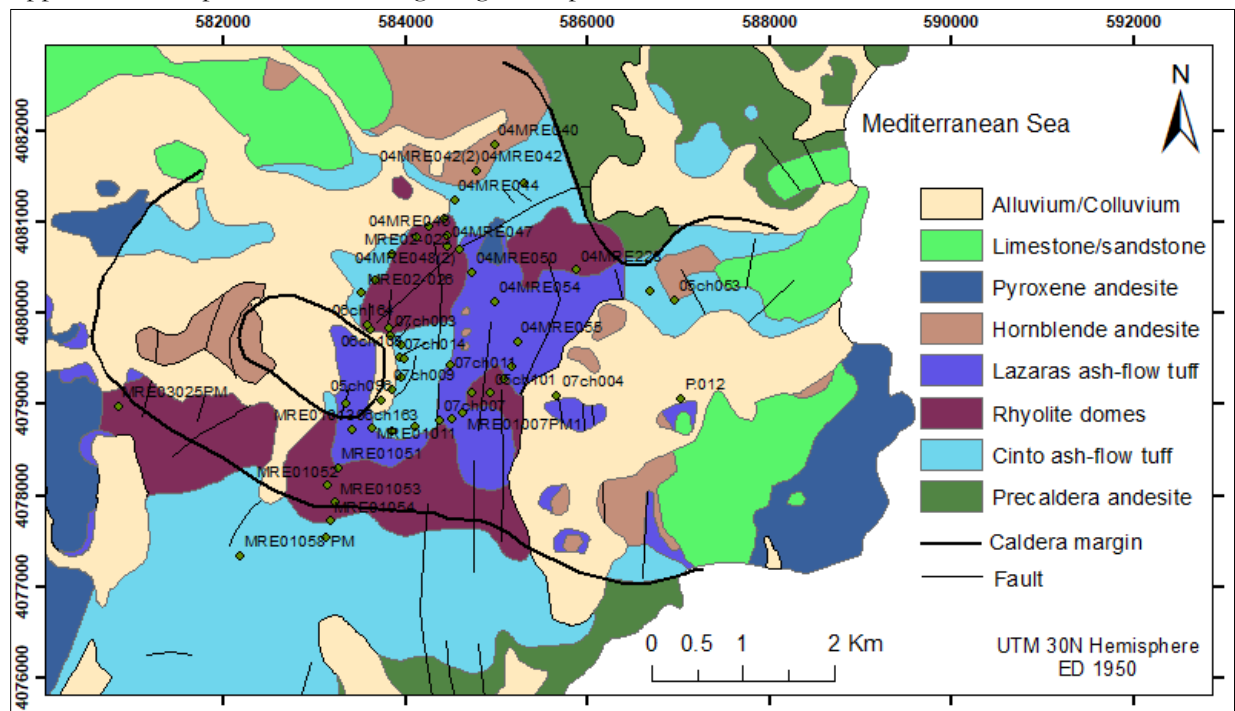
Appendix 5: LWIR mineral abundance of the rock samples

Sample_code	Easting	Northing	SAM-Mineral abundance (%)															
			Alunite	Halloysite	Jarosite	Kaolinite	Nontronite	Quartz-1	Quartz-2	K-feldspar	Pyroxene	Anorthite	Hornblende	Calcite	Dolomite	Unclassified		
04MRE008			0	0	0	0	5	0	0	0	0	0	0	0	0	0	0	0
04MRE011			0	0	0	0	0	0	0	0	0	0	0	0	0	100	0	0
04MRE038(2)	585301	4081418	1	0	8	0	11	0	4	0	4	73	0	0	0	0	0	0
04MRE040	584988	4081842	41	0	0	0	51	0	9	0	0	0	0	0	0	0	0	0
04MRE042	584789	4081559	0	0	6	0	93	0	1	0	0	0	0	0	0	0	0	0
04MRE042(1)	584789	4081559	0	0	19	0	69	0	12	0	0	0	0	0	0	0	0	0
04MRE042(2)	584789	4081559	0	0	54	0	40	0	6	0	0	0	0	0	0	0	0	0
04MRE044	584547	4081237	0	0	0	0	73	0	9	0	0	18	0	0	0	0	0	0
04MRE045	584430	4081026	0	0	0	0	86	1	13	0	0	0	0	0	0	0	0	0
04MRE046	584470	4080853	0	0	14	0	57	0	0	0	0	29	0	0	0	0	0	0
04MRE047	584469	4080732	0	90	0	0	0	0	11	0	0	0	0	0	0	0	0	0
04MRE048(2)	584607	4080699	0	83	0	0	17	0	0	0	0	0	0	0	0	0	0	0
04MRE050	584742	4080445	5	0	0	92	0	0	3	0	0	0	0	0	0	0	0	0
04MRE054	584992	4080128	0	10	0	0	0	0	2	88	0	0	0	0	0	0	0	0
04MRE055	585241	4079687	0	0	0	0	89	0	11	0	0	0	0	0	0	0	0	0
04MRE143	584510	4078837	0	0	0	71	0	0	0	29	0	0	0	0	0	0	0	0
04MRE146	585094	4079274	0	0	0	59	5	0	5	30	0	0	0	0	0	0	0	0
04MRE228	585887	4080472	0	0	0	85	0	0	15	0	0	0	0	0	0	0	0	0
04MRE256A			0	0	95	0	0	0	5	0	0	0	0	0	0	0	0	0
04MREAQ2-3	586684	4080240	0	0	0	78	15	0	2	5	0	0	0	0	0	0	0	0
05ch053	586958	4080146	0	0	70	0	0	0	7	0	0	23	0	0	0	0	0	0
05ch093	583961	4079654	0	0	0	64	11	0	23	2	0	0	0	0	0	0	0	0
05ch094	583819	4079828	26	0	43	0	0	0	31	0	0	0	0	0	0	0	0	0
05ch096	583746	4079044	34	0	0	0	0	0	66	0	0	0	0	0	0	0	0	0
05ch099	584737	4079121	10	0	78	0	0	0	12	0	0	0	0	0	0	0	0	0
05ch101	584933	4079130	0	0	0	40	2	0	9	49	0	0	0	0	0	0	0	0
06ch108	583613	4079821	20	0	1	16	0	2	60	0	0	0	0	0	0	0	0	0
06ch163	583413	4078725	0	2	0	96	0	0	2	0	0	0	0	0	0	0	0	0
06ch164	583595	4079876	0	0	0	78	2	0	20	0	0	0	0	0	0	0	0	0
07ch003	583845	4079758	18	0	9	0	0	0	72	0	0	0	0	0	0	0	0	0
07ch004	585670	4079091	0	0	0	99	0	0	1	0	0	0	0	0	0	0	0	0
07ch007	584381	4078823	0	0	82	0	17	0	1	0	0	0	0	0	0	0	0	0
07ch009	583856	4079167	0	0	0	33	0	0	66	0	0	0	0	0	0	0	0	0
07ch011	584506	4079435	0	0	5	70	0	0	25	0	0	0	0	0	0	0	0	0
07ch014	583944	4079509	22	0	0	5	0	0	73	0	0	0	0	0	0	0	0	0
MRE01004	585171	4079421	0	0	0	0	75	0	25	0	0	0	0	0	0	0	0	0
MRE01007	584639	4078901	0	0	0	0	82	0	18	0	0	0	0	0	0	0	0	0
MRE01009	584104	4078762	0	0	41	0	59	0	0	0	0	0	0	0	0	0	0	0
MRE01010	583859	4078703	0	0	1	95	0	0	4	0	0	0	0	0	0	0	0	0
MRE01011	583636	4078738	0	0	0	48	0	0	52	0	0	0	0	0	0	0	0	0
MRE01013	583352	4079016	0	0	3	15	0	0	82	0	0	0	0	0	0	0	0	0
MRE01051	583267	4078307	0	0	71	0	22	0	7	0	0	0	0	0	0	0	0	0
MRE01052	583155	4078106	0	0	11	0	89	0	1	0	0	0	0	0	0	0	0	0
MRE01053	583236	4077924	0	0	2	60	20	0	18	0	0	0	0	0	0	0	0	0
MRE01054	583180	4077721	1	79	16	0	3	0	1	0	0	0	0	0	0	0	0	0
MRE01055	583128	4077539	0	7	0	0	87	0	6	0	0	0	0	0	0	0	0	0
MRE01058	582183	4077342	5	0	2	73	1	0	2	17	0	0	0	0	0	0	0	0
MRE02020	584256	4080946	0	19	0	0	68	2	12	0	0	0	0	2	0	0	0	0
MRE02021	584127	4080828	0	0	0	71	14	0	15	0	0	0	0	0	0	0	0	0
MRE02023	583858	4080649	0	2	0	85	4	0	9	0	0	0	0	0	0	0	0	0
MRE02025	583670	4080354	0	4	0	75	0	0	21	0	0	0	0	0	0	0	0	0
MRE02026	583527	4080215	7	1	0	76	0	0	16	0	0	0	0	0	0	0	0	0
MRE02030	583987	4079500	21	0	0	8	0	0	71	0	0	0	0	0	0	0	0	0
MRE02031	583956	4079303	17	28	0	0	55	0	0	0	0	0	0	0	0	0	0	0
MRE03025	580848	4078979	14	0	1	10	3	0	6	66	0	0	0	0	0	0	0	0
P.012	587024	4079067	63	0	3	12	0	0	22	0	0	0	0	0	0	0	0	0

Appendix 6: Dominant mineral assemblages in the rock samples and alteration types

Sample_code	Easting	Northing	Dominant mineral assemblages		SWIR-LWIR significance mineral assemblages	Alteration zone
			SWIR Decreasing abundance →	LWIR Decreasing abundance →		
04MRE008			Nontronite, Pyrophyllite	Calcite, Kaolinite, Dolomite	Calcite, Nontronite, Pyrophyllite, Kaolinite	Argillic
04MRE011			Nontronite, Jarosite, Montmorillonite	Calcite	Calcite, Nontronite, Montmorillonite	Propylitic
04MRE038(2)	585301	4081418	Nacrite, Jarosite, PX-kaolinite, Pyrophyllite	Anorthite, Nontronite, Quartz-2	Nacrite, Nontronite, Pyrophyllite, Quartz-2	Intermediate argillic
04MRE040	584988	4081842	Jarosite, Nontronite	Nontronite, Alunite, Quartz-2	Nontronite, Alunite, Quartz-2	Propylitic
04MRE042	584789	4081559	Nontronite, Jarosite, HX-kaolinite, Nacrite	Nontronite, Jarosite	Nontronite, HX-kaolinite, Nacrite	Argillic
04MRE042(1)	584789	4081559	Pyrophyllite, Nontronite, Jarosite, Nacrite	Nontronite, Jarosite, Quartz-2	Nontronite, Pyrophyllite, Quartz-2, Nacrite	Argillic
04MRE042(2)	584789	4081559	Jarosite, Nontronite, Nacrite, PX-kaolinite	Jarosite, Nontronite, Quartz-2	Nontronite, Quartz-2, Nacrite	Argillic
04MRE044	584547	4081237	Nontronite, PX-kaolinite, Pyrophyllite, Nacrite	Nontronite, Anorthite, Quartz-2	Nontronite, Quartz-2, Pyrophyllite, Nacrite	Argillic
04MRE045	584430	4081026	Nontronite, PX-kaolinite	Nontronite, Quartz-2	Nontronite, Quartz-2	Propylitic
04MRE046	584470	4080853	PX-kaolinite, Nontronite, Nacrite, Pyrophyllite	Nontronite, Anorthite, Jarosite	Nontronite, Nacrite, Pyrophyllite	Argillic
04MRE047	584469	4080732	Nontronite, Pyrophyllite, PX-kaolinite, Jarosite	Halloysite, Quartz-2	Halloysite, Nontronite, Pyrophyllite, Quartz-2	Intermediate argillic
04MRE048(2)	584607	4080699	Jarosite, PX-kaolinite, Nontronite	Halloysite, Nontronite	Halloysite, Nontronite	Intermediate argillic
04MRE050	584742	4080445	HX-kaolinite, Nontronite, Nacrite	Kaolinite, Alunite, Quartz-2	Kaolinite, HX-kaolinite, Nontronite, Nacrite, Alunite	Intermediate argillic
04MRE054	584992	4080128	Montmorillonite, Nontronite, Nacrite, HX-kaolinite	K-feldspar, Halloysite	Montmorillonite, Nontronite, Nacrite	Argillic
04MRE055	585241	4079687	Montmorillonite, HX-kaolinite, Pyrophyllite	Nontronite, Quartz-2	Nontronite, Montmorillonite, HX-kaolinite, Pyrophyllite	Argillic
04MRE143	584510	4078857	HX-kaolinite, Pyrophyllite	Kaolinite, K-feldspar	Kaolinite, HX-kaolinite, Pyrophyllite	Intermediate argillic
04MRE146	585094	4079274	Nontronite, Montmorillonite, Jarosite, HX-kaolinite	Kaolinite, K-feldspar, Quartz-2, Nontronite	Kaolinite, Nontronite, Montmorillonite, HX-kaolinite	Intermediate argillic
04MRE228	585887	4080472	Dickite, HX-kaolinite, D-Halloysite	Kaolinite, Quartz-2	Kaolinite, Dickite, HX-kaolinite, Quartz-2, D-Halloysite	Intermediate argillic
04MRE256A			Chlorite, Jarosite, PX-kaolinite	Jarosite, Quartz-2	Chlorite, Quartz-2	Propylitic
04MREAQ2-3	586684	4080240	Dickite, HX-kaolinite, Montmorillonite, D-Halloysite	Kaolinite, Nontronite, K-feldspar	Kaolinite, Dickite, HX-kaolinite, Montmorillonite, Nontronite	Intermediate argillic
05ch053	586958	4080146	Jarosite, Pyrophyllite, Nontronite, Nacrite	Jarosite, Anorthite, Quartz-2	Pyrophyllite, Quartz-2, Nontronite, Nacrite	Intermediate argillic
05ch093	583961	4079654	Pyrophyllite, Jarosite, Montmorillonite, HX-kaolinite	Kaolinite, Quartz-2, Nontronite	Kaolinite, Quartz-2, Pyrophyllite, Montmorillonite, Nontronite	2nd Advanced argillic
05ch094	583819	4079828	Jarosite, Alunite	Jarosite, Quartz-2, Alunite	Quartz-2, Alunite	Silicic
05ch096	583746	4079044	Alunite, Nacrite, Pyrophyllite, HX-kaolinite	Quartz-2, Alunite	Quartz-2, Alunite, Nacrite, Pyrophyllite, HX-kaolinite	Silicic
05ch099	584737	4079121	Nacrite, Montmorillonite, Nontronite, Pyrophyllite	Jarosite, Quartz-2, Alunite	Nacrite, Quartz-2, Alunite, Montmorillonite, Nontronite	Intermediate argillic
05ch101	584933	4079130	Nontronite, Montmorillonite, Nacrite, HX-kaolinite	K-feldspar, Kaolinite, Quartz-2	Kaolinite, Nontronite, Nacrite, HX-kaolinite, Quartz-2	Intermediate argillic
06ch108	583613	4079821	Pyrophyllite, Nacrite, Jarosite, HX-kaolinite	Quartz-2, Alunite, Kaolinite	Quartz-2, Pyrophyllite, Nacrite, HX-kaolinite	Silicic
06ch163	583413	4078725	HX-kaolinite, H-Halloysite	Kaolinite, Quartz-2, Halloysite	Kaolinite, HX-kaolinite, Quartz-2, Halloysite	Intermediate argillic
06ch164	583595	4079876	HX-kaolinite, Nontronite, Montmorillonite	Kaolinite, Quartz-2,	Kaolinite, HX-kaolinite, Quartz-2, Nontronite, Montmorillonite	Intermediate argillic
07ch003	583845	4079758	Jarosite, PX-kaolinite, Nacrite	Quartz-2, Alunite, Jarosite	Quartz-2, Alunite, PX-kaolinite, Nacrite	Silicic
07ch004	585670	4079091	Nontronite, Jarosite, Nacrite, Pyrophyllite	Kaolinite	Kaolinite, Nontronite, Nacrite, Pyrophyllite	Intermediate argillic
07ch007	584381	4078823	Montmorillonite, HX-kaolinite, Nacrite	Jarosite, Nontronite	Montmorillonite, Nontronite, HX-kaolinite, Nacrite	Argillic
07ch009	583856	4079167	HX-kaolinite, Dickite, Nontronite	Quartz-2, Kaolinite	Quartz-2, HX-kaolinite, Kaolinite, Dickite, Nontronite	Silicic
07ch011	584506	4079435	HX-kaolinite, Montmorillonite, PX-kaolinite	Kaolinite, Quartz-2, Jarosite	Kaolinite, HX-kaolinite, Quartz-2, Montmorillonite	2nd Advanced argillic
07ch014	583944	4079509	Nontronite, Jarosite, PX-kaolinite, alunite	Quartz-2, Alunite, kaolinite	Quartz-2, Alunite, Nontronite, kaolinite	Silicic
MRE01004	585171	4079421	Nontronite, Montmorillonite, Pyrophyllite, HX-kaolinite	Nontronite, Quartz-2	Nontronite, Quartz-2, Montmorillonite, Pyrophyllite	Argillic
MRE01007	584639	4078901	PX-kaolinite, Nontronite, Montmorillonite	Nontronite, Quartz-2	Nontronite, Montmorillonite, Quartz-2	Propylitic
MRE01009	584104	4078762	Jarosite, Nontronite, Nacrite	Nontronite, Jarosite	Nontronite, Nacrite	Argillic
MRE01010	583859	4078703	HX-kaolinite, Jarosite, Nontronite	Kaolinite, Quartz-2	Kaolinite, HX-kaolinite, Quartz-2, Nontronite	Intermediate argillic
MRE01011	583636	4078738	H-Halloysite, Dickite, HX-kaolinite	Quartz-2, Kaolinite	Quartz-2, Kaolinite, Dickite	Silicic
MRE01013	583352	4079016	Nacrite, Jarosite, PX-kaolinite, HX-kaolinite	Quartz-2, kaolinite, Jarosite	Quartz-2, Nacrite, Kaolinite, HX-kaolinite	Silicic
MRE01051	583267	4078307	Jarosite, PX-kaolinite	Jarosite, Nontronite, Quartz-2	Nontronite, Quartz-2	Propylitic
MRE01052	583155	4078106	Jarosite, PX-kaolinite	Nontronite, Jarosite	Nontronite	Propylitic
MRE01053	583236	4077924	PX-kaolinite, Nontronite, Jarosite	Kaolinite, Nontronite, Quartz-2	Kaolinite, Nontronite, Quartz-2	Intermediate argillic
MRE01054	583180	4077721	Nontronite, Nacrite, PX-kaolinite	Halloysite, Jarosite, Nontronite	Halloysite, Nontronite, Nacrite	Intermediate argillic
MRE01055	583128	4077539	Nontronite, PX-kaolinite, Jarosite	Nontronite, Halloysite, Quartz-2	Nontronite, Halloysite, Quartz-2	Argillic
MRE01058	582183	4077342	Nontronite, PX-kaolinite, Jarosite	Kaolinite, K-feldspar, alunite	Kaolinite, Nontronite, Alunite	Intermediate argillic
MRE02020	584256	4080946	PX-kaolinite, Nontronite, Jarosite	Nontronite, Halloysite, Quartz-2	Nontronite, Halloysite, Quartz-2	Argillic
MRE02021	584127	4080828	Nontronite, Montmorillonite, PX-kaolinite	Kaolinite, Quartz-2, Nontronite	Kaolinite, Nontronite, Montmorillonite, Quartz-2	Intermediate argillic
MRE02023	583858	4080649	HX-kaolinite, Montmorillonite, Dickite	Kaolinite, Quartz-2, Nontronite	Kaolinite, HX-kaolinite, Montmorillonite, Dickite, Nontronite	Intermediate argillic
MRE02025	583670	4080354	Montmorillonite, PX-kaolinite, Pyrophyllite	Kaolinite, Quartz-2, Halloysite	Kaolinite, Montmorillonite, Quartz-2, Pyrophyllite, Halloysite	Intermediate argillic
MRE02026	583527	4080215	HX-kaolinite, Nontronite	Kaolinite, Quartz-2, Alunite	Kaolinite, HX-kaolinite, Nontronite, Quartz-2, Alunite	Intermediate argillic
MRE02030	583987	4079500	H-Halloysite, Dickite, Pyrophyllite	Quartz-2, Alunite, Kaolinite	Quartz-2, Alunite, Kaolinite	Silicic
MRE02031	583956	4079303	HX-kaolinite, H-Halloysite, Dickite, Alunite	Nontronite, Halloysite, Alunite	HX-kaolinite, Nontronite, Halloysite, Dickite, Alunite	Intermediate argillic
MRE03025	580848	4078979	Montmorillonite, Nacrite, Jarosite	K-feldspar, Alunite, Kaolinite, Quartz-2	Montmorillonite, Alunite, kaolinite, Nacrite, Quartz-2	Argillic
P.012	587024	4079067	Alunite, HX-kaolinite	Alunite, Quartz-2, Kaolinite	Alunite, Quartz-2, HX-kaolinite, Kaolinite	1st Advanced argillic

Appendix 7: Sample location in the geological map



Appendix 8: Assigned alteration zones versus existing alteration map

